
NORWEGIAN UNIVERSITY OF SCIENCE AND
TECHNOLOGY

PHYSICS, MASTER THESIS

Sensitivity to Numerical Integration Scheme in Calculation of Lagrangian Coherent Structures

Author:

Arne Magnus Tveita LØKEN

Supervisor:

Assoc. Prof. Tor NORDAM

Department of Physics
Norwegian University of Science and Technology
N-7491 Trondheim, Norway

May 23, 2018



Norwegian University of
Science and Technology

Abstract

Sammendrag

Preface

Table of Contents

List of Figures	ix
List of Tables	xi
Notation	xiii
1 Introduction	1
2 Theory	3
2.1 Solving systems of ordinary differential equations	3
2.1.1 The Runge-Kutta family of numerical ODE solvers	4
2.1.2 Spline interpolation of discrete data	9
2.2 The type of flow systems considered	11
2.3 Definition of Lagrangian coherent structures for three-dimensional flows . .	13
2.3.1 Hyperbolic LCSs in three dimensions	14
3 Method	17
3.1 Flow systems defined by analytical velocity fields	17
3.1.1 Steady Arnold-Beltrami-Childress flow	17
3.1.2 Unsteady Arnold-Beltrami-Childress flow	17
3.2 Flow systems defined by gridded velocity data	18
3.2.1 Oceanic currents in the Førde fjord	18
3.2.2 Interpolating gridded velocity data	19
3.3 Computing the flow map and its directional derivatives	20
3.3.1 Advectiong a set of tracers	20
3.3.2 The implementation of dynamic Runge-Kutta step size	21
3.4 Computing Cauchy-Green strain eigenvalues and -vectors	22
3.5 Preliminaries for computing repelling LCSs in 3D flow by means of geodesic level sets	24
3.5.1 Identifying suitable initial conditions for developing LCSs	24
3.5.2 Parametrizing the innermost level set	25
3.6 Legacy approach to computing new mesh points	27
3.6.1 Selecting initial conditions from which to compute new mesh points	28
3.6.2 Choosing new trajectory start points by an algorithm with memory .	30
3.6.3 Handling failures to compute satisfactory mesh points	31
3.7 Revised approach to computing new mesh points	33
3.7.1 Computing pseudoradial trajectories directly	33
3.7.2 Handling failures to compute satisfactory mesh points	34
3.7.3 Key improvements of the revised algorithm for computing new mesh points	35
3.8 Managing mesh accuracy	36
3.8.1 Maintaining mesh point density	36

Table of Contents

3.8.2	Limiting the accumulation of numerical noise	37
3.8.3	A curvature-based approach to determining interset separations	38
3.9	Continuously reconstructing manifold surfaces from expanding point meshes in 3D	40
3.10	Macroscale stopping criteria for the expansion of computed manifolds	41
3.10.1	Continuous self-intersection checks	42
3.11	Identifying LCSs as subsets of computed manifolds	44
3.12	Making the most of the available computational resources	46
4	Results	49
4.1	Verifying our method of generating manifolds	49
4.1.1	An analytical test case	49
4.1.2	Sample manifolds computed from the steady ABC flow	50
4.2	Verifying our method of extracting LCSs from the computed manifolds	52
4.2.1	An analytical test case	52
4.2.2	Verifying that the computed LCSs are in fact repelling	55
4.3	Computed LCSs in the ABC flow	56
4.4	Computed LCSs in the Førde fjord	58
5	Discussion	65
5.1	Regarding the variational approach to computing the Cauchy-Green strain characteristics	65
6	Conclusions	67
References		69
A	Appendix A	71

List of Figures

<p>2.1 A selection of commonly used interpolation methods applied to a discretely sampled, high order polynomial</p> <p>2.2 Geometric interpretation of the eigenvectors of the Cauchy-Green strain tensor</p> <p>3.1 Time dependence of the coefficient functions for unsteady ABC flow</p> <p>3.2 Stereographical map projection of the Førde fjord and its surroundings</p> <p>3.3 Conceptual illustration of the special-purpose cubic interpolation routine for the Cauchy-Green strain eigenvectors</p> <p>3.4 The construction of the innermost geodesic level set</p> <p>3.5 Visualization of the direction field used to compute trajectories within a manifold, using the legacy approach</p> <p>3.6 Visualization of typical trajectories used to compute a new mesh point, using the legacy approach</p> <p>3.7 Flowchart illustrating the algorithm for iteratively choosing new trajectory start points based on the termination status of the preceding trajectories, using the legacy approach.</p> <p>3.8 Visualization of a typical trajectory used to compute a new mesh point, using the revised approach</p> <p>3.9 Our approach to inserting new, or removing, mesh points to maintain mesh point density</p> <p>3.10 Our approach to limit the compound numerical error, by continuously removing unwanted loops in the computed level sets</p> <p>3.11 The principles of curvature-guided interset step length adjustment</p> <p>3.12 How our triangulation algorithm handled the special cases arising when the one-to-one correspondence between the points in subsequent level sets was broken</p> <p>3.13 Flowchart illustrating the algorithm for detecting self-intersections</p> <p>3.14 How the intersection-detection algorithm handles special cases</p> <p>3.15 An example of a repelling LCS extracted as a subset of a computed manifold</p> <p>3.16 Our way of assigning weights to mesh points in computed LCSs</p> <p>4.1 Geodesic level set approximation to analytically known three-dimensional surface</p> <p>4.2 RMS error of geodesic level set approximations to analytically known three-dimensional surface, as a function of mesh point density</p> <p>4.3 Geodesic level set approximations with varying mesh point densities, for a manifold in the steady ABC flow</p> <p>4.4 Trajectories orthogonal to the ξ_3-direction field, superimposed onto a computed manifold surface in the steady ABC flow</p> <p>4.5 Arithmetic average of λ_3 across all solid angles, for a purely radial velocity field</p> <p>4.6 The single repelling LCS present in the purely radial velocity field</p> <p>4.7 Advection of tracers in order to verify the repelling nature of the computed LCSs</p> <p>4.8 Four views of the \mathcal{U}_0 domain obtained for transport in the steady ABC flow</p> <p>4.9 Four views of the \mathcal{U}_0 domain obtained for transport in the unsteady ABC flow</p>	<p>10</p> <p>13</p> <p>18</p> <p>19</p> <p>23</p> <p>26</p> <p>28</p> <p>30</p> <p>32</p> <p>35</p> <p>37</p> <p>39</p> <p>40</p> <p>42</p> <p>43</p> <p>44</p> <p>46</p> <p>47</p> <p>51</p> <p>52</p> <p>53</p> <p>54</p> <p>54</p> <p>55</p> <p>56</p> <p>57</p> <p>58</p>
---	---

List of Figures

4.10	Four views of the repelling LCSs obtained for transport in the steady ABC flow	60
4.11	Four views of the repelling LCSs obtained for transport in the unsteady ABC flow	61
4.12	Four views of the \mathcal{U}_0 domain obtained for transport in the Førde fjord	62
4.13	Four views of the repelling LCSs obtained for transport in the Førde fjord . . .	64

List of Tables

2.1	Butcher tableau representing a generic s -stage Runge-Kutta method	6
2.2	Butcher tableau representation of a generic, embedded, explicit Runge-Kutta method	7
2.3	Butcher tableau representation of the explicit, classical, 4 th -order Runge-Kutta method	7
2.4	Butcher tableau representation of the Dormand-Prince 8(7) embedded Runge-Kutta method	8
3.1	Grid parameters for advection in the considered flow systems	20
3.2	Parameter choices for selecting LCS initial conditions	25
4.1	Parameter values used to approximate an analytically known three-dimensional surface by the method of geodesic level sets	50
4.2	Parameters used to compute manifolds, and subsequently repelling LCSs, in the ABC flow (both variants)	59
4.3	Parameters used to compute manifolds, and subsequently repelling LCSs, in the Førde fjord	63

Notation

Newton's notation is used for differentiation with respect to time, i.e.:

$$\dot{f}(t) \equiv \frac{df(t)}{dt}.$$

Vectors are denoted by lowercase, upright, bold letters, like this:

$$\xi = (\xi_1, \xi_2, \dots, \xi_n).$$

The Euclidean inner product for two vectors $(\xi, \psi) \in \mathbb{R}^n$ is denoted by:

$$\langle \xi, \psi \rangle = \sum_{i=1}^n \xi_i \psi_i.$$

The Euclidean norm of a vector $\xi \in \mathbb{R}^n$ is designated as:

$$\|\xi\| = \sqrt{\langle \xi, \xi \rangle}.$$

Matrices and matrix representations of rank-2 tensors are denoted by uppercase, upright, bold letters, as follows:

$$\mathbf{A} = (a_{i,j}) = \begin{pmatrix} a_{1,1} & a_{1,2} & \dots & a_{1,n} \\ a_{2,1} & a_{2,2} & \dots & a_{2,n} \\ \vdots & \vdots & \ddots & \vdots \\ a_{m,1} & a_{m,2} & \dots & a_{m,n} \end{pmatrix}.$$

1 Introduction

2 Theory

2.1 SOLVING SYSTEMS OF ORDINARY DIFFERENTIAL EQUATIONS

In physics, like other sciences, modeling a system often equates to solving an initial value problem. An initial value problem can be described in terms of an ordinary differential equation (hereafter abbreviated to ODE) of the form

$$\dot{x}(t) = f(t, x(t)), \quad x(t_0) = x_0, \quad (2.1)$$

where x is an unknown function (scalar or vector) of time t . The function f is defined on an open subset Ω of $\mathbb{R} \times \mathbb{R}^n$, where n is the number of spatial dimensions; that is, the number of components of x . The initial condition (t_0, x_0) is a point in the domain of f , i.e., $(t_0, x_0) \in \Omega$. In higher dimensions (namely, $n > 1$), the differential equation (2.1) generally extends to a coupled family of ODEs

$$\dot{x}_i(t) = f_i(t, x_1(t), x_2(t), \dots, x_n(t)), \quad x_i(t_0) = x_{i,0}, \quad i = 1, \dots, n. \quad (2.2)$$

The system is nonlinear if the function f in equation (2.1), or, if at least one of the functions $\{f_i\}$ in equation (2.2), is nonlinear in one or more of its arguments. For the sake of notational simplicity, the discussion to follow in the rest of this section is based on the one-dimensional case, that is, system (2.1), for $n = 1$. However, all of the considerations also hold for $n > 1$.

Say that the solution of system (2.1) is sought at some time t_f . In order to approximate said solution numerically, the time variable must be discretized first. This is frequently done by defining

$$t_j = t_0 + j \cdot h, \quad (2.3)$$

where t_j is the time level j for integer j , and h is some increment which is smaller than $t_f - t_0$. Typically, the time increment is chosen such that an integer number of step lengths h equals the difference $t_f - t_0$. With the discretized time, the numerical solution of system (2.1) is found by successive applications of some numerical integration method. The Runge-Kutta family of numerical methods for ODE systems is a common choice, and will be elaborated upon in greater detail in section 2.1.1.

All numerical integration schemes fall into one of two categories; explicit and implicit methods. Explicit methods are characterized by computing the state of the system at a later time, based on the state of the system at the current time (in some cases, the state at earlier times are also considered). Implicit methods, however, involve the solution of an equation in which both the current and the later state of the system are involved. Thus, a generic, explicit method for computing the state of the system at time $t + h$, given its state at t , can be expressed as

$$x(t + h) = F(x(t)), \quad (2.4a)$$

while, for implicit methods, an equation of the sort

$$G(x(t), x(t + h)) = 0, \quad (2.4b)$$

is solved to find $x(t + h)$.

In general, implicit methods require the solution of a linear system at every time step. Clearly, implicit methods are more computationally demanding than explicit methods. The main selling point of implicit methods is that they are more numerically stable than explicit methods. This property means that implicit methods are particularly well-suited for *stiff* systems, i.e., physical systems with highly disparate time scales (Hairer and Wanner 1996, p.2). For such systems, most explicit methods are unstable, unless the time step h is made exceptionally small, rendering these methods practically useless. For *nonstiff* systems, however, implicit methods behave similarly to their explicit analogues in terms of numerical accuracy and convergence properties.

Irrespective of which numerical integration method is employed, one obtains an approximation of the true solution of the system (2.1) *at* the discrete time levels, that is,

$$x_j \approx x(t_j), \quad (2.5)$$

where $x(t)$ is the exact solution at time t . The accuracy of the approximation, however, depends on both the numerical integration method and the time step length h used for the temporal discretization. One way of obtaining approximations of the true solution *inbetween* the discrete time levels is by means of interpolation — a numerical technique which will be elaborated upon in section 2.1.2. For nonlinear systems, analytical solutions usually do not exist. Thus, such systems are often analyzed by means of numerical methods.

2.1.1 The Runge-Kutta family of numerical ODE solvers

In numerical analysis, the Runge-Kutta family of methods is a popular collection of implicit and explicit iterative methods, used in temporal discretization in order to obtain numerical approximations of the *true* solutions of systems like (2.1). The German mathematicians C. Runge and M.W. Kutta developed the first of the family's methods at the turn of the twentieth century (Hairer, Nørsett, and Wanner 1993, p.134). The general outline of what is now known as a Runge-Kutta method is as follows:

Definition 1 (Runge-Kutta methods).

Let s be an integer and $\{a_{i,j}\}_{i,j=1}^s$, $\{b_i\}_{i=1}^s$ and $\{c_i\}_{i=1}^s$ be real coefficients.

Let h be the numerical step length used in the temporal discretization.

Then, the method

$$\begin{aligned} k_i &= f\left(t_n + c_i h, x_n + h \sum_{j=1}^s a_{i,j} k_j\right), \quad i = 1, \dots, s, \\ x_{n+1} &= x_n + h \sum_{i=1}^s b_i k_i, \end{aligned} \quad (2.6)$$

is called an *s-stage Runge-Kutta method* for the system (2.1).

The main reason to include multiple stages in a Runge-Kutta method is to improve the numerical accuracy of the computed solutions. The *order* of a Runge-Kutta method can be defined as follows:

Definition 2 (*Order of Runge-Kutta methods*).

A Runge-Kutta method, given by equation (2.6), is of *order p* if, for sufficiently smooth systems (2.1), the local error e_n scales as h^{p+1} . That is:

$$e_n = \|x_n - u_{n-1}(t_n)\| \leq K h^{p+1} \quad (2.7)$$

where $u_{n-1}(t)$ is the exact solution of the ODE in system (2.1) at time t , subject to the initial condition $u_{n-1}(t_{n-1}) = x_{n-1}$, and K is a numerical constant. This is true, if the Taylor series for the exact solution $u_{n-1}(t_n)$ and the numerical solution x_n coincide up to (and including) the term h^p .

The *global* error

$$E_n = x_n - x(t_n), \quad (2.8)$$

where $x(t)$ is the exact solution of system (2.1) at time t , accumulated by n repeated applications of the numerical method, can be estimated by

$$|E_n| \leq C \sum_{l=1}^n |e_l|, \quad (2.9)$$

where C is a numerical constant, depending on both the right hand side of the ODE in system (2.1) and the difference $t_n - t_0$. Making use of definition 2, the global error is limited from above by

$$\begin{aligned} |E_n| &\leq C \sum_{l=1}^n |e_l| \leq C \sum_{l=1}^n |K_l| h^{p+1} \leq C \max_l \{|K_l|\} n h^{p+1} \\ &\leq C \max_l \{|K_l|\} \frac{t_n - t_0}{h} h^{p+1} \leq \tilde{K} h^p, \end{aligned} \quad (2.10)$$

where \tilde{K} is a numerical constant. Equation (2.10) demonstrates that, for a p -th order Runge-Kutta method, the global error can be expected to scale as h^p .

In definition 1, the matrix $(a_{i,j})$ is commonly called the *Runge-Kutta matrix*, while the coefficients $\{b_i\}$ and $\{c_i\}$ are known as the *weights* and *nodes*, respectively. Since the 1960s, it has been customary to represent Runge-Kutta methods, given by equation (2.6), symbolically, by means of mnemonic devices known as Butcher tableaus (Hairer, Nørsett, and Wanner 1993, p.134). The Butcher tableau for a general s -stage Runge-Kutta method, as introduced in definition 1, is presented in table 2.1. For explicit Runge-Kutta methods, the Runge-Kutta matrix $(a_{i,j})$ is lower triangular. Similarly, for fully implicit Runge-Kutta methods, the Runge-Kutta matrix is upper triangular. The difference between explicit and implicit methods is outlined in equation (2.4).

During the first half of the twentieth century, a substantial amount of research was conducted in order to develop numerically robust, high-order, explicit Runge-Kutta methods. The idea

Table 2.1: Butcher tableau representing a generic s -stage Runge-Kutta method.

c_1	$a_{1,1}$	$a_{1,2}$	\dots	$a_{1,s}$
c_2	$a_{2,1}$	$a_{2,2}$	\dots	$a_{2,s}$
\vdots	\vdots	\vdots	\ddots	\vdots
c_s	$a_{s,1}$	$a_{s,2}$	\dots	$a_{s,s}$
	b_1	b_2	\dots	b_s

was that using such methods would mean one could resort to larger time increments h without sacrificing precision in the computed solution. However, the required number of stages s grows quicker than linearly as a function of the required order p . It has been proven that, for $p \geq 5$, no explicit Runge-Kutta method of order p with $s = p$ stages exists ([Hairer, Nørsett, and Wanner 1993](#), p.173). This is one of the reasons for the attention shift from the latter half of the 1950s and onwards, towards so-called *embedded* Runge-Kutta methods.

The basic idea of embedded Runge-Kutta methods is that they, aside from the numerical approximation x_{n+1} , yield a second approximation \widehat{x}_{n+1} . The difference between the two approximations then provides an estimate of the local error of the less precise result, which can be used for automatic step size control ([Hairer, Nørsett, and Wanner 1993](#), pp.167–168). The trick is to construct two independent, explicit Runge-Kutta methods which both use the *same* function evaluations. This results in practically obtaining the two solutions for the price of one, in terms of computational complexity. The Butcher tableau of a generic, embedded, explicit Runge-Kutta method is illustrated in table 2.2.

For embedded methods, the coefficients are tuned such that

$$x_{n+1} = x_n + h \sum_{i=1}^s b_i k_i \quad (2.11a)$$

is of order p , and

$$\widehat{x}_{n+1} = x_n + h \sum_{i=1}^s \widehat{b}_i k_i \quad (2.11b)$$

is of order \widehat{p} , typically with $\widehat{p} = p+1$. Which of the solutions is used to continue the numerical integration, depends on the integration method in question. In the following, the solution which is *not* used to continue the integration, will be referred to as the *interpolant* solution.

There exists an abundance of Runge-Kutta methods; many of which are fine-tuned for specific constraints, such as problems of varying degrees of stiffness. Based on prior investigations — such as the work done by [Løken \(2017\)](#) — using explicit, high order, embedded Runge-Kutta methods to compute Lagrangian coherent structures (which will be elaborated upon in section 2.3) consistently yields accurate solutions at lower computational cost than the most common fixed stepsize methods. Accordingly, the Dormand-Prince 8(7) method — consisting

Table 2.2: Butcher tableau representation a generic, embedded, explicit Runge-Kutta method.

0				
c_2	$a_{2,1}$			
c_3	$a_{3,1}$	$a_{3,2}$		
\vdots	\vdots	\vdots	\ddots	
c_s	$a_{s,1}$	$a_{s,2}$	\dots	$a_{s,s-1}$
	b_1	b_2	\dots	b_{s-1}
	\widehat{b}_1	\widehat{b}_2	\dots	\widehat{b}_{s-1}
				\widehat{b}_s

of an eighth order solution with a seventh order interpolant — was chosen as the single, multipurpose, numerical ODE solver for this project.

Note that the concept of *order* is less well-defined for embedded methods than for fixed stepsize methods, as a direct consequence of the adaptive time step. Although the *local* errors of each integration step scale as per equation (2.7), the bound on the *global* (i.e., observable) error suggested in equation (2.10) is invalid, as the time step is, in principle, different for each integration step. Butcher tableau representations of the classical 4th-order Runge-Kutta method and the embedded Dormand-Prince 8(7) method are available in tables 2.3 and 2.4; where the latter of which has been typeset in landscape mode for the reader’s convenience. Details on how the dynamic time step of the Dormand-Prince 8(7) method was implemented will be presented in section 3.3.2.

Table 2.3: Butcher tableau representation of the explicit, classical, 4th-order Runge-Kutta method.

0				
$\frac{1}{2}$	$\frac{1}{2}$			
$\frac{1}{2}$	0	$\frac{1}{2}$		
1	0	0	1	
	$\frac{1}{6}$	$\frac{1}{3}$	$\frac{1}{3}$	$\frac{1}{6}$

Table 2.4: Butcher tableau for the Dormand-Prince 8(7) embedded Runge-Kutta method. The b coefficients give an 8th-order accurate solution used to continue the integration. The \hat{b} coefficients yield a 7th-order interpolant, which can be used to estimate the error of the numerical approximation, and to dynamically adjust the time step. The provided coefficients are rational approximations, accurate to about 24 significant decimal digits. For reference, see Prince and Dormand (1981).

0	1	$\frac{1}{18}$	$\frac{1}{16}$	$\frac{1}{48}$	$\frac{1}{32}$	$\frac{5}{32}$	$\frac{75}{64}$	$\frac{3}{64}$	$\frac{3}{20}$	$\frac{-28693883}{1125000000}$	$\frac{23124283}{1800000000}$
$\frac{93}{400}$	$\frac{29443841}{614563906}$	0	0	$\frac{77736358}{692538347}$	$\frac{77736358}{692538347}$	$\frac{1125000000}{1125000000}$	$\frac{-28693883}{1125000000}$	$\frac{23124283}{1800000000}$	$\frac{-180193667}{-180193667}$	$\frac{545815736}{545815736}$	$\frac{1043307555}{1043307555}$
$\frac{93}{200}$	$\frac{16016141}{946692911}$	0	0	$\frac{61564180}{158732637}$	$\frac{61564180}{158732637}$	$\frac{633445777}{2771057229}$	$\frac{633445777}{2771057229}$	$\frac{100302831}{100302831}$	$\frac{790204164}{790204164}$	$\frac{800635310}{800635310}$	$\frac{3783071287}{3783071287}$
$\frac{5490023248}{9719169821}$	$\frac{39632708}{573591083}$	0	0	$\frac{-433636366}{683701615}$	$\frac{-433636366}{683701615}$	$\frac{-421739975}{2616292301}$	$\frac{-421739975}{2616292301}$	$\frac{723423059}{723423059}$	$\frac{839813087}{839813087}$	$\frac{393006217}{393006217}$	$\frac{123872331}{123872331}$
$\frac{13}{20}$	$\frac{246121993}{1340847787}$	0	0	$\frac{-37695042795}{15268766246}$	$\frac{-37695042795}{15268766246}$	$\frac{-309121744}{1061227803}$	$\frac{-309121744}{1061227803}$	$\frac{6005943493}{490766935}$	$\frac{6005943493}{490766935}$	$\frac{1396673457}{2108947689}$	$\frac{1396673457}{2108947689}$
$\frac{1201146811}{1299019798}$	$\frac{-1028468189}{84618014}$	0	0	$\frac{8478235783}{508512851}$	$\frac{8478235783}{508512851}$	$\frac{1311729495}{1432422823}$	$\frac{1311729495}{1432422823}$	$\frac{-10304129995}{1701304382}$	$\frac{-10304129995}{1701304382}$	$\frac{-48777925059}{3047939560}$	$\frac{-48777925059}{3047939560}$
1	$\frac{185892177}{718116043}$	0	0	$\frac{-3185094517}{667107341}$	$\frac{-3185094517}{667107341}$	$\frac{-477755414}{1098033517}$	$\frac{-477755414}{1098033517}$	$\frac{-703635378}{230739211}$	$\frac{-703635378}{230739211}$	$\frac{5731566787}{1027345527}$	$\frac{5731566787}{1027345527}$
1	$\frac{403863854}{491063109}$	0	0	$\frac{-5068492393}{454740067}$	$\frac{-5068492393}{454740067}$	$\frac{-411421997}{543043805}$	$\frac{-411421997}{543043805}$	$\frac{652783627}{92320556}$	$\frac{652783627}{92320556}$	$\frac{1173962825}{6184727034}$	$\frac{1173962825}{6184727034}$
	$\frac{1400451}{335480064}$	0	0	0	0	$\frac{-59238493}{106827825}$	$\frac{-59238493}{106827825}$	$\frac{1811606767}{758867731}$	$\frac{1811606767}{758867731}$	$\frac{56129285}{797845732}$	$\frac{56129285}{797845732}$
	$\frac{13451932}{455176623}$	0	0	0	0	$\frac{-808719486}{976000145}$	$\frac{-808719486}{976000145}$	$\frac{1757004468}{5045159321}$	$\frac{1757004468}{5045159321}$	$\frac{65604539}{265891186}$	$\frac{65604539}{265891186}$
								$\frac{-386757421}{1518517206}$	$\frac{-386757421}{1518517206}$	$\frac{465885868}{32273535}$	$\frac{465885868}{32273535}$
								$\frac{53011238}{667516719}$	$\frac{53011238}{667516719}$	$\frac{2}{45}$	$\frac{0}{45}$

2.1.2 Spline interpolation of discrete data

As all naturally occurring physical systems can only be known partially, either by means of partial measurements or grid based model output, interpolating (i.e., estimating) the measurement data becomes a requirement when describing the dynamics of systems which depend on measurement data from inbetween the sampling or grid points. Spline interpolation involves approximating a discretely sampled function by a series of piecewise defined polynomials. According to Stoer and Bulirsch (2002, p.93), spline interpolation is a popular tool within the field of numerical analysis, due to yielding smooth interpolation curves with limited interpolation error when using low degree polynomial pieces. Furthermore, the local nature of spline interpolated functions means that such functions are less prone to oscillatory behaviour when using high order polynomials. This is in stark contrast to regular, global polynomial interpolation, which exhibits strong global dependence on local properties. In particular, if the function to be approximated is badly behaved anywhere within the interval of approximation, then the approximation by polynomial interpolation is poor everywhere (de Boor 1978, p.17).

A generic interpolation problem can be described in terms of a family of functions

$$\Theta(\mathbf{x}; \beta_0, \dots, \beta_n), \quad (2.12)$$

each of which characterized by the $n + 1$ parameters $\{\beta_i\}$, with \mathbf{x} containing the independent variables of the problem. Given a set of $n + 1$ discrete measurements — each defined by a set of coordinates and function values (\mathbf{x}_i, f_i) where $\mathbf{x}_i \neq \mathbf{x}_j$ for $i \neq j$ and $f_i = f(\mathbf{x}_i)$ — the interpolation problem reduces to finding parameters $\{\beta_i\}$ such that

$$\Theta(\mathbf{x}; \beta_0, \dots, \beta_n) = f_i, \quad i = 0, \dots, n \quad (2.13)$$

is satisfied. According to Stoer and Bulirsch (2002, pp.38–39), spline interpolation problems (amongst others) can be classified as linear interpolation problems, meaning that the family of interpolation functions (cf. equation (2.12)) can be expressed as

$$\Theta(\mathbf{x}; \beta_0, \dots, \beta_n) = \sum_{i=0}^n \beta_i \Theta_i(\mathbf{x}). \quad (2.14)$$

In the following, let the coordinates $\{\mathbf{x}_i\}$, function values $\{f_i\}$ and sampling points $\{(\mathbf{x}_i, f_i)\}$ be denoted by *support abscissas*, *support ordinates* and *support points*, respectively.

Solving an interpolation problem by means of spline interpolation is done by determining the set of parameters $\{\beta_i\}$ of equations (2.13) and (2.14), with the family of functions $\{\Theta_i\}$ limited to spline functions. These functions, often denoted as *splines*, are connected through the use of a partition. Consider the one-dimensional case for the sake of notational simplicity — the considerations to follow also hold for higher dimensions, but invariably introduces notational clutter. The partition

$$\Delta : \quad \{a = x_0 < x_1 < \dots < x_n = b\} \quad (2.15)$$

of the closed interval $[a, b]$ determines the domains of the piecewise polynomial spline functions \mathcal{S} in the set \mathcal{S}_Δ . These spline functions are joined at support abscissas, which, in the context of splines, are called *knots*.

Stoer and Bulirsch (2002, p.107) define a *piecewise polynomial function* as follows:

Definition 3 (Piecewise polynomial functions).

Let f be a real-valued function which, for each $i = 0, \dots, n - 1$, when restricted to the subinterval (x_i, x_{i+1}) of the partition given in equation (2.15) corresponds to a polynomial $p_i(x)$ of degree less than or equal to $r - 1$.

In order to obtain a one-to-one correspondence between the function f and the polynomial sequence $(p_0(x), p_1(x), \dots, p_{n-1}(x))$, define f at the knots $\{x_i\}_{i=0}^{n-1}$, so that the function becomes continuous from the right.

Accordingly, spline functions \mathcal{S}_Δ of degree k are polynomial functions of degree k which are $(k - 1)$ times continuously differentiable at the interior knots, that is, $\{x_i\}_{i=1}^{n-1}$, of the partition Δ . These k^{th} -order polynomials are uniquely determined by $k + 1$ coefficients, of which k are given by the $(k - 1)$ derivatives and function values at their left bordering knot.

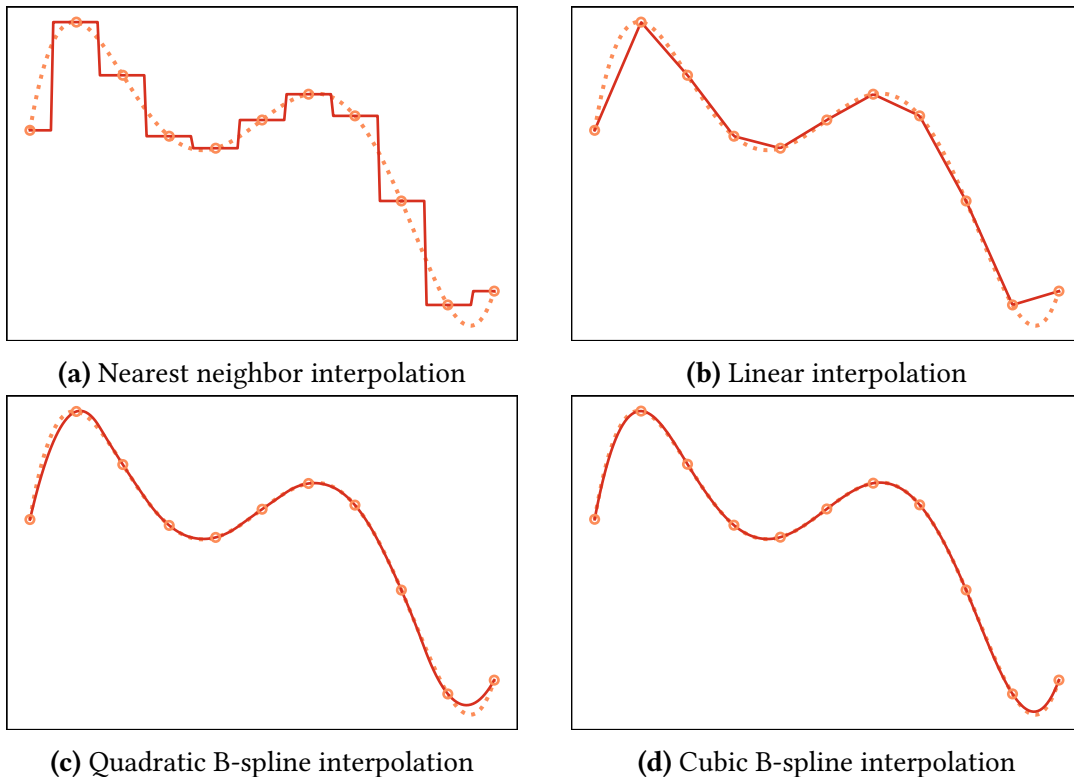


Figure 2.1: A selection of commonly used interpolation methods applied to a discretely sampled, high order polynomial (dashed). The sampling points (knots) are shown as hollow circles. Observe how higher order splines yield increasingly accurate and smooth interpolations.

B-splines are a family of nonnegative spline functions which have minimal support for any given degree, smoothness and domain partition. Furthermore, any spline function of a given degree can be expressed as a linear combination of B-splines of the same degree

(Stoer and Bulirsch 2002, pp.107–110). Accordingly, B-splines provide the foundation of efficient and numerically stable computations of splines. A selection of commonly used interpolation methods applied to a discretely sampled, high order polynomial is shown in figure 2.1. From the figure, the increased precision of higher order splines when applied to continuous functions is readily apparent. Note, however, that higher order interpolation methods require more sampling points than lower order methods. In particular, at least $k + 1$ samples are required in order to construct a k^{th} order spline. In higher dimensions, that is, with data which depends on several other (independent) variables, the required amount of samples increases rapidly with the interpolation order. Subsequently, the use of cubic B-splines constitutes a popular method for general-purpose interpolation, providing a good balance between numerical accuracy and computational complexity.

2.2 THE TYPE OF FLOW SYSTEMS CONSIDERED

We consider flow in three-dimensional dynamical systems of the form

$$\dot{\mathbf{x}} = \mathbf{v}(t, \mathbf{x}), \quad \mathbf{x} \in \mathcal{U}, \quad t \in \mathcal{I}, \quad (2.16)$$

i.e., systems defined for the finite time interval \mathcal{I} on an open, bounded subset \mathcal{U} of \mathbb{R}^3 . In addition, the velocity field \mathbf{v} is assumed to be smooth in its arguments. Depending on the exact nature of the velocity field \mathbf{v} , analytical particle trajectories, that is, analytical solutions of system (2.16), may or may not exist. The flow particles are assumed to be infinitesimal and massless, i.e., non-interacting *tracers* of the overall circulation.

Consider a finite time interval $[t_0, t_1] \subset \mathcal{I}$ such that all tracer trajectories $\mathbf{x}(t; t_0, \mathbf{x}_0)$ in the system given by equation (2.16) are defined for all times $t \in [t_0, t_1]$. Then, the flow map is defined as

$$\Phi_{t_0}^t(\mathbf{x}_0) = \mathbf{x}(t; t_0, \mathbf{x}_0), \quad (2.17)$$

that is, the flow map describes the movement of tracers from one point in time to another mathematically. In general, the flow map is as smooth as the underlying velocity field (cf. system (2.16)) (Farazmand and Haller 2012a). In Lagrangian flow analysis, the *Jacobian matrix* of the flow map $\Phi_{t_0}^t$ plays a significant role. Component-wise, the Jacobian matrix of a general vector-valued function \mathbf{f} is defined as

$$(\nabla \mathbf{f})_{i,j} = \frac{\partial f_i}{\partial x_j}, \quad \mathbf{f} = \mathbf{f}(\mathbf{x}) = (f_1(\mathbf{x}), f_2(\mathbf{x}), \dots), \quad (2.18)$$

which, for our three-dimensional flow, reduces to

$$\nabla \mathbf{f} = \begin{pmatrix} \frac{\partial f_1}{\partial x} & \frac{\partial f_1}{\partial y} & \frac{\partial f_1}{\partial z} \\ \frac{\partial f_2}{\partial x} & \frac{\partial f_2}{\partial y} & \frac{\partial f_2}{\partial z} \\ \frac{\partial f_3}{\partial x} & \frac{\partial f_3}{\partial y} & \frac{\partial f_3}{\partial z} \end{pmatrix}. \quad (2.19)$$

Making use of the definition of the flow map (cf. equation (2.17)) in conjunction with equation (2.16), one finds the following ordinary differential equation which describes the time evolution of the flow map:

$$\dot{\phi} = v(t, \phi), \quad (2.20)$$

where t_0 , t and \mathbf{x}_0 have been omitted in order to avoid notational clutter. These are, however, implicit by context. As the nabla operator is time-independent, equation (2.20) immediately yields an ordinary differential equation for the time development of the directional derivative of the flow map, namely

$$\frac{d}{dt}(\hat{\mathbf{u}} \cdot \nabla)\phi = (\mathbf{u} \cdot \nabla)v(t, \phi), \quad (2.21)$$

which holds along any constant (unit) vector \mathbf{u} . On a regular Cartesian grid, equation (2.21) provides a coupled set of ordinary differential equations describing the time evolution of each component of the Jacobian of the flow map:

$$\begin{aligned} \frac{d}{dt}\left(\frac{\partial\phi_i}{\partial x_j}\right) &= \sum_k \frac{\partial v_i}{\partial x_k}\Big|_{(t,\phi)} \frac{\partial\phi_k}{\partial x_j}\Big|_t, \\ \frac{\partial\phi_i}{\partial x_j}\Big|_{t_0} &= \delta_{ij}, \quad \mathbf{x}_0 \in \mathcal{U}, \quad t \in [t_0, t_1], \end{aligned} \quad (2.22)$$

where the Kronecker delta is defined as

$$\delta_{ij} = \begin{cases} 1, & \text{if } i = j, \\ 0, & \text{if } i \neq j. \end{cases} \quad (2.23)$$

The initial conditions for the Jacobi components reflect the fact that, for a regular Cartesian grid, the directional derivative of the x coordinate in the x direction is 1, but zero in the y and z directions.

For sufficiently smooth velocity fields, the flow map Jacobian $\nabla\phi_{t_0}^t$ can be computed, which allows for the right Cauchy-Green strain tensor field to be defined as

$$\mathbf{C}_{t_0}^t(\mathbf{x}_0) = \left(\nabla\phi_{t_0}^t(\mathbf{x}_0)\right)^* \left(\nabla\phi_{t_0}^t(\mathbf{x}_0)\right), \quad (2.24)$$

where the asterisk refers to the adjoint operation, which, because the Jacobian $\nabla\phi_{t_0}^t$ is real-valued, equates to matrix transposition. Moreover, as the Jacobian of the flow map is invertible, the Cauchy-Green strain tensor $\mathbf{C}_{t_0}^t(\mathbf{x}_0)$ is symmetric and positive definite ([Farazmand and Haller 2012a](#)). Thus, it has three real, positive eigenvalues and orthogonal, real eigenvectors. Its eigenvalues λ_i and corresponding unit eigenvectors ξ_i are defined by

$$\begin{aligned} \mathbf{C}_{t_0}^t(\mathbf{x}_0)\xi_i(\mathbf{x}_0) &= \lambda_i\xi_i(\mathbf{x}_0), \quad i = 1, 2, 3, \\ \langle \xi_i(\mathbf{x}_0), \xi_j(\mathbf{x}_0) \rangle &= \delta_{ij}, \quad 0 < \lambda_1(\mathbf{x}_0) \leq \lambda_2(\mathbf{x}_0) \leq \lambda_3(\mathbf{x}_0), \end{aligned} \quad (2.25)$$

where the Kronecker delta is defined in equation (2.23), and the dependence of λ_i and ξ_i on t_0 and t has been suppressed, for the sake of notational transparency. The geometric interpretation of equation (2.25) is that a fluid element undergoes the most stretching along the ξ_3 axis, less stretching along the ξ_2 axis, and the least stretching along the ξ_1 axis. This concept is shown in figure 2.2.

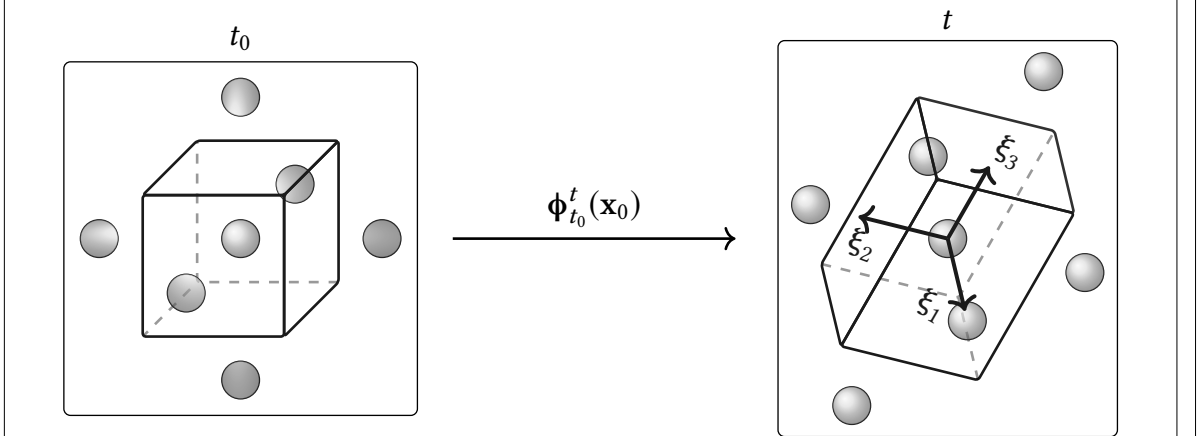


Figure 2.2: Geometric interpretation of the eigenvectors of the Cauchy-Green strain tensor. The central unit cell is stretched and deformed under the flow map $\phi_{t_0}^t(x_0)$. The local stretching is the largest in the direction of ξ_3 , the eigenvector which corresponds to the largest eigenvalue, λ_3 , of the Cauchy-Green strain tensor, defined in equation (2.25). Along the ξ_i axes, the stretch factors are given by $\sqrt{\lambda_i}$, respectively.

As the stretch factors along the ξ_i axes are given by the square roots of the corresponding eigenvalues, for incompressible flow, the eigenvalues satisfy

$$\lambda_1(x_0)\lambda_2(x_0)\lambda_3(x_0) = 1 \quad \forall x_0 \in \mathcal{U}, \quad (2.26)$$

where, in the context of tracer advection, incompressibility is equivalent to the velocity field v being divergence-free (i.e., $\nabla \cdot v \equiv 0$ in system (2.16)).

2.3 DEFINITION OF LAGRANGIAN COHERENT STRUCTURES FOR THREE-DIMENSIONAL FLOWS

A necessary prerequisite for three-dimensional Lagrangian flow analysis is the concept of *material surfaces*, which Oettinger and Haller (2016) define as

Definition 4 (*Material surfaces*).

Consider a set of initial positions forming a two-dimensional surface $\mathcal{M}(t_0)$ at time t_0 in \mathcal{U} . Its time- t image, $\mathcal{M}(t)$, is obtained under the flow map as

$$\mathcal{M}(t) = \phi_{t_0}^t(\mathcal{M}(t_0)). \quad (2.27)$$

The union of *all* time- t images, $\cup_{t \in [t_0, t_1]} \mathcal{M}(t)$, is a hypersurface in the extended phase space $\mathcal{U} \times \mathcal{I}$, called a *material surface*.

In the following, the entire material surface will be referred to by the notation $\mathcal{M}(t)$. Although no material surfaces can be crossed by tracers, only special material surfaces create coherence in the phase space \mathcal{U} and thus act as observable transport barriers. Such material surfaces are generally referred to as *Lagrangian coherent structures* (henceforth abbreviated to LCSs).

Subsequently, LCSs can be described as time-evolving surfaces which shape coherent trajectory patterns in dynamical systems, defined over a finite time interval (Haller 2011).

There are three main types of LCSs, namely *elliptic*, *hyperbolic* and *parabolic*. Roughly speaking, parabolic LCSs outline cores of jet-like trajectories, elliptic LCSs describe vortex boundaries, whereas hyperbolic LCSs are comprised of overall attractive or repelling manifolds. As such, hyperbolic LCSs practically act as organizing centers of observable tracer patterns ([Onu, Huhn, and Haller 2015](#)). Because hyperbolic LCSs provide the most readily applicable insight in terms of forecasting flow in e.g. oceanic currents, such structures have been the focus of this project.

2.3.1 Hyperbolic LCSs in three dimensions

The identification of LCSs for reliable forecasting requires sufficiency and necessity conditions, supported by mathematical theorems. [Haller \(2011\)](#) derived a variational LCS theory based on the Cauchy-Green strain tensor, defined by equation (2.24), from which the aforementioned conditions follow. The immediately relevant parts of Haller's theory are given in definitions 5–8 ([Haller 2011](#)).

Definition 5 (*Normally repellent material surfaces*).

A *normally repellent material surface* over the time interval $[t_0, t_1]$ is a compact material surface segment $\mathcal{M}(t)$ which is overall repelling, and on which the normal repulsion rate is greater than the tangential repulsion rate.

The required *compactness* of the material surface segment signifies that, in some sense, it must be topologically well-behaved. That the material surface is *overall repelling* means that nearby trajectories are repelled from, rather than attracted towards, the material surface. Lastly, requiring that the *normal* repulsion rate is greater than the *tangential* repulsion rate means that nearby trajectories are in fact driven away from the material surface, rather than being stretched along with it due to shear stress.

Definition 6 (*Repelling LCS*).

A *repelling LCS* over the time interval $[t_0, t_1]$ is a normally repelling material surface $\mathcal{M}(t_0)$ whose normal repulsion admits a pointwise non-degenerate maximum relative to any nearby material surface $\widehat{\mathcal{M}}(t_0)$.

Definition 7 (*Attracting LCS*).

An *attracting LCS* over the time interval $[t_0, t_1]$ is defined as a repelling LCS over the *backward* time interval $[t_1, t_0]$.

Definition 8 (*Hyperbolic LCS*).

A *hyperbolic LCS* over the time interval $[t_0, t_1]$ is a *repelling* or *attracting* LCS over the same time interval.

Note that the above definitions associate LCSs with the time interval \mathcal{I} over which the dynamical system under consideration is known, or, at the very least, where information regarding the behaviour of tracers, is sought. Generally, LCSs obtained over a time interval \mathcal{I} do not necessarily exist over different time intervals ([Farazmand and Haller 2012a](#)).

For sufficiently smooth three-dimensional flow, the above definitions can be summarized as a set of mathematical existence criteria, based on the Cauchy-Green strain tensor (cf. equation (2.24)) (Haller 2011; Farazmand and Haller 2012a; Karrasch 2012; Farazmand and Haller 2012b). These are given in theorem 1.

Theorem 1 (*Sufficient and necessary conditions for LCSs in three-dimensional flows*). Consider a compact material surface $\mathcal{M}(t) \subset \mathcal{U}$ evolving over the time interval $[t_0, t_1]$. Then $\mathcal{M}(t)$ is a repelling LCS over $[t_0, t_1]$ if and only if all of the following holds for all initial conditions $\mathbf{x}_0 \in \mathcal{M}(t_0)$:

$$\lambda_2(\mathbf{x}_0) \neq \lambda_3(\mathbf{x}_0) > 1, \quad (2.28a)$$

$$\langle \xi_3(\mathbf{x}_0), \mathbf{H}_{\lambda_3}(\mathbf{x}_0) \xi_3(\mathbf{x}_0) \rangle < 0 \quad (2.28b)$$

$$\xi_3(\mathbf{x}_0) \perp \mathcal{M}(t_0), \quad (2.28c)$$

$$\langle \nabla \lambda_3(\mathbf{x}_0), \xi_3(\mathbf{x}_0) \rangle = 0. \quad (2.28d)$$

In theorem 1, $\langle \cdot, \cdot \rangle$ signifies the Euclidean inner product, and \mathbf{H}_{λ_3} denotes the Hessian matrix of the largest eigenvalues of the Cauchy-Green strain tensor field. Component-wise, the Hessian matrix of a general, smooth, scalar-valued function f is defined as

$$(\mathbf{H}_f)_{i,j} = \frac{\partial^2 f}{\partial x_i \partial x_j}, \quad (2.29)$$

which, for our three-dimensional flow, reduces to

$$\mathbf{H}_f = \begin{pmatrix} \frac{\partial^2 f}{\partial x^2} & \frac{\partial^2 f}{\partial x \partial y} & \frac{\partial^2 f}{\partial x \partial z} \\ \frac{\partial^2 f}{\partial y \partial x} & \frac{\partial^2 f}{\partial y^2} & \frac{\partial^2 f}{\partial y \partial z} \\ \frac{\partial^2 f}{\partial z \partial x} & \frac{\partial^2 f}{\partial z \partial y} & \frac{\partial^2 f}{\partial z^2} \end{pmatrix}. \quad (2.30)$$

Condition (2.28a) ensures that the normal repulsion rate is larger than the tangential stretch due to shear strain along the LCS, in accordance with definition 5. Conditions (2.28c) and (2.28d) suffice to enforce that the normal repulsion rate attains a local extremum along the LCS, relative to all nearby material surfaces. Lastly, condition (2.28b) ensures that this is a strict local maximum.

From condition (2.28c) and the orthormality of the Cauchy-Green strain eigenvectors (cf. equation (2.25)), it follows that any initial LCS surface is tangent to the planes locally spanned by $\xi_1(\mathbf{x}_0)$ and $\xi_2(\mathbf{x}_0)$. Thus, an integral curve of any (normalized) linear combination of the ξ_1 - and ξ_2 -direction fields, launched from an arbitrary point of the surface $\mathcal{M}(t_0)$, will never leave $\mathcal{M}(t_0)$. Hence:

Remark 1 (*Invariance of initial positions of repelling LCSs*).

The initial position $\mathcal{M}(t_0)$ of any repelling LCS (definition 6) is an invariant manifold of the autonomous dynamical system

$$\mathbf{r}' = a\xi_1(\mathbf{r}) + b\xi_2(\mathbf{r}), \quad a^2 + b^2 = 1. \quad (2.31)$$

Note that the converse of remark 1 does not hold. That is, a material surface $\Xi(t_0)$ which is an invariant manifold of all (normalized) linear combinations of ξ_1 and ξ_2 does not necessarily correspond to a repelling LCS $\mathcal{M}(t_0)$ – that is, unless $\Xi(t_0)$ also satisfies conditions (2.28a), (2.28b) and (2.28d).

3 Method

3.1 FLOW SYSTEMS DEFINED BY ANALYTICAL VELOCITY FIELDS

3.1.1 Steady Arnold-Beltrami-Childress flow

The Arnold-Beltrami-Childress (henceforth abbreviated to ABC) flow is a three-dimensional, incompressible velocity field which solves the Euler equations exactly. It is a simple example of a fluid flow which can exhibit chaotic behaviour ([Frisch 1995](#), p.204). In terms of the Cartesian coordinate vector $\mathbf{x} = (x, y, z)$, the system can be expressed mathematically as

$$\dot{\mathbf{x}} = \mathbf{v}(t, \mathbf{x}) = \begin{pmatrix} A \sin(z) + C \cos(y) \\ B \sin(x) + A \cos(z) \\ C \sin(y) + B \cos(x) \end{pmatrix}, \quad (3.1)$$

where A , B and C are parameters which dictate the nature of the flow pattern. The inherent periodicity with regards to the Cartesian axes naturally leads to a domain of interest $\mathcal{U} = [0, 2\pi]^3$, with periodic boundary conditions imposed in x , y and z .

Here, the parameter values

$$A = \sqrt{3}, \quad B = \sqrt{2}, \quad C = 1 \quad (3.2)$$

were used, as has been common in litterature (e.g. by [Oettinger and Haller \(2016\)](#)), as these values are known to result in chaotic tracer trajectories ([Zhao et al. 1993](#)). The time interval of interest for this system was $\mathcal{I} = [0, 5]$.

3.1.2 Unsteady Arnold-Beltrami-Childress flow

Inspired by [Oettinger and Haller \(2016\)](#), a temporally aperiodic modification of the ABC flow (equation (3.1)) was made by the replacements

$$\begin{aligned} B &\rightarrow \tilde{B}(t) = B + B \cdot k_0 \tanh(k_1 t) \cos((k_2 t)^2), \\ C &\rightarrow \tilde{C}(t) = C + C \cdot k_0 \tanh(k_1 t) \sin((k_3 t)^2), \end{aligned} \quad (3.3)$$

with A , B and C given by equation (3.2), where the parameters values

$$k_0 = 0.3, \quad k_1 = 0.5, \quad k_2 = 1.5, \quad k_3 = 1.8, \quad (3.4)$$

were used. The fundamental idea of this modification is to further enhance the chaotic nature of the resulting flow patterns. Similarly modified ABC flow has previously been at the centre of other three-dimensional transport barrier investigations – including hyperbolic LCSs – such as the work of [Blazevski and Haller \(2014\)](#); albeit with quite different methods of computing said LCSs than the one considered here. Like for its stationary sibling, the time interval of interest for this system was $\mathcal{I} = [0, 5]$. The time dependence of the \tilde{B} and \tilde{C} coefficients is illustrated in figure 3.1.

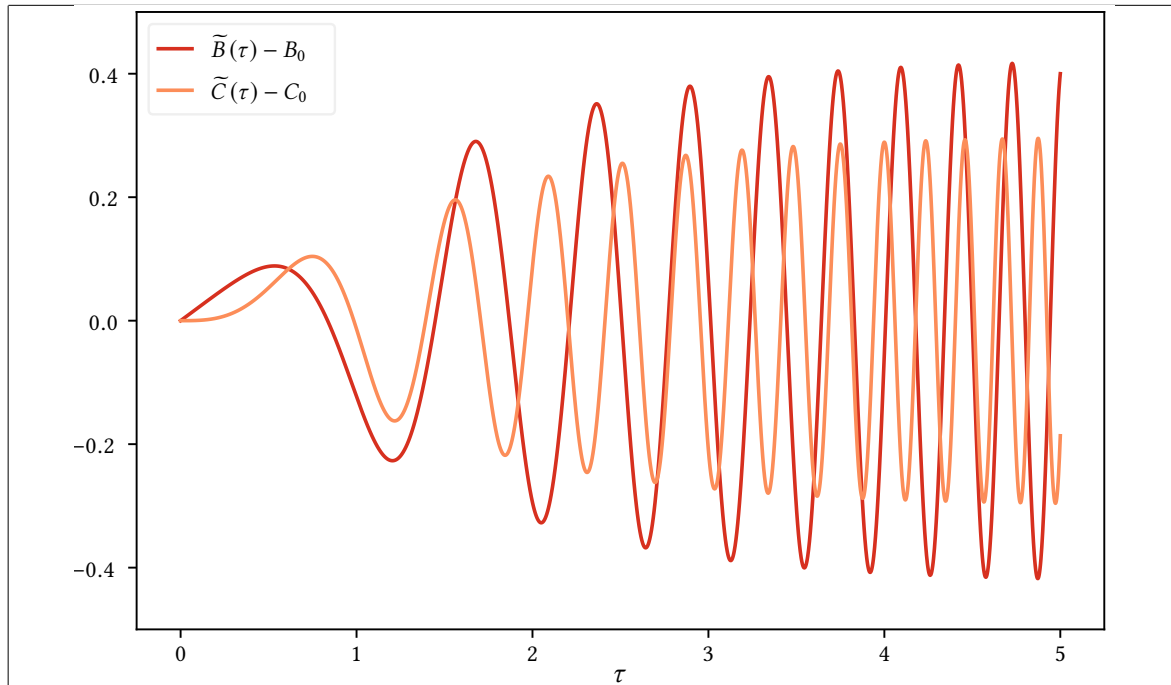


Figure 3.1: Time dependence of the coefficient functions for unsteady ABC flow, defined in equations (3.2)–(3.4).

3.2 FLOW SYSTEMS DEFINED BY GRIDDED VELOCITY DATA

3.2.1 *Oceanic currents in the Førde fjord*

In 2016, the mining company Nordic Mining ASA received permission from the Norwegian Ministry of Climate and Environment to extract rutile from the Engebø mountain in Naustdal, Norway (Garvik 2017; Haugan 2015). Furthermore, the company were authorized to dump the mining waste into the nearby Førde fjord; a legislation which has been debated fiercely, and heavily protested against, ever since the original application was submitted in 2008. Early estimates suggest that, when operating at full scale, the mining operation will result in yearly oceanic mine tailings deposits in excess of five million tonnes (Garvik 2017).

Several centres of technical expertise – such as the Norwegian Institute of Marine Research – have publically advised against depositing mine tailings into the fjord, emphasizing the potentially severe negative consequences for the aquaculture (Haugan 2015). Not only is the surrounding area a significant spawning ground for cod, there is always a possibility of particles being transported by the water currents such that they contaminate the outer edges of the fjord, or even into the ocean. Accordingly, the use of LCSs in order to predict possible flow patterns for contaminants resulting from the deposit of mine tailings would be of great environmental interest.

To this end, gridded three-dimensional velocity data, modelling oceanic currents in the (depths of the) Førde Fjord, was made available by SINTEF Fisheries and Aquaculture, based on the SINMOD oceanic model (Slagstad and McClimans 2005). The data set considered here contains velocity data for the time period between June 1 2013, 00:00 and June 2 2013, 23:40,

sampled in intervals of 20 minutes, with a horizontal resolution of approximately 50m and vertical resolution varying from 25m in the fjord depths, to 1m near the surface. For our simulations, the time interval of interest was the 12 hour time window between 00:00 and 12:00 on June 1 2013 – practically ensuring the encapsulation of a tidal cycle.

Seeing as some of the most harmful contaminants found within the mine tailings are heavy metals, we concentrated our analysis on the depths of the fjord. Accordingly, we looked for LCSs in a region of water which was neither particularly close to the oceanic surface, nor hit the coastline when advected for the 12 hour duration of the time interval of interest. This limited our research to a $500\text{ m} \times 500\text{ m} \times 250\text{ m}$ region, with depths ranging from 50 m to 300 m below the surface. A bird's-eye view of the region is shown in white in figure 3.2, which also contains a map view of the geographical region.

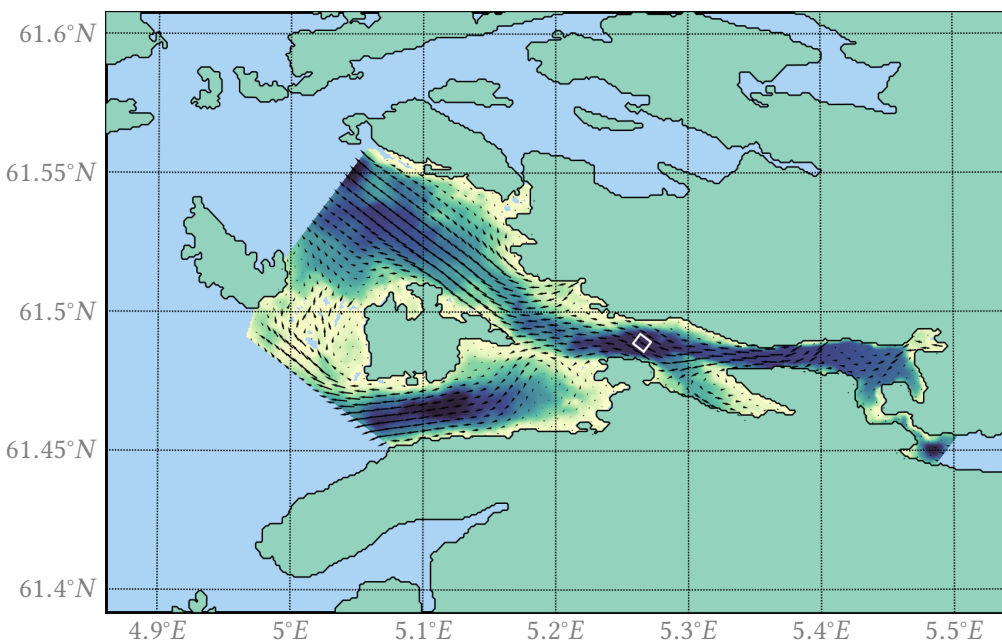


Figure 3.2: Stereographical map projection of the Førde fjord and its surroundings. The local fjord depths are indicated by a varying background color. A subset of the gridded velocity vectors indicates the macroscopic trends of the oceanic currents at a depth of 50 m below the surface. Outlined in white is a bird's-eye view of the main region of interest; namely, a region of water which was neither particularly close to the oceanic surface, nor struck the coastline when transported by the currents for the duration of the 12 hour time interval of interest.

3.2.2 Interpolating gridded velocity data

In order to describe transport phenomena in the Førde fjord, interpolating the discretely sampled velocity field becomes necessary. Based upon the considerations presented in section 2.1.2, we elected to do so by means of cubic B-splines in time and space. Thus, each of the velocity field's three components was considered to be a quadrivariate function of time and the three spatial coordinates.

Several multidimensional B-spline interpolation libraries are publically available under open access licensing. For this project, we elected to use the Bspline-Fortran library, partly motivated by its extensive documentation (Williams 2018). In particular, we made use of the `bspline_4d` derived type, which we, along with a subset of its type-bound procedures, made available in C making use of the Fortran standard interoperability with C-languages, that is, the `iso_c_binding` module – which is shipped with most modern Fortran compilers. From there, we wrote a thin wrapper class in C++, which was exposed to Python via Cython.

The choice of Python as our main programming language was made partly due to its relatively low development costs, in addition to its beneficial properties as a ‘glue language’ – as exemplified by the above, and the ease of parallelization by means of e.g. MPI (the use of which will be outlined in greater detail in section 3.12). Moreover, by utilizing Fortran’s reference-based subroutine call structure, in addition to pointers at C-level (typed memoryviews in Cython), we were able to minimize memory duplication. This could otherwise have been a significant bottleneck.

3.3 COMPUTING THE FLOW MAP AND ITS DIRECTIONAL DERIVATIVES

3.3.1 *Advection of a set of tracers*

The variational framework for computing LCSs is based upon the advection of non-interacting tracers, as described in section 2.2, by the systems mentioned in sections 3.1 and 3.2. The computational domains \mathcal{U} were discretized by a set equidistant tracers, effectively creating a uniform grid with tracers placed on and within the domain boundaries of \mathcal{U} . The grid parameters are summarized in table 3.1.

Table 3.1: Grid parameters for advection in the considered flow systems. For the fjord system, the domain extents and grid spacings are given in units of metre. Also note that the grid spacings have been truncated to two significant decimal digits.

	Analytical ABC flow	Fjord model data
Computational domain	$[0, 2\pi]^3$	$[0, 500] \times [0, 500] \times [50, 300]$
N_x, N_y, N_z	256, 256, 256	200, 200, 100
$\Delta x = \Delta y = \Delta z$	$2.5 \cdot 10^{-2}$	2.5

In order to increase the precision of the computed Cauchy-Green strain tensor field, it is necessary to increase the accuracy with which one computes the Jacobian of the flow map, as their accuracies are intrinsically linked; which follows from equation (2.24). Accordingly, the flow map Jacobian was computed directly, by means of simultaneously solving the twelve coupled ODEs given by equations (2.16) and (2.22) while letting the underlying velocity field transport the tracers. All twelve ODEs were solved simultaneously, via the Dormand-Prince 8(7) method (see section 2.1.1 and, in particular, table 2.4). The dynamic step length adjustment procedure will be outlined in detail in section 3.3.2.

In this framework, the tracer advection takes second stage to the ‘advection’ of the components of the flow map Jacobian. As it turns out, the increase in mathematical complexity which the coupling terms introduces is a small price to pay for the increased precision compared to the straightforward approach of applying a finite difference scheme to the advected flow map (Oettinger and Haller 2016). This is also evident from previous ‘finite difference-based’ LCS computing endeavors, in which the use of several grids of tracers was necessitated in order to accurately compute the flow map Jacobian (Løken 2017; Farazmand and Haller 2012a).

3.3.2 The implementation of dynamic Runge-Kutta step size

In order to implement automatic step size control, the procedure suggested by Hairer, Nørsett, and Wanner (1993, pp.167–168) was followed closely. A starting step size h needs to be prescribed; this generally differs based upon the (pseudo-)time scale of the underlying system. For the first solution step, the embedded Dormand-Prince 8(7) method, as described in section 2.1.1 and table 2.4, yields the two approximations x_1 and \hat{x}_1 , from which the difference $x_1 - \hat{x}_1$ can be used as an estimate of the error of the less precise result. The idea is to enforce the error of the numerical solution to satisfy, componentwise:

$$|x_{1,i} - \hat{x}_{1,i}| \leq sc_i, \quad sc_i = Atol_i + \max(|x_{1,i}|, |\hat{x}_{1,i}|) \cdot Rtol_i, \quad (3.5)$$

where $Atol_i$ and $Rtol_i$ are the desired absolute and relative tolerances. For this project, the tolerance values

$$Atol_i = 10^{-7}, \quad Rtol_i = 10^{-7} \quad (3.6)$$

were used throughout.

As a measure of the numerical error,

$$\text{err} = \sqrt{\frac{1}{n} \sum_{i=1}^n \left(\frac{x_{1,i} - \hat{x}_{1,i}}{sc_i} \right)^2} \quad (3.7)$$

is used. Then, err is compared to unity in order to find an optimal step size. From definition 2, it follows that err scales like h^{q+1} , where $q = \min(p, \hat{p})$. Under the assumption $1 \approx Kh_{\text{opt}}^{q+1}$, one finds the optimal step size from

$$h_{\text{opt}} = h \cdot \left(\frac{1}{\text{err}} \right)^{\frac{1}{q+1}}. \quad (3.8)$$

If $\text{err} \leq 1$, the suggested solution step is accepted, the (pseudo-)time variable t is increased by h , and the step length is modified according to equations (3.8) and (3.9). Which of the two approximations x_{n+1} or \hat{x}_{n+1} is used to continue the integration generally depends on the embedded Runge-Kutta method in question. Continuing the integration with the higher order result is commonly referred to as *local extrapolation*. The Dormand-Prince 8(7) method is tuned in order to minimize the order of the higher order result; accordingly, local extrapolation was used throughout. If $\text{err} > 1$, the solution step is rejected, and the step length decreased before attempting another step. The procedure for updating the time step

can be summarized as follows:

$$h_{\text{new}} = \begin{cases} \min(\text{fac}_{\max} \cdot h, \text{fac} \cdot h_{\text{opt}}) & \text{if the solution step is accepted,} \\ \text{fac} \cdot h_{\text{opt}}, & \text{if the solution step is rejected,} \end{cases} \quad (3.9)$$

where fac and fac_{\max} are numerical safety factors, intended to prevent increasing the step size *too much*. Here, the parameter values

$$\text{fac} = 0.8, \quad \text{fac}_{\max} = 2.0, \quad (3.10)$$

were used throughout.

3.4 COMPUTING CAUCHY-GREEN STRAIN EIGENVALUES AND -VECTORS

Computing the Cauchy-Green strain tensor field directly, by performing a series of matrix products per its definition in equation (2.24), and then solving for its eigenvalues and -vectors turns out to be numerically disadvantageous (Oettinger and Haller 2016). In particular, this method leaves the smallest eigenvalues quite susceptible to numerical round-off error. A fully equivalent, more numerically sound way of identifying the Cauchy-Green strain eigenvalues and -vectors is based on performing an SVD decomposition of the Jacobian field of the flow map, i.e.,

$$\nabla \phi_{t_0}^t(\mathbf{x}_0) = \mathbf{U} \Sigma \mathbf{V}^*, \quad (3.11)$$

where the asterisk refers to the adjoint operation, \mathbf{U} and \mathbf{V} are unitary matrices and Σ is a diagonal matrix with nonnegative real numbers — the *singular values* of $\nabla \phi$ — on the diagonal. Because the flow map Jacobian is square, so too are the matrices \mathbf{U} , Σ and \mathbf{V} . Moreover, as the flow map Jacobian is real-valued, so too are the matrices \mathbf{U} and \mathbf{V} . The eigenvalues of the right Cauchy-Green strain tensor (cf. equations (2.24) and (2.25)) are given by the squares of the singular values, that is, $\lambda_i(\mathbf{x}_0) = (\sigma_i(\mathbf{x}_0))^2$, and the corresponding orthonormal eigenvectors are found in the columns of \mathbf{V} .

Interpolating the Cauchy-Green strain eigenvalues

For computing LCSs, the Cauchy-Green strain eigenvalues frequently need to be evaluated inbetween the grid points. Moreover, as suggested by the existence criterion given in equation (2.28b), all of the second derivatives of $\lambda_3(\mathbf{x}_0)$ are also needed. Accordingly, the eigenvalues were interpolated by means of cubic trivariate B-splines, in order to ensure continuous second derivatives. For this purpose, the `bspline_3d` derived type from the Bspline-Fortran library (Williams 2018) was ported to Python using the techniques described in section 3.2.2.

Interpolating the Cauchy-Green strain eigenvectors

Just like the eigenvalues of the Cauchy-Green strain tensor field, its eigenvectors frequently need to be evaluated inbetween the grid points in order to compute LCSs. Like the strain

eigenvalues, the strain eigenvectors were interpolated by means of cubic trivariate B-splines, through the `bspline_3d` derived type from the Bspline-Fortran library ([Williams 2018](#)) — albeit with a twist, in order to remove local orientational discontinuities. In particular, the local stretch is equal in magnitude along any given negative ξ_i axis as that of its positive counterpart, and there is no a priori reason to expect the SVD decomposition (cf. equation (3.11)) to follow any particular convention regarding the ‘sign’ of the computed eigenvectors.

The interpolation routine outlined here is a generalization of a similar special-purpose linear interpolation routine which has previously been utilized to compute LCSs in two spatial dimensions ([Onu, Huhn, and Haller 2015](#); [Løken 2017](#)). The routine is based upon careful monitoring and local reorientation prior to cubic interpolation, and its two-dimensional equivalent is illustrated in figure 3.3 — the principles are similar in three dimensions, but illustrating a two-dimensional projection of the three-dimensional case simply became cluttered beyond comprehension.

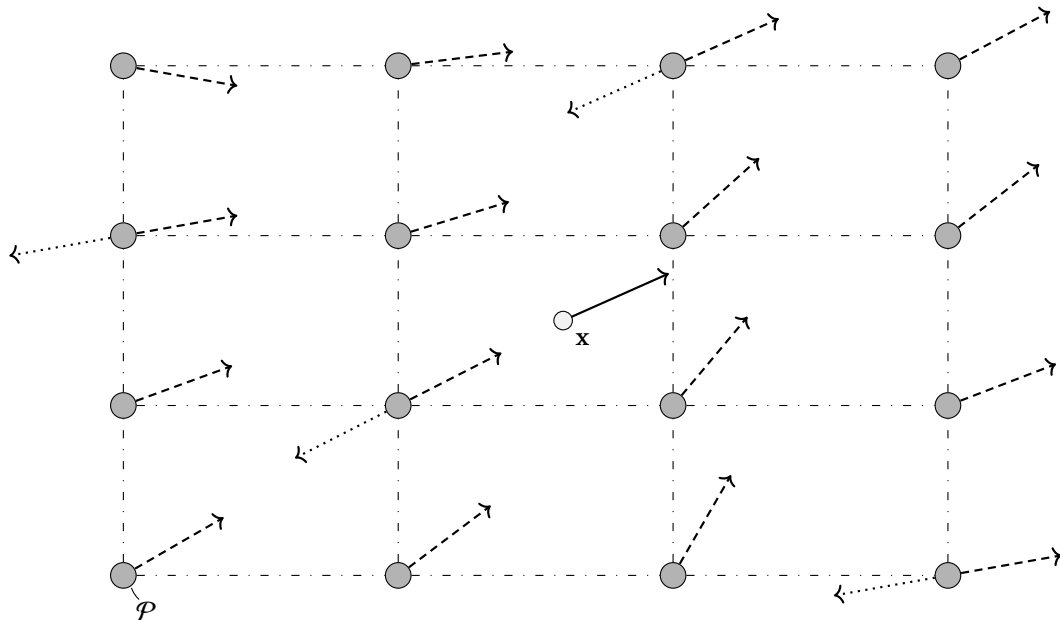


Figure 3.3: Conceptual illustration of the special-purpose cubic interpolation routine for the Cauchy-Green strain eigenvectors. The 64 nearest grid points (16 in two dimensions; here shown in gray) to any given coordinate x are identified. As the local stretch is equal in magnitude along the negative ξ_i axis as that of its positive counterpart, we are free to reverse any ξ_i vector which is rotated more than 90° with regards to the selected pivot vector (at the grid point denoted by P) prior to interpolating the components of ξ_i , making use of cubic B-splines. The vectors used in the local cubic interpolation are dashed, whereas the vectors which had to be reversed are dotted.

First, the 64 (in two dimensions: 16) nearest neighboring grid points to any given coordinate x are identified. Choosing a vector at a corner of this local interpolation voxel, orientational discontinuities inbetween the grid elements are found by inspecting the inner products of the ξ_i vectors of the remaining grid points with the pivot. Rotations exceeding 90° are identified by inner products with the pivot vector being negative, labelled as orientational

discontinuities, and then corrected by reversing the sign of the corresponding vectors. For each of ξ_i 's three components, cubic B-spline interpolation is used within the interpolation voxel in order to find $\xi_i(\mathbf{x})$, which is then normalized, like the ξ_i vectors defined at the grid points are a priori.

3.5 PRELIMINARIES FOR COMPUTING REPELLING LCSs IN 3D FLOW BY MEANS OF GEODESIC LEVEL SETS

Repelling LCSs in three spatial dimensions are quite challenging to compute. Straightforward numerical integration of the flow is insufficient — in three dimensions, the existence criterion (2.28c) provides another degree of freedom, as, everywhere within such an LCS, one is allowed to move ‘freely’ within a plane which is orthogonal to $\xi_3(\mathbf{x})$. Dedicated algorithms are needed. Here, we consider a (variation of) the method of geodesic level sets for computing repelling LCSs as invariant manifolds of the ξ_1 and ξ_2 direction fields (cf. remark 1), as presented by [Krauskopf et al. \(2005\)](#). The short presentation to follow in the next paragraph will be explained further in depth in the subsequent subsections.

The method is based on the concept of developing an unstable manifold from a local neighborhood of an initial condition \mathbf{x}_0 (how these initial conditions were chosen will be described in section 3.5.1). In particular, a small, closed curve C_1 consisting of points which all lie within the tangent plane defined by the coordinate \mathbf{x}_0 and the unit normal $\xi_3(\mathbf{x}_0)$, separated from \mathbf{x}_0 by a distance δ_{init} , is assumed to consist of points which all lie within the same manifold as \mathbf{x}_0 . The idea is then to compute the next geodesic circle in a local, dynamic coordinate system, defined by hyperplanes which are orthogonal to the most recently computed geodesic circle. A set of accuracy parameters governs the number of next points by which the next geodesic circle is approximated, in solving a set of boundary value problems. During the computation, the interpolation error stays bounded by the density of mesh points, so that the overall quality of the mesh is preserved.

3.5.1 Identifying suitable initial conditions for developing LCSs

Inspired by the two-dimensional approach of [Farazmand and Haller \(2012a\)](#), in order to identify repelling LCSs, the first step was to identify the subdomain $\mathcal{U}_0 \subset \mathcal{U}$ in which the existence conditions (2.28a), (2.28b) and (2.28d) are satisfied — as these conditions can be verified for individual points, unlike criterion (2.28c). All grid points which lie within \mathcal{U}_0 would then be valid initial conditions for repelling LCSs. Of the aforementioned criteria, condition (2.28d) is the least straightforward to implement numerically, as identifying the zeros of inner products is prone to numerical round-off error. Our approach is based on comparing the value of λ_3 at a given grid point \mathbf{x}_0 to the values of λ_3 at the two points $\mathbf{x}_0 \pm \varepsilon \xi_3(\mathbf{x}_0)$, where ε is a number one order of magnitude smaller than the grid spacing. Should $\lambda_3(\mathbf{x}_0)$ be the largest of the three, the point \mathbf{x}_0 would be flagged as satisfying criterion (2.28d).

Using all of the points in \mathcal{U}_0 domain would invariably involve computing a lot of LCSs

several times over — in particular, if two neighboring grid points are both located in the \mathcal{U}_0 domain, then they likely belong to the same manifold. In order to reduce the number of redundant calculations, the set of considered initial conditions was further reduced, by only checking whether every v^{th} grid point along each axis belonged to \mathcal{U}_0 , that is, only considering one in every v^3 grid points in the entire domain as possible initial conditions. Because the number of grid points was different for the different types of flow (cf. table 3.1), so too was the pseudo-sampling frequency v . The values for ε , v and the resulting number of initial conditions are given in table 3.2. Note that, using the given filtering parameters, the initial conditions reduced to a far more manageable number of grid points, than all of the grid points which satisfy the LCS conditions (2.28a), (2.28b) and (2.28d).

Table 3.2: Parameter choices for selecting LCS initial conditions. ε was made to be one order of magnitude smaller than the grid spacing, and v was selected to be a common divisor of the number of grid points along each Cartesian abscissa, cf. table 3.1. Note that ε for the fjord model data is given in units of metre. Observe how the reduced set of initial conditions contains orders of magnitude fewer points than the total number of grid points which satisfy the LCS existence criteria (2.28a), (2.28b) and (2.28d).

	Analytical ABC flow	Fjord model data
ε	$5 \cdot 10^{-3}$	10^{-1}
v	8	5
# initial conditions without v -filtering	340 951 (steady) 361 461 (unsteady)	209 945
# initial conditions with v -filtering	618 (steady) 676 (unsteady)	1 631

3.5.2 Parametrizing the innermost level set

For an initial condition \mathbf{x}_0 identified by means of the method outlined in section 3.5.1, the corresponding LCS must locally be tangent to the plane with unit normal given by $\xi_3(\mathbf{x}_0)$, as a consequence of LCS existence criterion (2.28c). Accordingly, the first geodesic level set is approximated by a set of n points $\{\mathcal{M}_{1,j}\}_{j=1}^n$, which all lie within the aforementioned tangent plane, separated from \mathbf{x}_0 by a distance δ_{init} ; all of which assumed to lie within the same manifold. The parameter δ_{init} was chosen small compared to the grid spacing, in order to limit the inherent errors of this linearization.

An interpolation curve C_1 was then made, with a view to representing the innermost level set in a smoother fashion. In particular, this interpolation curve was designed as a parametric spline. To this end, the points $\{\mathcal{M}_{1,j}\}_{j=1}^n$ were first ordered in clockwise or counterclockwise — merely a matter of perspective — fashion. Then, each mesh point was assigned an independent variable s based upon the cumulative interpoint distance along the ordered list of points, starting at $j = 1$; estimated by means of the Euclidean norm, then normalized by dividing s through by the total interpoint distance around the entire initial level set.

In an intermediary step, the coordinates of the mesh point $\mathcal{M}_{1,1}$ was appended to a list containing the ordered coordinates of the mesh points $\{\mathcal{M}_{1,j}\}_{j=1}^n$, such that, aside from $\mathcal{M}_{1,1}$, which corresponded to both $s = 0$ and $s = 1$, there was a one-to-one correspondence between the s -values and the coordinates of the mesh points. Then, considering each of the lists containing the Cartesian coordinates of the mesh points as univariate functions of the pseudo-arclength parameter s , separate cubic B-splines were made for each set of coordinates, making use of the `bspline_1d` extension type from the Bspline-Fortran library ([Williams 2018](#)), which was ported to Python as outlined in section 3.2.2. The constructed innermost level set and its associated interpolation curve is illustrated in figure 3.4. Interpolation curves for all subsequent level sets (the computation of which will be described in detail shortly) were made completely analogously to C_1 .

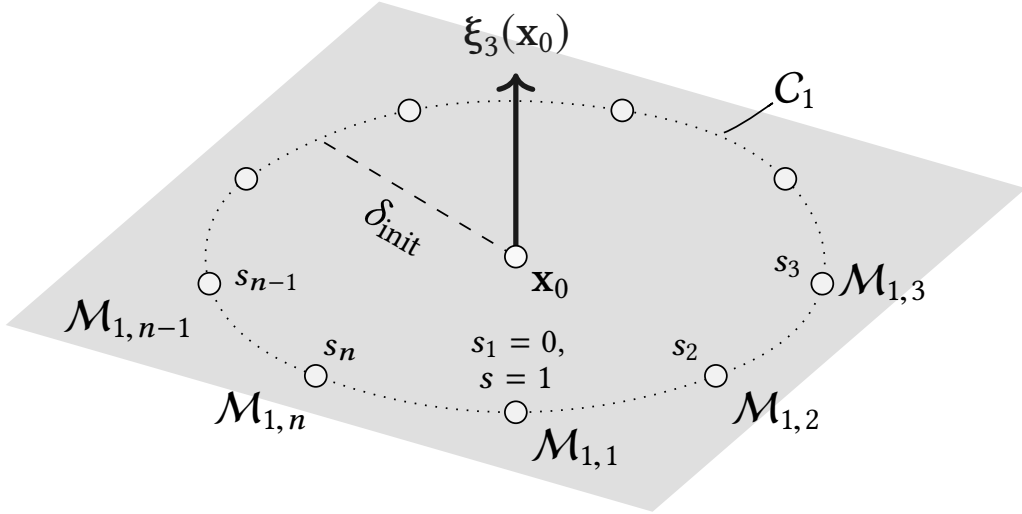


Figure 3.4: The construction of the innermost geodesic level set. An initial condition \mathbf{x}_0 is found by means of the method outlined in section 3.5.1. A set of n meshpoints $\{\mathcal{M}_{1,j}\}_{j=1}^n$ is then evenly distributed within the plane defined by the point \mathbf{x}_0 and the unit normal $\xi_3(\mathbf{x}_0)$, which is shaded. Each mesh point is separated from \mathbf{x}_0 by a small distance δ_{init} (dashed). Using a normalized pseudo-arclength parameter s , the mesh point coordinates are interpolated using cubic B-splines, forming the smooth curve C_1 (dotted).

In the following, let $\mathbf{x}_{i,j}$ denote the location of mesh point $\mathcal{M}_{i,j}$. As suggested by [Krauskopf et al. \(2005\)](#), we then sought to develop a new level set, parametrized by a new set of points $\{\mathcal{M}_{2,j}\}$ located in the family of half-planes $\{\mathcal{H}_{1,j}\}_{j=1}^n$, extending radially outwards from the corresponding points $\{\mathcal{M}_{1,j}\}_{j=1}^n$ in the initial level set while being orthogonal to C_1 . These half-planes are generally defined by the points $\mathbf{x}_{i,j}$ and the (unit) tangent vectors $\mathbf{t}_{i,j}$. For the innermost level set, these tangent vectors were computed as

$$\mathbf{t}_{1,j} = \frac{\xi_3(\mathbf{x}_0) \times (\mathbf{x}_{1,j} - \mathbf{x}_0)}{\|\xi_3(\mathbf{x}_0) \times (\mathbf{x}_{1,j} - \mathbf{x}_0)\|}. \quad (3.12)$$

For the subsequent level sets, [Krauskopf et al. \(2005\)](#) suggest determining the tangents $\mathbf{t}_{i,j}$ using the interpolation curve C_i , by drawing a vector between two points equidistant to $\mathcal{M}_{i,j}$ in either direction along C_i . However, an inheritance-based approach was found to yield more smoothly parametrized manifolds, which were less sensitive to numerical noise. This

approach, along with the treatment of special cases, will be explained in greater detail in the sections to follow (in particular, section 3.8.1).

A *guidance* vector $\rho_{i,j}$ was computed for each of the mesh points $\{\mathcal{M}_{i,j}\}$, in order to keep track of the local (quasi-)radial direction. The guidance vectors for the innermost level set were computed as

$$\rho_{1,j} = \frac{\mathbf{x}_{1,j} - \mathbf{x}_0}{\|\mathbf{x}_{1,j} - \mathbf{x}_0\|}. \quad (3.13)$$

For each mesh point in all ensuing level sets, the guidance vectors were computed relative to the coordinates of the point in the immediately preceding level set, from which the new point was computed. That is,

$$\rho_{i,j} = \frac{\mathbf{x}_{i,j} - \mathbf{x}_{i-1,j}}{\|\mathbf{x}_{i,j} - \mathbf{x}_{i-1,j}\|}, \quad (3.14)$$

where the indices j and \hat{j} generally need not be the same, as there is generally not a one-to-one correspondence between points in subsequent level sets; see section 3.8.1 for details.

Note that, in computing new mesh points, organized in level sets, a descendant point $\mathcal{M}_{i+1,j}$ has to be computed for each ancestor point $\mathcal{M}_{i,j}$. This is due to the method being based on parametrizing manifolds as a series of smooth topological circles. Should this prove not to be possible, given a set of tolerance parameters which will be described in greater detail in the sections to come, the computation would stop abruptly, leaving the manifold parametrized by however many of its geodesic level sets were successfully completed. Further details on the stopping criteria for the generation of new geodesic level sets will be presented in section 3.10.

3.6 LEGACY APPROACH TO COMPUTING NEW MESH POINTS

As tentatively suggested in section 3.5.2, each of the points in the first level set $\mathcal{M}_1 = \{\mathcal{M}_{1,j}\}_{j=1}^n$ is used to compute a point in the ensuing level set \mathcal{M}_2 . This notion extends to all of the subsequent level sets; namely, the points in level set \mathcal{M}_{i+1} are computed from the points in the prior level set \mathcal{M}_i . For reasons of brevity in the discussion to follow, denote the points $\{\mathcal{M}_{i,j}\}$ and $\{\mathcal{M}_{i+1,j}\}$ as *ancestor* and *descendant points*, respectively. Furthermore, the set of mesh points which can be traced backwards to a single, common ancestor, is referred to as a *point strain*. The considerations to follow rely on each mesh point $\mathcal{M}_{i,j}$ inheriting its tangential vector from its direct ancestor; that is, $\mathbf{t}_{i,j} := \mathbf{t}_{i-1,j}$. The treatment of the special cases of this inheritance-based approach will be described in greater detail in section 3.8.1.

From the mesh point $\mathcal{M}_{i,j}$, we wish to place a new mesh point $\mathcal{M}_{i+1,j}$ at an intersection of the manifold \mathcal{M} and the half-plane $\mathcal{H}_{i,j}$ located a distance Δ_i from $\mathcal{M}_{i,j}$. The aforementioned half-plane is defined by the coordinate $\mathbf{x}_{i,j}$, the unit normal $\mathbf{t}_{i,j}$ and the guidance vector $\rho_{i,j}$ (cf. equations (3.13) and (3.14)). Note that this intersection may occur anywhere on the half-circle within $\mathcal{H}_{i,j}$ of radius Δ_i , centered at $\mathbf{x}_{i,j}$. The search for a new mesh point is conducted by defining an aim point \mathbf{x}_{aim} within $\mathcal{H}_{i,j}$, computed by performing a single, classical, 4th-order Runge-Kutta step (cf. table 2.3) of length Δ_i in the vector field locally

defined as

$$\psi(\mathbf{x}) = \frac{\xi_3(\mathbf{x}) \times \mathbf{t}_{i,j}}{\|\xi_3(\mathbf{x}) \times \mathbf{t}_{i,j}\|}, \quad (3.15)$$

starting at $\mathbf{x}_{i,j}$. Moreover, all of the vectors of the intermediary Runge-Kutta steps were corrected, if necessary, by continuous comparison with $\rho_{i,j}$ and sign-reversion if an intermediary vector was directed radially inwards. Finally, the computed aim point was projected into the half-plane $\mathcal{H}_{i,j}$ as follows:

$$\mathbf{x}_{\text{aim}} := \mathbf{x}_{\text{aim}} - \langle \mathbf{t}_{i,j}, \mathbf{x}_{\text{aim}} \rangle \mathbf{t}_{i,j}. \quad (3.16)$$

The idea is then to look for a new position within $\mathcal{H}_{i,j}$, in the vicinity of \mathbf{x}_{aim} , which lies a distance Δ_i from $\mathbf{x}_{i,j}$, by moving within the constraints of the manifold. Motivated by remark 1, this involves computing trajectories which everywhere lie within the plane spanned by the local ξ_1 - and ξ_2 -vectors. This was done by defining a local, normalized direction field as

$$\mu(\mathbf{x}, \mathbf{x}_{\text{aim}}) = \frac{\mathbf{x}_{\text{aim}} - \mathbf{x} - \langle \xi_3(\mathbf{x}), \mathbf{x}_{\text{aim}} - \mathbf{x} \rangle \xi_3(\mathbf{x})}{\|\mathbf{x}_{\text{aim}} - \mathbf{x} - \langle \xi_3(\mathbf{x}), \mathbf{x}_{\text{aim}} - \mathbf{x} \rangle \xi_3(\mathbf{x})\|}, \quad (3.17)$$

that is, the normalized projection of the vector separating \mathbf{x} and \mathbf{x}_{aim} into the plane orthogonal to the local ξ_3 vector, in accordance with LCS existence criterion (2.28c). A visual representation of this direction field is given in figure 3.5. The choice of initial conditions for computing trajectories within the manifold, with a view to expanding it, is the topic of (the immediately forthcoming) section 3.6.1.

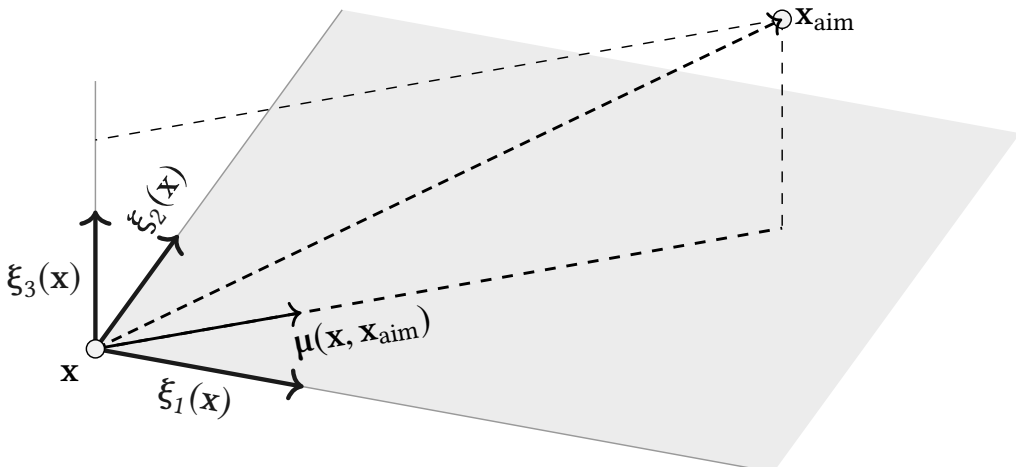


Figure 3.5: Visualization of the direction field used to compute trajectories within a manifold, using the legacy approach. The normalized direction $\mu(\mathbf{x}, \mathbf{x}_{\text{aim}})$ is found by normalizing the projection of $\mathbf{x}_{\text{aim}} - \mathbf{x}$ into the plane spanned by the local ξ_1 - and ξ_2 vectors (shaded).

3.6.1 Selecting initial conditions from which to compute new mesh points

As suggested by Krauskopf et al. (2005), the starting point for all trajectories intended to reach \mathbf{x}_{aim} could be chosen as any point not equal to $\mathbf{x}_{i,j}$ along the parametrized curve C_i .

However, trajectories starting out at points along C_i which are far removed from $\mathbf{x}_{i,j}$ are likely to require a long integration path, which would result in an increase in the accumulated numerical round-off error. Subject to such errors, these trajectories might not even get close to \mathbf{x}_{aim} with a reasonable computational resource consumption. Accordingly, we limited the potential number of trajectories to compute by only considering a subset of the interpolation curve C_i as initial conditions, as follows:

$$\mathbf{x}_{\text{init}} = C_i(\check{s}), \quad \check{s} \in \{[s_j - \varsigma, s_j) \cup (s_j, s_j + \varsigma]\}, \quad 0 < \varsigma \leq \frac{1}{2}, \quad (3.18)$$

where the inherent periodicity of the (quasi-)arclength parametrization of C_i is implicitly applied. Here, ς was set to 0.1, ensuring that 20 % of all possible initial conditions along C_i were considered.

For computing trajectories whose initial conditions are given by equation (3.18) and direction fields given by equation (3.17), the Dormand-Prince 8(7) adaptive ODE solver (cf. table 2.4 and section 3.3.2) was the method of choice. In particular, the dynamic integration step size adjustment meant that we did not need to treat the integration step itself as a degree of freedom (of which there are many, as will be revealed shortly). However, in order to ensure that any trajectory did not overstep the half-plane $\mathcal{H}_{i,j}$ in passing, the step length was continuously limited from above by $\|\mathbf{x}_{\text{aim}} - \mathbf{x}\|$. Moreover, in order to avoid spending unreasonable computational resources on trajectories which for practical purposes never would result in acceptable, new mesh points, the total allowed integration arclength was limited by a scalar multiple of the initial separation $\|\mathbf{x}_{\text{init}} - \mathbf{x}_{\text{aim}}\|$. In particular, this limitation meant that trajectories which ended in stable orbits around \mathbf{x}_{aim} were not allowed to keep going indefinitely.

If any trajectory terminated in a point \mathbf{x}_{fin} which lied within the half-plane $\mathcal{H}_{i,j}$ at a distance Δ_i from $\mathbf{x}_{i,j}$, then \mathbf{x}_{fin} was used as coordinates for a new mesh point $\mathcal{M}_{i+1,j}$. Numerically, these checks were implemented by means of tolerance parameters, as comparing floating-point numbers for equivalence is prone to numerical round-off error. More precisely, a point \mathbf{x} was said to lie within $\mathcal{H}_{i,j}$ provided that

$$\boldsymbol{\eta} := \frac{\mathbf{x} - \mathbf{x}_{i,j}}{\|\mathbf{x} - \mathbf{x}_{i,j}\|}; \quad |\langle \boldsymbol{\eta}, \mathbf{t}_{i,j} \rangle| < \gamma_{\mathcal{H}}, \quad (3.19)$$

whereas

$$\left| \frac{\|\mathbf{x} - \mathbf{x}_{i,j}\|}{\Delta_i} - 1 \right| < \gamma_{\Delta} \quad (3.20)$$

sufficed for it to be flagged as lying a distance Δ_i from $\mathbf{x}_{i,j}$, with $\gamma_{\mathcal{H}}$ and γ_{Δ} small numbers. When a trajectory first intersected $\mathcal{H}_{i,j}$, the integration was stopped abruptly, leaving its endpoint \mathbf{x}_{fin} as its suggested coordinates for the new mesh point. As briefly mentioned in section 3.5.2, the unit tangent vectors $\mathbf{t}_{i,j}$ were generally inherited — the treatment of special cases will be explained in greater detail in section 3.8.1. Figure 3.6 depicts a few characteristic trajectory patterns which commonly occurred when searching for new mesh points in the fashion discussed in the above.

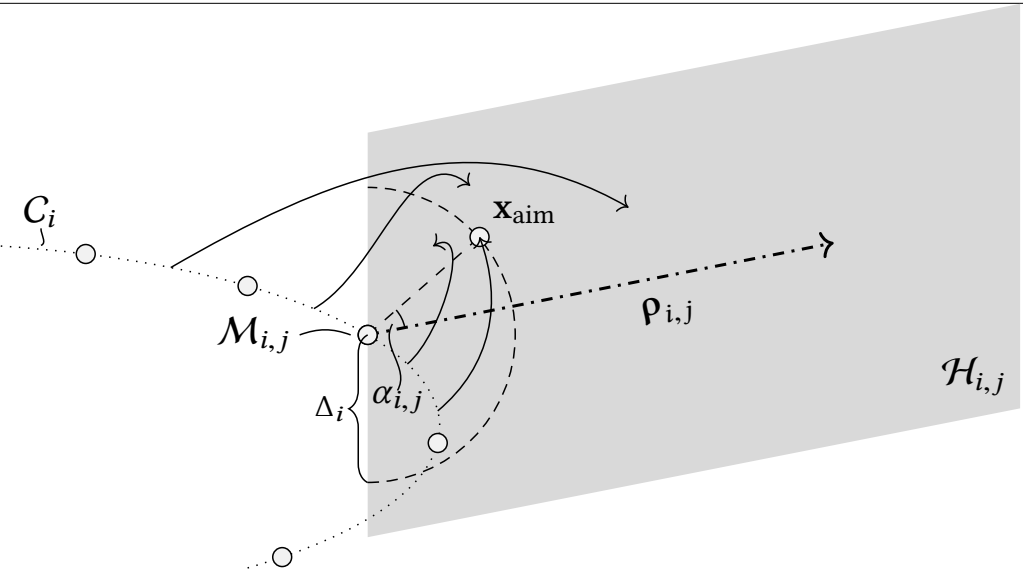


Figure 3.6: Visualization of typical trajectories used to compute a new mesh point, using the legacy approach. The aim point x_{aim} is used to guide trajectories which are locally orthogonal to the ξ_3 direction field (cf. equation (3.17)) towards the intersection between the manifold \mathcal{M} and the half-plane $\mathcal{H}_{i,j}$ (shaded), in order to find a new mesh point $\mathcal{M}_{i+1,j}$ located a distance Δ_i from $\mathcal{M}_{i,j}$. $\mathcal{H}_{i,j}$ is defined by the point $x_{i,j}$ (that is, the coordinates corresponding to the mesh point $\mathcal{M}_{i,j}$), its unit normal $t_{i,j}$ (not shown) and the (quasi-)radial unit vector $\rho_{i,j}$ (dashdotted). The half-circle of radius Δ_i , centered in $x_{i,j}$ and lying within $\mathcal{H}_{i,j}$, on which we seek to find a new mesh point, is dashed. All permitted trajectory initial positions lie along the smooth parametrized curve C_i (dotted), and are given by equation (3.18). A select few trajectories are shown, where the arrowheads indicate the first intersection with $\mathcal{H}_{i,j}$ (as per equation (3.19)), after which the integration was terminated.

3.6.2 Choosing new trajectory start points by an algorithm with memory

Our method of choosing parameter values \check{s} corresponding to points along C_i (cf. equation (3.18)), from which to compute trajectories of the direction field given by equation (3.17) — with the intention of computing new mesh points — rests on the assumption that

$$\Delta(\check{s}) := \|\mathbf{x}_{\text{fin}}(\check{s}) - \mathbf{x}_{i,j}\|, \quad \mathbf{x}_{\text{fin}} \in \mathcal{H}_{i,j} \quad (3.21)$$

is a continuous function of \check{s} . To this end, we keep track of why each computed trajectory is terminated. In particular, we first note whether or not each trajectory, corresponding to a start point $\mathbf{x}(\check{s})$, ends up at some point $\mathbf{x}_{\text{fin}} \in \mathcal{H}_{i,j}$. If this is the case, we also note whether the separation $\Delta(\check{s})$ (defined in equation (3.21)) corresponding was an over- or undershoot compared to the desired separation Δ_i .

Based on the premises outlined above, we then make use of the intermediate value theorem; specifically, if we have

$$\Delta(\check{s}_1) < \Delta_i, \quad \Delta(\check{s}_2) > \Delta_i \quad (3.22a)$$

for $\check{s}_1 < \check{s}_2$, then the intermediate value theorem implies that we must have

$$\Delta(\check{s}) = \Delta_i, \quad \check{s}_1 < \check{s} < \check{s}_2, \quad (3.22b)$$

under the assumption that $\Delta(\check{s})$ is a continuous function. In order to optimize our use of computational resources, we thus endeavor to take large steps when moving along C_i whenever the computed intersections with $\mathcal{H}_{i,j}$ are far from fulfilling $\Delta(\check{s}) = \Delta_i$. However, when a subinterval of C_i within which the intermediate value theorem suggests that a trajectory may fulfill our requirements is identified, we decrease the (quasi-)arclength increment $\delta\check{s}$ in order to increase our odds of finding said trajectory. The increment $\delta\check{s}$ was not allowed to decrease beyond a pre-set $\delta\check{s}_{\min}$, nor to increase beyond a pre-set $\delta\check{s}_{\max}$. The latter limitation was made in order to avoid bypassing subsets of C_i from which two or more trajectories satisfy $\Delta(\check{s}) = \Delta_i$. Overstepping any region containing an even number of such intersections could render it undetectable using our intermediate value theorem-based approach, as no change in trajectory termination status need be detected.

The feedback received by tracking why each trajectory is terminated, allows us to dynamically select new trajectory start points along C_i . We do so by increasing the (quasi-)arclength increment $\delta\check{s}$ as long as there is no change in trajectory termination status, and, conversely, backtracking and reducing $\delta\check{s}$ when a status change is detected. This process is shown schematically in figure 3.7. Note that our algorithm is not perfect; theoretical closed loops exist (left for the interested reader to find, as an exercise¹). However, in our experience, the iterative search process never became stuck beyond recovery; likely due to the direction field (see equation (3.17)) yielding well-behaved trajectories (and, possibly, numerical round-off error). As we assume asymptotic behaviour close to any regions in which $\Delta(\check{s})$ is not defined (that is, regions where no trajectories reach the half-plane $\mathcal{H}_{i,j}$, cf. equation (3.21)), the adjustment of $\delta\check{s}$ is treated in the same fashion there.

3.6.3 Handling failures to compute satisfactory mesh points

As mentioned in section 3.6.1, it can never be guaranteed that any trajectories which start out at some point along the smooth curve C_i will be able to generate a new mesh point located within $\mathcal{H}_{i,j}$ which simultaneously satisfies all of our defined constraints. Missing out on points in any freshly generated level set prohibits the generation of more level sets – in particular, partly dependent on the number of successfully computed points, the smoothness of the interpolation curve C_{i+1} exhibits a critical dependence on *all* of the points used for its creation. Accordingly, handling tricky mesh points is crucial.

Although it remains impossible to *ensure* that the trajectory-based approach to compute new mesh points comes to fruition, the success rate can be increased significantly by responding appropriately to an initially failed search. Our strategy of choice is based upon adjusting the computed aim point incrementally. Specifically, given the initial angular offset $\alpha_{i,j}$ of \mathbf{x}_{aim} along the semicircle of radius Δ_i , with regards to the guidance vector $\rho_{i,j}$ (see figure 3.6), we perturb \mathbf{x}_{aim} along said semicircle by the forced alteration

$$\alpha_{i,j} := \alpha_{i,j} + \delta\alpha, \quad (3.23a)$$

¹Hint: What would happen if the very first computed trajectory failed to intersect with $\mathcal{H}_{i,j}$?

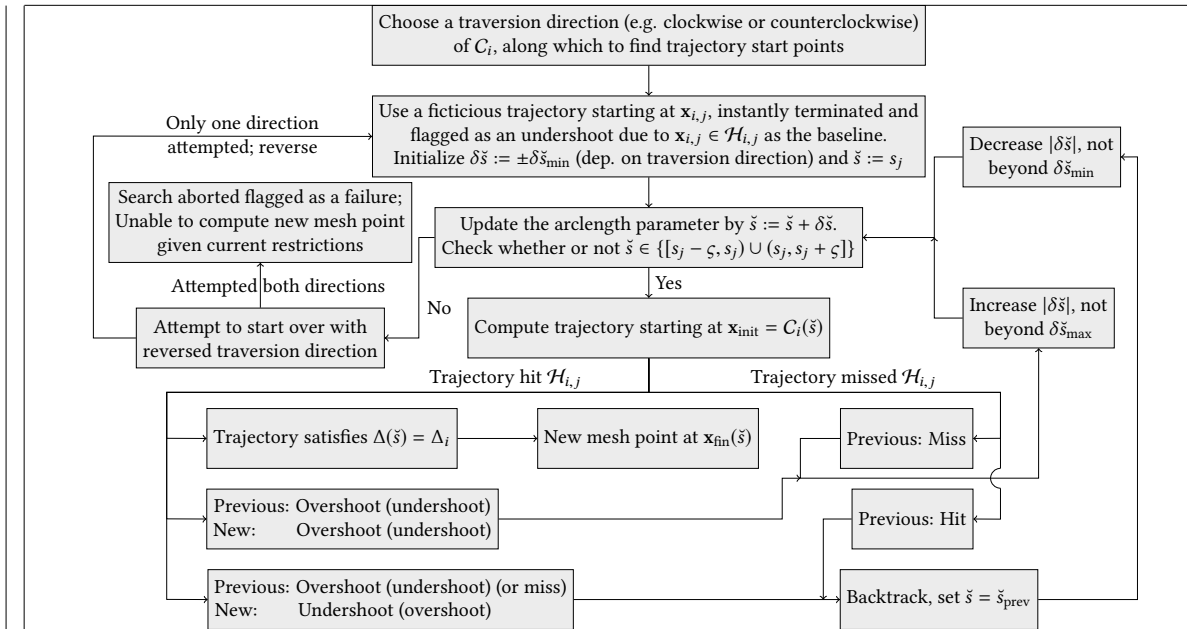


Figure 3.7: Flowchart illustrating the algorithm for iteratively choosing new trajectory start points based on the termination status of the preceding trajectories, using the legacy approach. All possible trajectory start points are contained within a subset of C_i , per equation (3.18). Whether or not a given trajectory intersected with the half-plane $\mathcal{H}_{i,j}$, and satisfied $\Delta(\check{s}) = \Delta_i$, was determined using equations (3.19) and (3.20).

with

$$|\delta\alpha| \leq \delta\alpha_{\max}. \quad (3.23b)$$

Note that the range of offsets – determined by $\delta\alpha_{\max}$ – should be chosen based on the expected geometry of the manifold as a whole; in contrast to the number of attempted angular offsets, which should be guided by considerations pertaining to the availability of computational resources.

Repeating the iterative point search algorithm outlined in the entirety of the current section (that is, section 3.6) for all possible perturbation configurations of \mathbf{x}_{aim} , given by equation (3.23), however, still does not guarantee that an acceptable mesh point is found. Should that be the case, the entire algorithm – including angular perturbations as outlined in the above – is then rerun with simultaneously and progressively relaxed point acceptance criteria. That is, the numerical tolerance parameters γ_H and γ_Δ (cf. equations (3.19) and (3.20)) are gradually increased up to pre-set maximum values γ_H^{\max} and γ_Δ^{\max} .

If, after having increased said tolerance parameters to their maximal permitted values, we were unable able to find an ‘acceptable’ mesh point, the incomplete level set was promptly discarded, and attempted to be computed anew with reduced Δ_i (more on the adjustment procedure for Δ_i to follow in section 3.8.3). Should an entire, new geodesic level set not be computable even with the minimum permitted step length, attempts at expanding the computed manifold further were abandoned; constrained by the given (maximal) tolerance parameters, the method simply would not be able to expand the computed manifold any

further. The various other stopping criteria for the generation of manifolds will be described in detail in section 3.10.

3.7 REVISED APPROACH TO COMPUTING NEW MESH POINTS

The version of the method of geodesic level sets presented by Krauskopf et al. (2005) is centered around computing manifolds defined by being everywhere tangent to some three-dimensional vector field (as a concrete example of application, Krauskopf et al. seek to compute the strange attractor of the Lorenz system). As noted by Oettinger and Haller (2016), repelling LCSs in 3D consist of subsets of manifolds defined by being everywhere orthogonal to the ξ_3 direction field – which is reflected in existence criterion (2.28c). Thus, compared to the type of systems considered by Krauskopf et al., we have an extra degree of freedom when seeking to identify repelling LCSs in 3D; in particular, moving along a manifold in arbitrary directions within a planes orthogonal to the local ξ_3 vector is allowed, in contrast to being constrained to moving back and forth along a curve. The paragraphs (and sections) to follow will reveal how we utilized the additional degree of freedom to reduce the number of calculations necessary to compute new mesh points.

The overarching principles, nevertheless, remain the same. Like for the legacy approach presented in section 3.6, mesh points in level set \mathcal{M}_{i+1} are computed from the points in the prior level set \mathcal{M}_i . Similarly, the considerations to follow rely on each mesh point $\mathcal{M}_{i,j}$ having inherited its tangential vector from its direct ancestor; namely, $\mathbf{t}_{i,j} := \mathbf{t}_{i-1,j}$. How the special cases of this inheritance-based approach were treated, will be described in greater detail in section 3.8.1. Moreover, from the mesh point $\mathcal{M}_{i,j}$, we wish to place a new mesh point $\mathcal{M}_{i+1,j}$ at an intersection of the manifold \mathcal{M} and the half-plane $\mathcal{H}_{i,j}$ located a distance Δ_i from $\mathcal{M}_{i,j}$. As usual, $\mathcal{H}_{i,j}$ is defined by the coordinate $\mathbf{x}_{i,j}$, the unit normal $\mathbf{t}_{i,j}$ and the guidance vector $\mathbf{p}_{i,j}$ (the latter of which is defined in equations (3.13) and (3.14)).

3.7.1 Computing pseudoradial trajectories directly

Completely analogously to the legacy approach outlined in section 3.6, we define a local direction field as

$$\Psi(\mathbf{x}) = \frac{\xi_3(\mathbf{x}) \times \mathbf{t}_{i,j}}{\|\xi_3(\mathbf{x}_0) \times \mathbf{t}_{i,j}\|}, \quad (3.24)$$

where $\mathbf{t}_{i,j}$ is the unit tangent associated with the mesh point $\mathcal{M}_{i,j}$. Here, however, we make explicit use of our previously mentioned additional degree of freedom – namely that trajectories within the parametrized manifold are allowed arbitrary movements within the planes which are locally orthogonal to the ξ_3 direction field, rather than being constrained to moving along a three-dimensional curve – by computing the coordinates of the new mesh point $\mathcal{M}_{i+1,j}$ as the end point of a *single* trajectory.

Any trajectory starting out within the half-plane $\mathcal{H}_{i,j}$ and moving in the direction field given by equation (3.24) is certain to remain within it, as the direction field is everywhere orthogonal to its unit normal $\mathbf{t}_{i,j}$. That is, as long as the direction field used in computing

said trajectory is everywhere oriented radially outwards. Accordingly, we computed a single trajectory in the aforementioned direction field, starting out at $\mathbf{x}_{\text{init}} = \mathbf{x}_{i,j}$, using the Dormand-Prince 8(7) adaptive ODE solver (see table 2.4 and section 3.3.2), where all of the vectors of the intermediary Runge-Kutta steps were corrected, if necessary, by continuous comparison with $\rho_{i,j}$ and sign-reversion if an intermediary vector was directed radially inwards.

Should the ξ_3 direction be parallel to the unit tangent $\mathbf{t}_{i,j}$ locally along the trajectory, the direction field equation (3.24) would become undefined. In such regions, we allowed the Runge-Kutta solver to take a step in the previous direction as was used for the immediately preceding step. Numerically, such regions were recognized by

$$\|\xi_3(\mathbf{x}) \times \mathbf{t}_{i,j}\| < \gamma_{\parallel}, \quad (3.25)$$

where γ_{\parallel} is a small tolerance parameter. Like for the legacy approach (as outlined in section 3.6, the self-correcting integration step length meant that we did not treat the integration step as a degree of freedom, and, in order to avoid overstepping, the step length of the Dormand-Prince solver was continuously limited from above by $\|\mathbf{x} - \mathbf{x}_{i,j}\| - \Delta_i$. Moreover, the total allowed integration arclength was limited to an integer multiple — that is, γ_{arc} — of the interstep Δ_i allowing for the termination of any (hypothetical) trajectory which would end up in a stable orbit.

The trajectory integration was immediately interrupted upon reaching a point \mathbf{x}_{fin} separated from $\mathbf{x}_{i,j}$ by a distance Δ_i . Like for the legacy approach, this criterion was checked by means of a tolerance parameter, seeing as directly comparing floating-point numbers is prone to numerical round-off error. In particular, if a point \mathbf{x} satisfied

$$\left| \frac{\|\mathbf{x} - \mathbf{x}_{i,j}\|}{\Delta_i} - 1 \right| < \gamma_{\Delta}, \quad (3.26)$$

with γ_{Δ} being a small number, the point was flagged as lying a distance Δ_i from $\mathbf{x}_{i,j}$. Thus, upon reaching a point satisfying equation (3.26), the trajectory was terminated, and the new mesh point $\mathcal{M}_{i+1,j}$ was placed at the trajectory end point \mathbf{x}_{fin} . Figure 3.8 depicts a typical trajectory used to compute new mesh points in the fashion discussed in the above.

3.7.2 Handling failures to compute satisfactory mesh points

Much like the legacy approach outlined in section 3.6, it can never be guaranteed that all of the computed trajectories will yield new, acceptable mesh points — moreover, missing out on points in a level set prohibits the generation of more level set. In particular, our procedure for maintaining mesh accuracy (which will be outlined in section 3.8.1) makes extensive use of the interpolation curves $\{C_i\}$. As the smoothness of the interpolation curve C_{i+1} depends on *all* of the points used for its creation, proper handling of tricky mesh points remains critically important.

Seeing as the only tolerance parameter involved in this method pertains to achieving the desired separation between a meshpoint and its direct descendant — see equation (3.26) — we

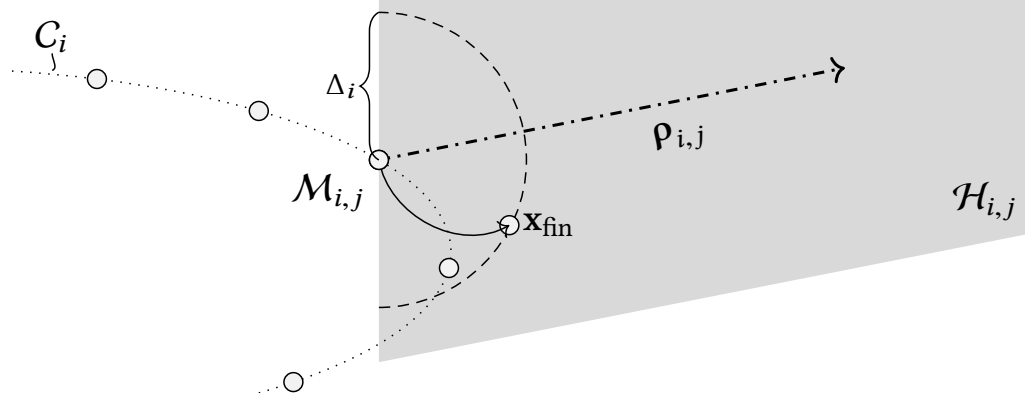


Figure 3.8: Visualization of a typical trajectory used to compute a new mesh point, using the revised approach. A trajectory is computed, starting at $\mathbf{x}_{i,j}$ (that is, the coordinates corresponding to the mesh point $\mathcal{M}_{i,j}$) and moving in the direction field given by equation (3.24), in order to find a new mesh point at the intersection between the manifold \mathcal{M} and the half-plane $\mathcal{H}_{i,j}$ (shaded), located a distance Δ_i from $\mathcal{M}_{i,j}$. $\mathcal{H}_{i,j}$ is defined by the point $\mathbf{x}_{i,j}$, its unit normal $\mathbf{t}_{i,j}$ (not shown) and the (quasi-)radial unit vector $\rho_{i,j}$ (dashdotted). The half-circle of radius Δ_i , centered in $\mathbf{x}_{i,j}$ and lying within $\mathcal{H}_{i,j}$, on which we seek to find a new mesh point, is dashed. As soon as a trajectory reaches a point separated from $\mathcal{M}_{i,j}$ by a distance Δ_i (per equation (3.26)), the integration is stopped, and a new mesh point $\mathcal{M}_{i+1,j}$ (not shown) is placed at the trajectory end point \mathbf{x}_{fin} .

elected not to progressively relax this constraint. Instead, we interpreted the failure of any trajectory to reach a point sufficiently far away, as the trajectory being coiled such that the required integration arc length to yield a point sufficiently far away from the ancestor mesh point pre-set allowed path length. Accordingly, the incomplete level set was discarded, and attempted to be recomputed with reduced Δ_i (for which the dynamic adjustment procedure will be described in detail in section 3.8.3). Should an entire, new geodesic level set prove incomputable even at the minimum permitted step length, attempts at further expansion of the computed manifold were abandoned. In such cases, this variant of the method of geodesic level sets simply did not suffice, for the given set of development parameters. Details on other stopping criteria for the generation of manifolds will be presented in section 3.10.

3.7.3 Key improvements of the revised algorithm for computing new mesh points

When compared to the convoluted way of computing new mesh points presented in section 3.6, it is readily apparent that the revised approach is significantly less complex. In particular, note how launching a single trajectory starting at the ancestor mesh point results in the legacy algorithm for computing new trajectory start points iteratively (cf. figure 3.7) is rendered entirely superfluous. Moreover, as all computed trajectories necessarily remain within the target half-planes, no tolerance parameter for detecting intersections between

trajectories and half-planes is needed. In short, the revised algorithm is conceptually simpler, and involves a lesser number of free (tolerance) parameters.

Simple numerical experiments confirmed that, given the same initial conditions and underlying direction fields, the two approaches yielded the same mesh points — at least, within rounding error. Moreover, these tests also revealed that the revised algorithm is usually two orders of magnitude quicker (in terms of computational runtime). Unsurprisingly, the main time expenditure of the legacy approach turned out to be the computation of elusive mesh points; often, several thousand computed trajectories were needed before a satisfactory new point was found. In particular, the probability of finding an acceptable mesh point depends sensitively on choosing an appropriate aim point — leading to significant slowdowns in regions wherein the underlying manifold behaves erratically.

For its superior speed and simplicity, the revised approach of forced pseudoradial trajectories became our method of choice. Accordingly, all of our results (which will be presented in chapter 4) were generated with this method. Note that, while deemed inferior in the context of identifying repelling LCSs in three-dimensional flow, the legacy approach of guided trajectories remains a valid way of computing three-dimensional manifolds. Thus, it can be used as a baseline for computing other kinds of three-dimensional manifolds defined in a different manner than repelling LCSs — which remains beyond the scope of this project.

3.8 MANAGING MESH ACCURACY

As will be described extensively in section 3.9, the manifold \mathcal{M} was extracted from its set of parametrization point $\{\mathcal{M}_{i,j}\}$ by means of linear interpolation. In order to keep the interpolation error in check, we sought to bind the distance separating neighboring mesh points by means pre-set upper and lower boundaries, in the following denoted Δ_{\min} and Δ_{\max} , respectively. Considered as a holistic approximation of a manifold, the separations between the mesh points in each level set, combined with the inter-set step lengths $\{\Delta_i\}$, determine the overall accuracy. Our algorithmic approach to maintaining the overall mesh quality will be explained in the sections to follow.

3.8.1 *Maintaining mesh point density*

When expanding a manifold by computing new geodesic level sets, the distance separating neighboring mesh points within each subsequent level set generally increases. This is due to the mesh points being a parametrization of what is essentially an expanding topological circle. Having successfully computed a new geodesic level set — that is, having found a descendant point $\mathcal{M}_{i+1,j}$ for each of the ancestor points $\{\mathcal{M}_{i,j}\}$ — by use of the method outlined in section 3.7 we then inspected all of the distances separating nearest neighbors.

If any of the separations between nearest neighbors exceeded Δ_{\max} , we sought to insert a new mesh point inbetween. Specifically, if $\|\mathbf{x}_{i+1,j} - \mathbf{x}_{i+1,j+1}\| > \Delta_{\max}$, a new mesh point $\mathcal{M}_{i+1,j+\frac{1}{2}}$ was computed, using the method described in section 3.7 by launching a trajectory

starting from a fictitious ancestor point $\mathcal{M}_{i,j+\frac{1}{2}}$, located midway inbetween $\mathcal{M}_{i,j}$ and $\mathcal{M}_{i,j+1}$ along the interpolation curve C_i . As the fictitious mesh point $\mathcal{M}_{i,j+\frac{1}{2}}$ does not itself have a direct ancestor from which to inherit a unit tangent, $\mathbf{t}_{i,j+\frac{1}{2}}$ was instead constructed by normalizing the arithmetic average of $\mathbf{t}_{i,j}$ and $\mathbf{t}_{i,j+1}$, and passed on to $\mathcal{M}_{i,j+\frac{1}{2}}$. The fictitious mesh point's guidance vector $\mathbf{p}_{i,j+\frac{1}{2}}$ was constructed in similar fashion — its role in the dynamic update of the interset separation Δ_i will be described in detail in section 3.8.3. This way, the interpolation error is limited; no new mesh points are generated using interpolations (in intermediary computations) over intervals of length exceeding Δ_{\max} .

Conversely, if any of the nearest neighbor separations became smaller than Δ_{\min} , we sought to remove one of them, as long as the distance separating mesh points which would then become nearest neighbors did not exceed Δ_{\max} . Accordingly, if any one of a pair of neighboring mesh points was to be removed, we chose to discard the one which would result in the smallest separation between the ensuing, *new* pair of nearest neighbors. Our principles for inserting new mesh points inbetween others, and removing grid points which are too close together, are illustrated in figure 3.9.

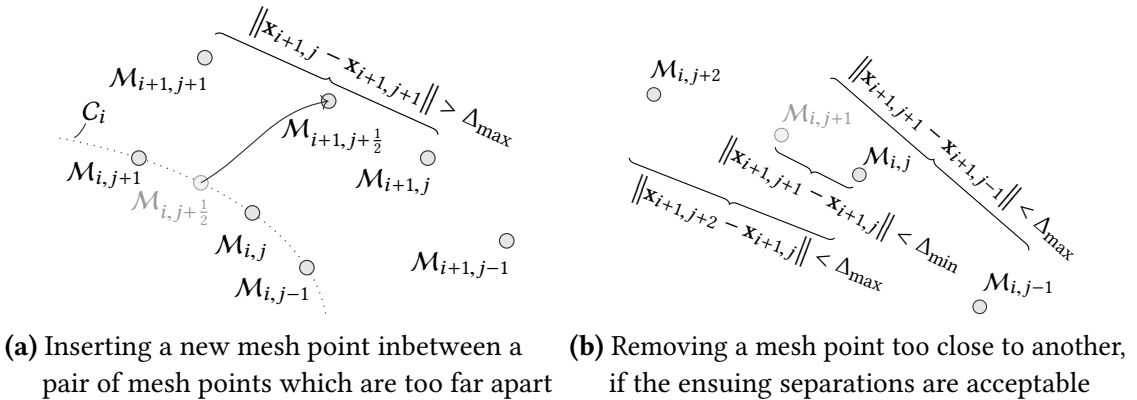


Figure 3.9: Our approach to inserting new, or removing, mesh points to maintain mesh point density. When two neighboring mesh points in a freshly computed level set are too far apart with regards to the given mesh parameter Δ_{\max} , we attempt to insert a new mesh point between them. As shown in (a), this is done by using the method described in section 3.7, using a fictitious initial condition midway inbetween the two ancestor mesh points $\mathcal{M}_{i,j}$ and $\mathcal{M}_{i,j+1}$ along the interpolated curve C_i , indicated in the figure by a lighter shade of gray. Should two neighboring mesh points be too close together, and one of the two can be removed without the resulting sets of neighboring points being too far apart, we remove the one which results in the shortest interpoint separation (as shown in (b), where the point which is removed is indicated with a lighter shade of gray).

3.8.2 Limiting the accumulation of numerical noise

Early tests with regards to the generation of manifolds revealed that the compound numerical error over the course of many level sets often resulted in irregular behaviour. Specifically, small bulges in the mesh easily became amplified in the subsequent level sets, which frequently caused unwanted loops in the interpolation curves $\{C_i\}$ which extended far from

the manifold epicentre. Occasionally, this would lead to the generated manifold to fold into itself. This *cannot* happen in repelling LCSs. In particular, self-intersecting manifolds indicate that, in a small neighborhood of any intersection, there would not be a well-defined direction of strongest repulsion, which would violate LCS existence criterion (2.28a).

As a countermeasure against the formation of undesired loops within a level set, we reviewed a recently computed (suggestion for a) geodesic level set, as follows: Consider a point $\mathcal{M}_{i+1,j}$ located at $\mathbf{x}_{i+1,j}$. If, for any point $\mathcal{M}_{i+1,j+k}$ with $k > 1$, the interpoint distances satisfy

$$\Delta_{\min} < \|\mathbf{x}_{i+1,j+k} - \mathbf{x}_{i+1,j}\| < \Delta_{\max} \quad (3.27a)$$

and

$$\|\mathbf{x}_{i+1,j+k} - \mathbf{x}_{i+1,j}\| < \gamma_{\cup} \sum_{\kappa=0}^{k-1} \|\mathbf{x}_{i+1,j+\kappa+1} - \mathbf{x}_{i+1,j+\kappa}\|, \quad (3.27b)$$

then all mesh points $\{\mathcal{M}_{i+1,j+\kappa}\}_{\kappa=1}^{k-1}$ are removed. Here, $0 \leq \gamma_{\cup} \leq 1$ is a bulge tolerance parameter, which essentially determines an upper limit for the extent (measured in cumulative arclength) of loop-like segments of any given interpolation curve C_i . Specifically, a large γ_{\cup} facilitates removal of rounded loops, whereas a small γ_{\cup} restricts the removal process to sharp bulges. A characteristic example demonstrating this method of removing unwanted loops is shown in figure 3.10. While possibly sacrificing some resolution of the manifold as a whole, adhering to criterion (3.27) prevents the removal of any *reasonable* bulge formations. As no new mesh points are *added* as a direct consequence of this loop-removal algorithm, it does not introduce new errors. It is also worth mentioning that some of the removed mesh points were recovered in the ensuing level sets, then as constituents of an overall smoother level set.

3.8.3 A curvature-based approach to determining interset separations

Given the interpoint separation constraints described in section 3.8.1, we have some flexibility regarding the choice of interset step length Δ_i . In an approach closely mirroring that of Krauskopf et al. (2005), we used the (approximate) local curvatures along each point strain (i.e., the set of mesh points which can be traced back to a common ancestor) in order to determine whether or not the local manifold dynamics were resolved to a satisfactory level of detail. Starting out with an initial interset separation $\Delta_1 = 2\Delta_{\min}$ for the second innermost level set (i.e., the first level set which was computed using the method described in section 3.7), we sought to ensure that the subsequent Δ_i resulted in the encapsulation of the finer details of the growing manifolds.

Specifically, once all mesh points which constitute a geodesic level set \mathcal{M}_{i+1} have been identified, all a distance Δ_i away from their direct ancestor points in the previous level set \mathcal{M}_i , we computed the angular offsets $\alpha_{i,j}$ of each pair of guidance vectors $\rho_{i,j}$ and $\rho_{i+1,j}$ (as defined in equations (3.13) and (3.14)). This is sketched in figure 3.11. If

$$\alpha_{i,j} > \alpha_{\downarrow} \quad \text{or} \quad \Delta_i \cdot \alpha_{i,j} > (\Delta\alpha)_{\downarrow} \quad \text{for at least one } j, \quad (3.28)$$

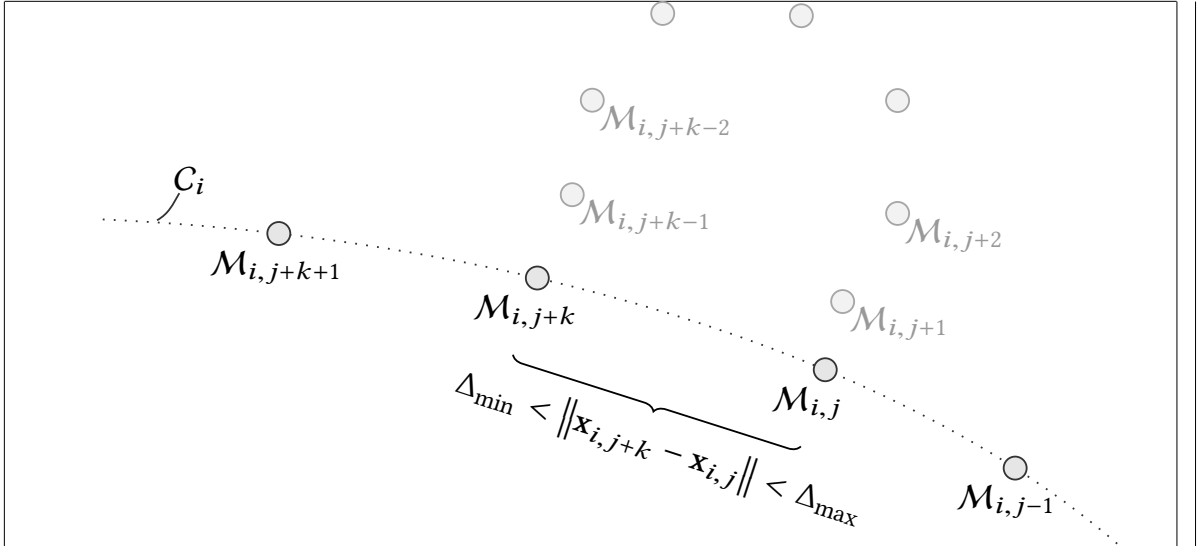


Figure 3.10: Our approach to limit the compound numerical error, by continuously removing unwanted loops in the computed level sets. As the separation between the mesh points $\mathcal{M}_{i,j}$ and $\mathcal{M}_{i,j+k}$ satisfies the restrictions regarding mesh point density (cf. section 3.8.1), the mesh points $\{\mathcal{M}_{i,j+k}\}_{k=1}^{k-1}$ (shown in a lighter shade of gray) are removed, provided that the cumulative neighbor separation around the bulge is sufficiently large (per the conditions presented in equation (3.27)) – which is the case in the above. The resulting interpolation curve C_i becomes significantly more well-behaved without the superfluous mesh points.

where α_\downarrow and $(\Delta\alpha)_\downarrow$ are upper curvature tolerance parameters, was satisfied, the level set \mathcal{M}_{i+1} was discarded and recomputed with reduced Δ_i . If Δ_i was already as low as the pre-set Δ_{\min} , the manifold generation process was terminated, as a new level set \mathcal{M}_{i+1} could not be computed under the given constraints on interpoint separation (cf. section 3.8.1). Conversely, if

$$\alpha_{i,j} < \alpha_\uparrow \quad \text{and} \quad \Delta_i \cdot \alpha_{i,j} < (\Delta\alpha)_\uparrow \quad \text{for all } j, \quad (3.29)$$

where α_\uparrow and $(\Delta\alpha)_\uparrow$ are lower curvature tolerance parameters, was satisfied, the interset distance for computing the *next* level set, Δ_{i+1} , was made bigger than Δ_i (although never beyond the pre-set Δ_{\max}).

As is evident from equations (3.28) and (3.29), the parameters α_\downarrow , α_\uparrow , $(\Delta\alpha)_\downarrow$ and $(\Delta\alpha)_\uparrow$ determine the mesh adaption along point strains. Choosing appropriate bounds for the offsets $\{\Delta_i \cdot \alpha_{i,j}\}$ allows for stricter requirements on angular offsets for large interstep lengths. Similarly, level sets computed using small interset lenghts are allowed (comparatively) larger angular offsets in general. In our experience, the interset step lenghts were rarely *increased* – typically, there would be one or more subsets of the mesh points constituting any given level set which underwent sufficient curvature such that condition (3.29) did not hold.

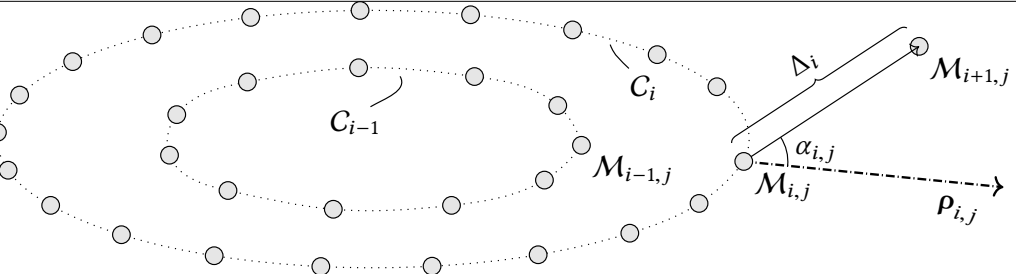


Figure 3.11: The principles of curvature-guided interset step length adjustment. For each of the mesh points $\{M_{i+1,j}\}$ constituting the level set M_{i+1} , the angular offsets $\alpha_{i,j}$ between the guidance vectors $p_{i,j}$ (dashdotted) and $p_{i+1,j}$ (not shown, but parallel to the vector separating $M_{i,j}$ and $M_{i+1,j}$, shown in solid) were computed. These were used in conjunction with Δ_i , the interset step used to compute the new mesh points, in order to determine whether or not the suggested level set would have to be discarded due to the local curvature along at least one point strain being sufficiently large to comply with criterion (3.28). If the level set was deemed acceptable, local curvature estimates $\{\alpha_{i,j}\}$ and $\{\Delta_i \cdot \alpha_{i,j}\}$ were then used to determine if the subsequent level set M_{i+2} could be computed using $\Delta_{i+1} > \Delta_i$; namely, if criterion (3.29) was satisfied.

3.9 CONTINUOUSLY RECONSTRUCTING MANIFOLD SURFACES FROM POINT MESHES IN 3D

While expanding the point mesh parametrization of a manifold \mathcal{M} in bundles constituting geodesic level sets, we attempt to reproduce its fully three-dimensional structure by simultaneously interpolating inbetween the mesh points. Our main objective for representing manifolds as continuous interpolation objects is visual representation (in addition to the detection of self-intersections, as will be outlined in section 3.10.1)—accordingly, we do not provide any form of analytical expression for \mathcal{M} 's surface. Moreover, as high order interpolation schemes are complicated considerably by the irregular structure inherent to the parametrization of \mathcal{M} as a sequence of level sets, linear interpolation became our method of choice.

To our knowledge, all three-dimensional plotting algorithms rely on some sort of triangulation method to regularize a pointwise parametrized surface. General-purpose routines for triangulation generation were found to be unsuitable, due to the specific mesh structure of \mathcal{M} , arising from the parametrization by geodesic level sets. For instance, Delaunay triangulation not only resulted in omitting triangles which, to the naked eye, were crucial for the overall manifold structure, but also generated a lot of undesirable surface triangles—a problem which became increasingly prominent near creases. Accordingly, we made use of the fact that the `plot_trisurf` routine from the Python plotting library Matplotlib accepts an optional input argument specifying a list of triangles to plot, given by their vertices, and made our own triangulation scheme based on the specific structure of the mesh point parametrization of the computed manifolds.

We begin by fixing a traversal direction, specifying the order in which the triangles are

created. Starting with the innermost level set, we then specify the sets of vertices for a set of triangles which together cover the (approximate) surface between the manifold epicentre \mathbf{x}_0 and C_1 (see figure 3.4). When a new geodesic level set \mathcal{M}_{i+1} satisfies the accuracy constraints outlined in section 3.8, we move along the mesh points constituting C_{i+1} in the selected direction, adding new triangles covering the (approximate) surface area between the interpolation curves C_i and C_{i+1} .

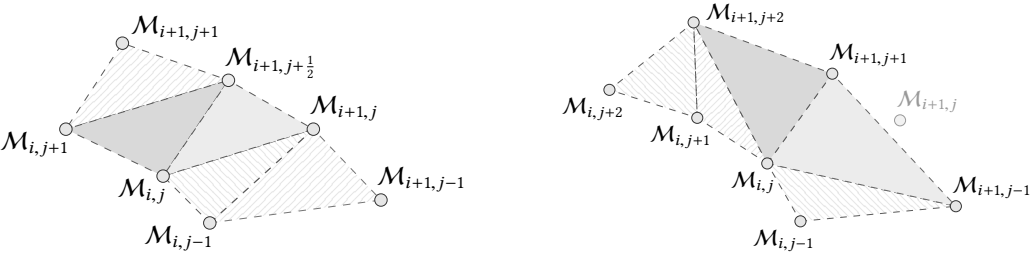
The surface area enclosed by the innermost level set was simply reconstructed by forming the triangles whose vertices are given as $\{\mathbf{x}_0, \mathbf{x}_{1,j}, \mathbf{x}_{1,j+1}\}$. Our treatment of the ensuing level sets is best described in terms of the local triangles formed around a single mesh point $\mathcal{M}_{i,j}$. The base case, that is, when no (nearby) points in the level set \mathcal{M}_{i+1} have been removed nor added inbetween direct descendants in order to maintain the overall mesh point quality (cf. sections 3.8.1 and 3.8.2) is handled by demanding that the triangles associated with $\mathcal{M}_{i,j}$ cover the tetragon surface element with vertices given by $\{\mathbf{x}_{i,j}, \mathbf{x}_{i,j+1}, \mathbf{x}_{i+1,j+1}, \mathbf{x}_{i+1,j}\}$. Accordingly, we add two triangles with vertices given by $\{\mathbf{x}_{i,j}, \mathbf{x}_{i+1,j}, \mathbf{x}_{i+1,j+1}\}$ and $\{\mathbf{x}_{i,j}, \mathbf{x}_{i,j+1}, \mathbf{x}_{i+1,j}\}$, respectively. Note that, in generating tetrads in this fashion for each point in each level set, triangles which connect the mesh point $\mathcal{M}_{i,j}$ to all of its neighbors are formed.

The special cases not involving a one-to-one correspondence between the mesh points in \mathcal{M}_i and \mathcal{M}_{i+1} require special attention. This occurs whenever mesh points are inserted by making use of fictitious ancestors, or when mesh points are removed, in order to maintain the mesh point density (cf. section 3.8.1) – or, when removing unwanted bulges in order to dampen the effects of compound numerical noise (as described in section 3.8.2). The treatment of these special cases is shown in figure 3.12, and will be outlined in greater detail in the upcoming paragraph. In particular, note how all of $\mathcal{M}_{i,j}$'s nearest neighbors in the surrounding level set \mathcal{M}_{i+1} are used in the triangulations.

When an extra mesh point $\mathcal{M}_{i+1,j+\frac{1}{2}}$ is inserted inbetween $\mathcal{M}_{i+1,j}$ and $\mathcal{M}_{i+1,j+1}$, the tetragonal surface element whose vertices are located at $\{\mathbf{x}_{i,j}, \mathbf{x}_{i,j+1}, \mathbf{x}_{i+1,j}, \mathbf{x}_{i+1,j+\frac{1}{2}}\}$ is approximated by means of two triangles. Again expressed in terms of their vertices, these are $\{\mathbf{x}_{i,j}, \mathbf{x}_{i+1,j}, \mathbf{x}_{i+1,j+\frac{1}{2}}\}$ and $\{\mathbf{x}_{i,j}, \mathbf{x}_{i+1,j}, \mathbf{x}_{i,j+1}\}$. In the event that the mesh point $\mathcal{M}_{i+1,j}$ was removed, either as part of an undesired bulge or in order to preserve mesh density, the tetragonal surface with vertices at $\{\mathbf{x}_{i,j}, \mathbf{x}_{i,j+1}, \mathbf{x}_{i+1,j-1}, \mathbf{x}_{i+1,j+1}\}$ is constructed using two triangles, with vertices at $\{\mathbf{x}_{i,j}, \mathbf{x}_{i+1,j-1}, \mathbf{x}_{i+1,j+1}\}$ and $\{\mathbf{x}_{i,j}, \mathbf{x}_{i+1,j+1}, \mathbf{x}_{i,j+1}\}$, respectively. If more than one intermittent mesh point is removed, the treatment is completely analogous, occasionally resulting in some triangle elements being significantly larger than its neighbors.

3.10 MACROSCALE STOPPING CRITERIA FOR THE EXPANSION OF COMPUTED MANIFOLDS

In principle, the process of developing manifold approximations by adding more and more mesh points, organized in geodesic level sets, would continue as long as the overall mesh quality was conserved (cf. section 3.8). The enforced (pseudo-)uniform expansion radially outwards, inherent to the method of geodesic level sets, would then yield a mesh providing a



(a) Including mesh points with fictitious ancestors in the triangulation

(b) Triangulating with the resulting nearest neighbors, if a mesh point is removed

Figure 3.12: How our triangulation algorithm handled the special cases arising when the one-to-one correspondence between the points in subsequent level sets was broken. In (a), a mesh point is inserted inbetween the points $\mathcal{M}_{i+1,j}$ and $\mathcal{M}_{i+1,j+1}$, while, in (b), the mesh point $\mathcal{M}_{i+1,j}$ is removed. Both of these adjustments were made in order to maintain the density of mesh points (cf. section 3.8.1). The ensuing pair of triangles which are computed when considering the triangulations from $\mathcal{M}_{i,j}$, are shaded. The remaining triangles (patterned) arise when triangulating from different points in level set \mathcal{M}_i . Note that the removal of bundles of mesh points in order to dampen the effect of numerical noise (which introduces bulges, as described in section 3.8.2) is treated analogously to the case of single missing points.

conservative estimate of the size of the *actual* manifold, as there is no particular reason to expect it to expect the manifold to appear homogeneous, when viewed for the epicentre of the computed level sets. With reasonable parameter choices, we became able to generate large manifolds quite quickly. This lead us to enforce two additional types of stopping criteria, based on what would happen if the computed manifolds reached the edges of the computational domain, or folded into themselves — where the latter of the two will be described in the imminent section 3.10.1

The trajectories which are computed in order to identify new mesh points (per the method described in section 3.7) frequently overstep the domains within which the Cauchy-Green strain eigenvalues and -vectors are defined in order to compute mesh points on or near the domain boundaries. Thus, in order to resolve the behaviour of manifolds near the edges of the domain of interest, the aforementioned strain characteristics need to be computed in a region which *contains* the domain of interest, expanding beyond it in all directions. This is how we treated the case of tidal flow in the Førde fjord (as outlined in section 3.2). For perfectly periodic flow systems, such as (either variant of) the ABC flow — described in section 3.1 — this reduces to the trivial exercise of utilizing the inherent periodicity (that is, provided that the computational domain is sufficiently large to encompass at least one cycle along each direction).

3.10.1 Continuous self-intersection checks

Per LCS existence criterion (2.28a), there must be a uniquely defined direction of strongest repellence everywhere along a repelling LCS. Furthermore, our method of expanding

manifolds by adding mesh points organized in geodesic level sets (cf. section 3.7) is based on continuous expansions(pseudo-)radially outwards from the manifold epicentre. Accordingly, the intersection of any manifold with itself was interpreted as a nonphysical artefact of accumulated numerical error. For that reason, we sought to terminate the expansion of a manifold when self-intersections were detected.

Our method of detecting manifold self-intersections is based on comparing the continuously computed interpolation triangles (as described in section 3.9) – in particular, we compared each triangle which was added together with the most recently computed level set, to all of the triangles which had been added with the preceding level sets. If at least one pair of triangles intersected, the newest level set was flagged as self-intersecting. Our way of determining whether or not two triangles intersect, is based on the Möller-Trumbore ray-triangle intersection algorithm, with a detection sensitivity parameter $\epsilon = 10^{-8}$ (Möller and Trumbore 1997). A visual representation of our triangle-intersection algorithm is available in figure 3.13.

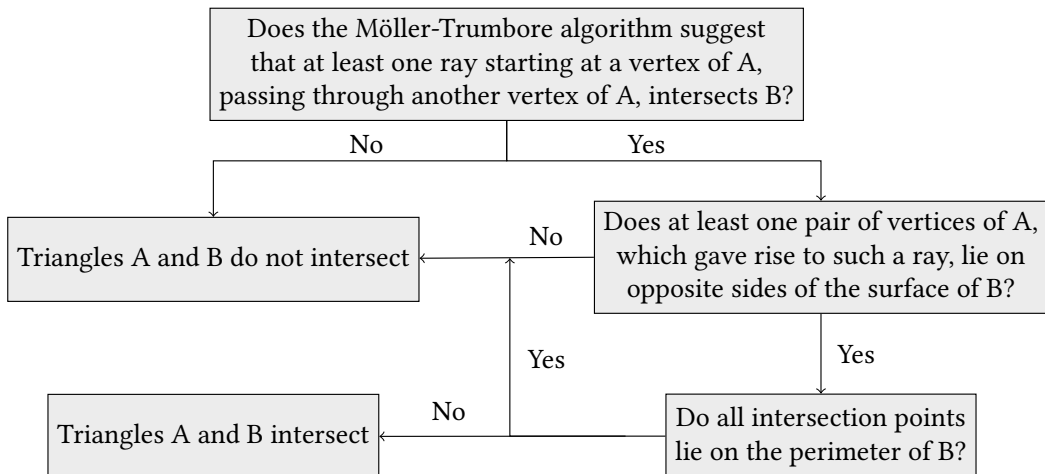
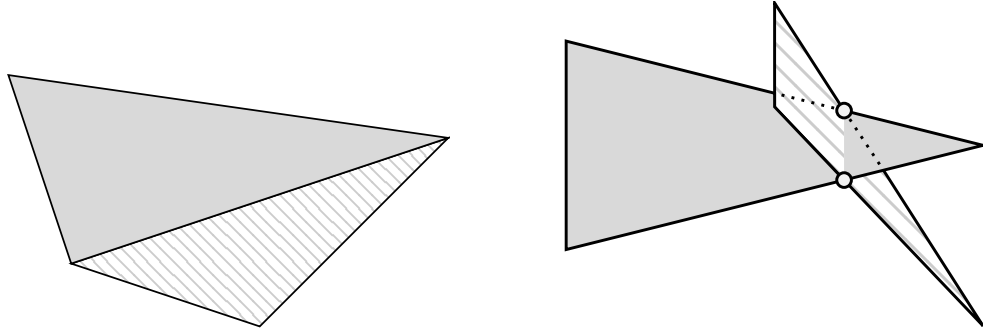


Figure 3.13: Flowchart illustrating the algorithm for detecting self-intersections. In order to ensure that no self-intersection went unnoticed, the indicated procedure was carried out by comparing each of the interpolation triangles A in the most recently computed level set, to all of the triangles B in the previously computed level sets. Provided that any of the new triangles intersected any of the old ones, the new level set as a whole was flagged as self-intersecting. How this intersection-detection approach handled a set of special cases is illustrated in figure 3.14.

Some special cases of intersecting triangles warrant special treatment. In particular, as our triangulation method (outlined in section 3.9) is based on generating triangles which share sides with its neighbors, we decided to allow triangles to intersect along the edges. Similarly, we allowed for two triangles to be identical – which might happen if a manifold folds onto itself perfectly. Our algorithmic way of treating these cases resulted in a theoretical false negative; namely, the case of two triangles intersecting in exactly two points, laying along the edges of *both* triangles. In our experience, however, this never proved problematic – should one pair of triangles happen to intersect in this exact fashion (which is a rarity in itself due to numerical round-off errors), another pair of triangles would intersect in such

a way that the most recently added set as a whole would be flagged as self-intersecting. Two of the aforementioned special cases – that is, two triangles sharing an edge, and two triangles intersecting in exactly two points laying along the edges of both triangles – are shown in figure 3.14.



(a) Two triangles sharing an edge, normally treated as a continuous intersection (b) Two triangles whose edges intersect in exactly two unique points

Figure 3.14: How the intersection-detection algorithm handles special cases. Triangles which share a common edge, as illustrated in (a), form the premise of our triangulation algorithm; accordingly, this scenario does not get flagged as an intersection. Neither does the case when two triangles are identical (or one is contained within the other) – which is not shown here – nor the case when the edges of two triangles intersect in exactly two unique points, shown in (b). The latter is a very marginal case which hardly ever occurs, and, for our purposes, would invariably coincide with another (nearby) pair of triangles intersecting in a different manner than these special cases; ensuring that the computed level set as a whole would be flagged as self-intersecting.

Initial tests revealed that some self-intersections were quite innocuous, in that, if the computed manifold was expanded by an additional level set, the newly added triangulations need not necessarily intersect with any of the preceding ones. This kind of insipid intersections could be a consequence of the linear nature of our triangulation method, possibly compounded by round-off error. Accordingly, we decided to stop the manifold expansion process if *several consecutive* geodesic level sets introduced intersection triangulations. This was done by computing the sum of the interset distances $\{\Delta_i\}$ for each consecutive level set $\{\mathcal{M}_i\}$ which introduced new intersections. Whenever this pseudo-intersection length exceeded $5 \cdot \Delta_{\min}$ (cf. section 3.8.1), we terminated the manifold computation process; empirical trials suggested that the intersection issue would then only worsen if more mesh points were added.

3.11 IDENTIFYING LCSS AS SUBSETS OF COMPUTED MANIFOLDS

The collection of manifolds computed by means of the method outlined in the preceding sections, starting from an approximately even distribution of points in the \mathcal{U}_0 domain (cf. section 3.5 and, in particular, table 3.2), are all surfaces which satisfy LCS existence criterion (2.28c) – that is, they are everywhere perpendicular to the local direction of maximal repulsion. In order to extract repelling LCSSs from these parametrized surfaces, we then identified the regions of the manifolds – represented as a subset of the mesh points in

their parametrization — which also satisfy the remaining existence criteria; namely, (2.28a), (2.28b) and (2.28d). This was done completely analogously to how we identified the grid points belonging within the \mathcal{U}_0 domain, as outlined in section 3.5.1. In particular, each mesh point $M_{i,j}$ of a computed manifold \mathcal{M} was flagged as to whether or not it satisfied all of the aforementioned existence criteria.

We then proceeded to construct a repelling LCS \mathcal{L} from the mesh points of \mathcal{M} . Per section 3.5.1, the mesh point at the centre of any given manifold always satisfies all the LCS existence criteria; accordingly, it was added as the first mesh point \mathcal{L}_0 of the extracted LCS. Going through the list of the remaining mesh points $M_{i,j}$ which satisfied all LCS criteria, we added a manifold mesh point to the set of LCS points provided that

$$\|x_{i,j} - \tilde{x}_\kappa\| < \gamma_\square \Delta_{\max} \quad (3.30)$$

holds for at least one κ , where $x_{i,j}$ and \tilde{x}_κ denote the coordinates of mesh point $M_{i,j}$ and the already accepted LCS point $\mathcal{L}_\kappa \in \{\mathcal{L}_k\}$, respectively. Δ_{\max} is the maximum allowed mesh point separation used for computing the manifold (cf. section 3.8.1), while the scalar parameter $\gamma_\square \geq 1$ allows for extracting smoother LCSs, more well-suited for visualization purposes — as will be made clear shortly. Subsequently, all mesh points *not* satisfying all of the LCS existence criteria were added to the set of LCS points, provided that they comply with a similar distance threshold as given in equation (3.30), where we only computed mesh point separations relative to the LCS points which satisfied all of the existence criteria (thus not to any point added to the LCS, for which this was not the case).

The tolerance parameter γ_\square thus allowed us to mitigate possible numerical error; in particular, if any given mesh point was slightly perturbed away from the underlying manifold, it could still end up being a part of the LCS. Finally, we looked at all of the surface elements pertaining to the triangulation of the manifold \mathcal{M} (as described in section 3.9) in conjunction with the set of mesh points which had been recognized as belonging to the LCS \mathcal{L} . If mesh points corresponding to two of the three vertices defining a triangular surface element had been recognized as part of \mathcal{L} , we then added the mesh point corresponding to the last remaining vertex to the set of LCS points $\{\mathcal{L}_k\}$. Accordingly, the triangulations of the \mathcal{M} were reused for \mathcal{L} . These slight relaxations of the LCS existence criteria facilitate the extraction of smoother LCS surfaces are favorable for the visual representation of LCSs. Moreover, they mitigate the possible effects of numerical error perturbing any given mesh point $M_{i,j}$ away from the *actual* manifold — leaving it more than sufficiently close to the manifold for visualization purposes — by possibly allowing it to be included as part of the LCS after all. Figure 3.15 shows an example of extracting a repelling LCS from a computed manifold.

The extracted LCS surfaces \mathcal{L} , parametrized as a set of mesh points $\{\mathcal{L}_k\}$, represent three-dimensional surfaces which — allowing for a little numerical error — comply with all of the existence criteria for repelling LCSs, as originally proposed by Haller (2011). Inspired by the work of Farazmand and Haller (2012a), we then sought to dispose of the smallest among the computed LCSs, as these are expected to be the least significant in terms of the overall flow within the system. In order to obtain a measure of the size of our three-dimensional surfaces,

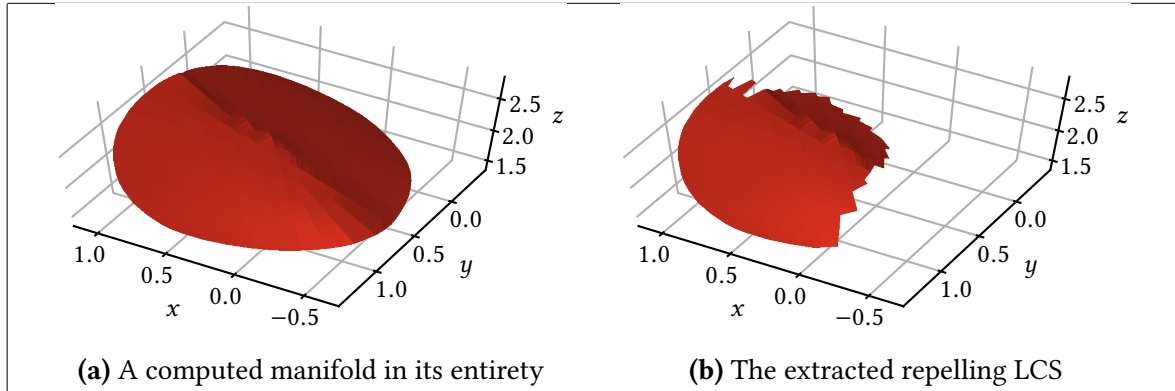


Figure 3.15: An example of a repelling LCS extracted as a subset of a computed manifold. In (a), a sample manifold for the steady ABC flow is shown, whereas (b) shows the subset of the manifold which satisfies the LCS existence criteria given in equation (2.28) (or lies sufficiently close to any point satisfying these criteria, meaning that their inclusion facilitates triangulations which provide an overall enhanced visual representation).

to each LCS point \mathcal{L}_k , we assigned a weighting given by the surface area approximating the region of the underlying manifold \mathcal{M} that is closer to the corresponding mesh point $\mathcal{M}_{i,j}$ than any others. To the mesh point located at the manifold epicentre \mathbf{x}_0 , we assigned the weight $\mathcal{W}_0 = \pi(\delta_{\text{init}}/2)^2$. The weights of all other mesh points were computed as

$$\mathcal{W}_k := \mathcal{A}_{i,j} \approx \frac{\Delta_i + \Delta_{i-1}}{2} \cdot \frac{\|\mathbf{x}_{i,j+1} - \mathbf{x}_{i,j}\| + \|\mathbf{x}_{i,j} - \mathbf{x}_{i,j-1}\|}{2}, \quad (3.31)$$

where, as always, $\mathbf{x}_{i,j}$ denotes the coordinates of mesh point $\mathcal{M}_{i,j}$. This surface approximation is illustrated in figure 3.16. These weights were also used to compute a repulsion average $\bar{\lambda}_3$; in particular,

$$\mathcal{W} = \sum_k \mathcal{W}_k, \quad \bar{\lambda}_3 = \frac{1}{\mathcal{W}} \sum_k \lambda_3(\tilde{\mathbf{x}}_k) \mathcal{W}_k, \quad (3.32)$$

where the summation is over all mesh points in the parametrization of \mathcal{L} , and $\tilde{\mathbf{x}}_k$ denotes the coordinates of mesh point \mathcal{L}_k . Any LCS for which the computed total weight \mathcal{W} was smaller than some pre-set limit \mathcal{W}_{\min} or $\bar{\lambda}_3 < 1$, the latter as a sanity check to ensure overall repulsion, per existence criterion (2.28a), were discarded.

3.12 MAKING THE MOST OF THE AVAILABLE COMPUTATIONAL RESOURCES

The simultaneous solution of twelve coupled ODEs involved in the advection of tracers in order to compute the (directional derivatives of the) flow map (cf. section 3.3) quickly proved an unreasonably strenuous task for the author's own personal laptop. Seeing as the available memory was the main limitation, we parallelized this computation by means of MPI, and ran it on NTNU's supercomputer, Vilje. In spite of the tracers being independent, we elected to utilize MPI over alternative multiprocessing tools in order to access multiple nodes within the Vilje cluster. Due to the problem's pleasingly parallel nature, the parallelization process consisted of distributing an approximately even amount of tracers across all ranks,

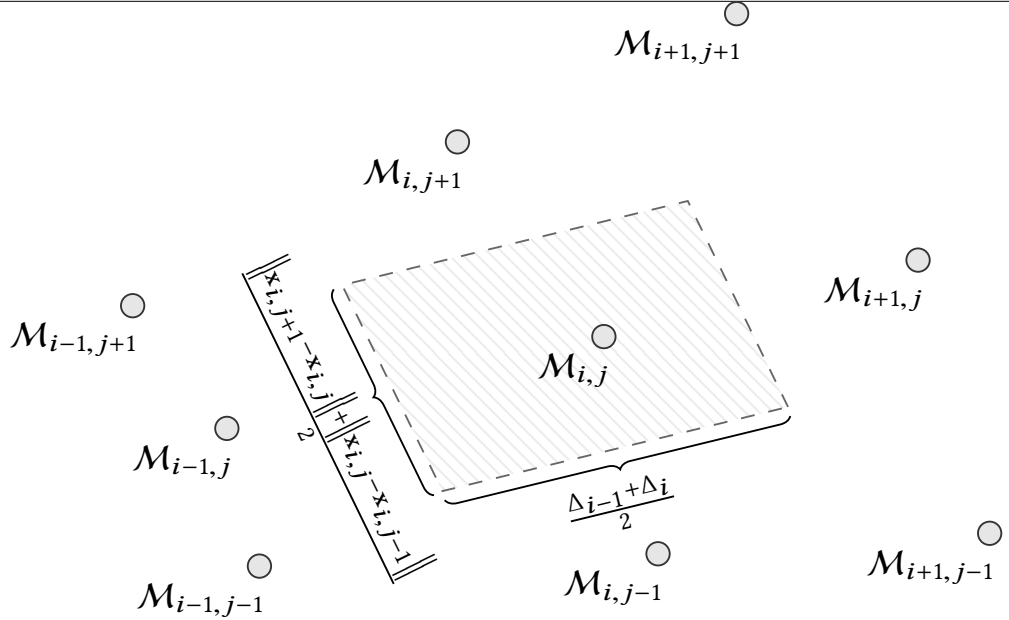


Figure 3.16: Our way of assigning weights to mesh points in computed LCSs. To a given LCS point \mathcal{L}_k , we assigned a weight given by a rectangular approximation of the surface area closer to the corresponding manifold mesh point $\mathcal{M}_{i,j}$ than all other point in the parametrization of the manifold \mathcal{M} (shaded). Here, Δ_i corresponds to the interset step length used to create level set \mathcal{M}_{i+1} , based on level set \mathcal{M}_i , (see section 3.7), while $\mathbf{x}_{i,j}$ denotes the coordinates of mesh point $\mathcal{M}_{i,j}$.

whereupon each rank advected (that is, simultaneously solved the twelve coupled ODEs for all of) its allocated tracers. In the end, all of the final state flow map Jacobians were collected by the designated main process (i.e, rank = 0), whereupon the Cauchy-Green strain eigenvalues and -vectors were extracted by means of a SVD decomposition (as outlined in section 3.4).

Regarding the generation of manifolds, code profiling (unsurprisingly) revealed that the generation of new mesh points by computing (pseudo-)radial trajectories orthogonal to the ξ_3 -direction field was a great source of time expenditure. Accordingly, we rewrote all numerical routines pertaining to the generation of new mesh points in Cython. In particular, we made use of highly optimized, low-level BLAS² routines whenever possible. Because of the ever increasing number of necessary triangle comparisons in our algorithm of detecting manifolds which self-intersect (as described in section 3.10.1), all of the accompanying numerical methods were expressed in Cython, too. Similarly to how we exposed the Bspline-Fortran library to Python (cf. section 3.2.2), we also consistently used calls by reference in order to avoid unnecessary memory duplication. Overall, the transition from (NumPy-based) Python to Cython for the most significant tasks reduced the overall runtime by two orders of magnitude.

Analogously to the advection of tracers, we made use of the mutual independence of the

²See www.netlib.org/blas and https://docs.scipy.org/doc/scipy/reference/linalg.cython_bla.html

computed manifolds to accelerate their computation by means of MPI parallelization across the Vilje cluster. We elected to make a one-to-one correspondence between the number of MPI threads and the number of manifolds to generate (as described in section 3.5.1), thus allowing each manifold to grow as large as possible before being stopped due to the one of the criteria imposed in section 3.10. Compared to the advection of tracers, or the expansion of manifolds, the extraction of repelling LCSs as subsets of the computed manifolds (cf. section 3.11) was not a particularly laborious task. Thus, we chose to parallelize this selection process by making use of the Python multiprocessing library, as access to a single node in the Vilje cluster sufficed to complete it in less than a minute.

4 Results

4.1 VERIFYING OUR METHOD OF GENERATING MANIFOLDS

4.1.1 An analytical test case

As a verification test case for (our variant of) the method of geodesic level sets to compute three-dimensional manifolds, we sought to reproduce a three-dimensional surface defined by

$$z = g(x, y) = A \sin(\omega_x x) \sin(\omega_y y) + z_0, \quad (4.1a)$$

which can be expressed as the zeros of the scalar function

$$f(\mathbf{x}) = g(x, y) - z, \quad (4.1b)$$

where \mathbf{x} denotes the Cartesian coordinate vector (x, y, z) . In order to do so, we computed its unit normal vector field as

$$\mathbf{n}(\mathbf{x}) = \frac{\nabla f(\mathbf{x})}{\|\nabla f(\mathbf{x})\|}, \quad (4.2)$$

which we then substituted for the ξ_3 -direction field in equation (3.24). Here, we chose the parameters

$$A = 1, \quad \omega_x = \omega_y = 2, \quad z_0 = \pi \quad (4.3)$$

and used a single initial position $\mathbf{x}_0 = (\pi, \pi, \pi)$ from which to develop the surface, by subsequently adding mesh points organized in level sets, as outlined in sections 3.7–3.10.

Specifically, we computed a total of seven surface approximations, using the parameter values provided in table 4.1 with different values of Δ_{\min} , thereby different mesh point densities. Four of the resulting manifolds are shown in figure 4.1. Although all of the presented manifolds successfully encapsulate the macroscale behaviour of the underlying surface (given by equations (4.1) and (4.3)), increasing the mesh point density clearly facilitates more accurate approximations. In particular, some of the visual discrepancies of figure 4.1 can be attributed to the linear interpolation inherent to our triangulation scheme (see section 3.9).

In order to obtain a quantitative measure of how an increase in the mesh point density impacts the accuracy of the overall approximation, we computed the root mean square (hereafter abbreviated to RMS) error of each mesh point as

$$\text{err}_{\text{RMS}} = \sqrt{\frac{1}{N} \sum_{i,j} |z_{i,j} - g(x_i, y_j)|^2}, \quad (4.4)$$

where we sum over all of the N computed points, with $g(x, y)$ given by equation (4.1) (and equation (4.3)). The RMS error is shown as a function of the mesh point density in figure 4.2. It appears to scale quadratically with Δ_{\min} , the smallest permitted separation between neighboring mesh points – which doubles as a measurement of the overall mesh density.

Note that, due to the local (pseudo-)planar nature of the parametrization of manifolds by means of points organized in level sets, the number of mesh points in the parametrization of

Table 4.1: Parameter values used to approximate an analytically known three-dimensional surface (see equations (4.1) and (4.3)) by the method of geodesic level sets. Note that while we varied the overall mesh point density by altering Δ_{\min} and Δ_{\max} , we kept the ratio between them constant.

Parameter	Value	Description
δ_{init}	10^{-3}	Separation of innermost geodesic level set from the manifold epicentre, cf. figure 3.4
$\Delta_{\min}, \Delta_{\max}$	$\frac{\Delta_{\max}}{\Delta_{\min}} = 4$	(Variable) boundaries for interpoint separations (details found in section 3.8.1)
Δ_1	$2\Delta_{\min}$	Interset distance used to compute the second geodesic level set (see sections 3.7 and 3.8.3)
γ_{Δ}	$5 \cdot 10^{-3}$	Tolerance for the separation of a mesh point from its ancestor (per equation (3.26))
γ_{arc}	5	Sets an upper limit to trajectory lengths as $\gamma_{\text{arc}}\Delta_i$ (briefly mentioned in section 3.7.1)
$\gamma_{\circlearrowleft}$	$7 \cdot 10^{-1}$	Sets an upper limit to the extent of loop-like segments of any level set (see section 3.8.2)
α_{\uparrow}	$8.7 \cdot 10^{-2} \text{rad } (5^\circ)$	Used in a curvature-based approach to adjust interset distances (outlined in section 3.8.3)
α_{\downarrow}	$4.4 \cdot 10^{-1} \text{rad } (25^\circ)$	
$(\delta\alpha)_{\uparrow}, (\delta\alpha)_{\downarrow}$	$2\delta_{\max}\alpha_{\uparrow}, 2\delta_{\min}\alpha_{\downarrow}$	

a manifold *increases* quadratically as Δ_{\min} decreases. Thus, the decrease in numerical error comes at the cost of an increased consumption of computational resources. For instance, the method's most computationally costly operations (namely, generating trajectories to identify new mesh points and checking for self-intersections, cf. sections 3.7 and 3.10.1, respectively) need to be performed far more frequently when the number of mesh points increase. Perhaps more crucially, an increased number of mesh points leads to an increase in the required memory. These considerations, together with the ones to follow in the immediately forthcoming section, became the foundation on which we based our choice of mesh point density for the computation of LCSs (which will be elaborated upon in sections 4.3 and 4.4).

4.1.2 Sample manifolds computed from the steady ABC flow

Figure 4.3 shows a sample manifold obtained for the steady ABC flow (cf. section 3.1), computed for a few different mesh point densities, and otherwise similar parameters as were used in order to approximate the sinusoidal surface (see table 4.1 and figure 4.1). From figure 4.3, it is apparent that increasing the mesh point density generally results in increased resolution. However, there appears to be some density threshold, beneath which unwanted numerical artifacts start to emerge. This is particularly evident in figure 4.3d, where the sharp indentation appears to be out of place. Such oddities could be due to accumulation of interpolation error when computing new mesh points from fictitious ancestor points (as described in section 3.8.1) – which naturally occurs more often with increased mesh point

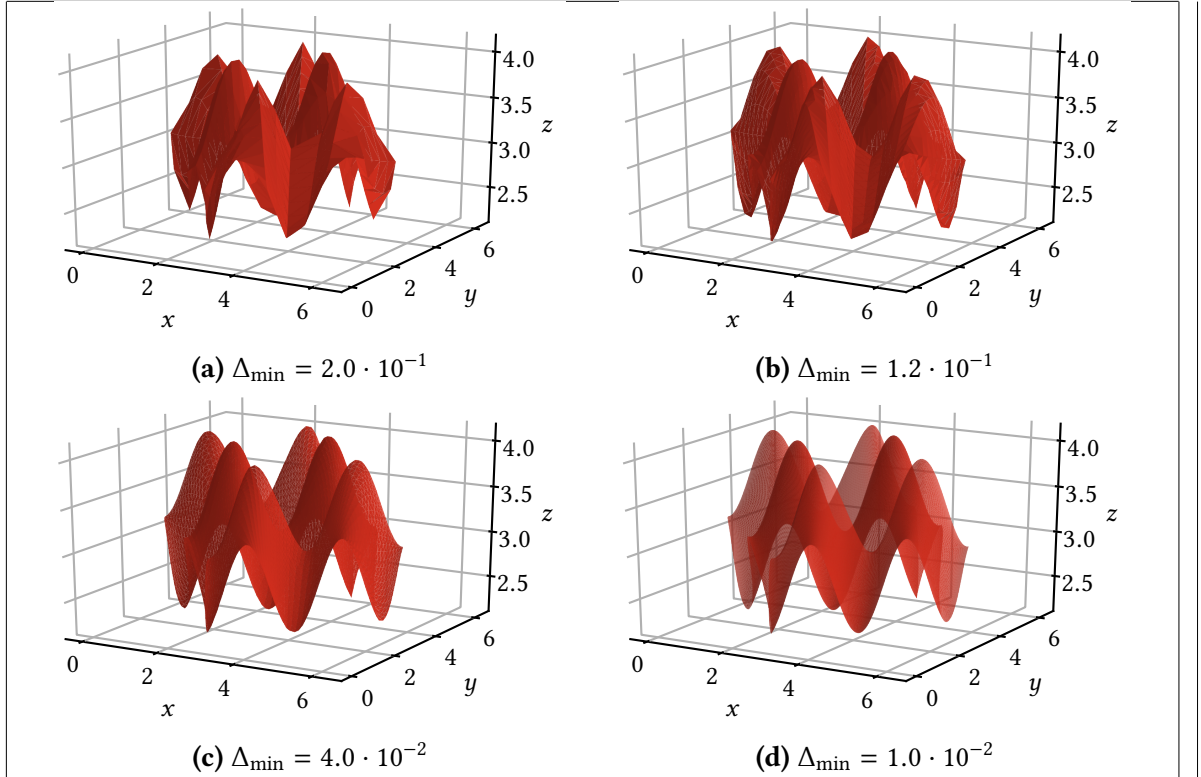


Figure 4.1: Geodesic level set approximation to analytically known three-dimensional surface. The underlying sinusoidal surface is given by equations (4.1) and (4.3). The manifolds were all computed using the parameters given in table 4.1, with varying mesh point densities (given by the value of Δ_{\min}). Each of the approximations were grown from the initial position $\mathbf{x}_0 = (\pi, \pi, \pi)$. Note how all of the manifolds are able to capture the macroscale behaviour of the underlying surface, although the microscale behaviour is increasingly well-resolved when the mesh point density increases.

density. Accordingly, our choice of mesh point density for (both variants of) the ABC flow (which will be presented in table 4.2) was guided by a desire to limit the amount of such oddities, in addition to the memory required in order to store each manifold (as described in section 4.1.1).

Motivated by remark 1, we sought to verify that our computed manifolds, by virtue of containing repelling LCSs, act as invariant manifolds for arbitrary linear combinations of the ξ_1 - and ξ_2 -direction fields. Figure 4.4 shows a sample manifold obtained for the steady ABC flow (described in detail in section 3.1), using the parameter values provided in table 4.2 — the very same that we used in order to compute LCSs in said flow (more to follow in section 4.3). It also shows 200 different trajectories launched from (a small circle laying within the manifold, centered in) the manifold epicentre \mathbf{x}_0 and computed using the Dormand-Prince 8(7) adaptive ODE solver (see table 2.4 and section 3.3.2). In figure 4.4a, the trajectories are solution curves of equation (3.24), where $t_{i,j}$ was kept constant along each trajectory. Meanwhile, figure 4.4b shows solution curves of equation (2.31), for 200 different pairs of weights (a, b) such that the initial trajectory directions were evenly distributed in the plane defined by the coordinate \mathbf{x}_0 and the unit normal $\xi_3(\mathbf{x}_0)$.

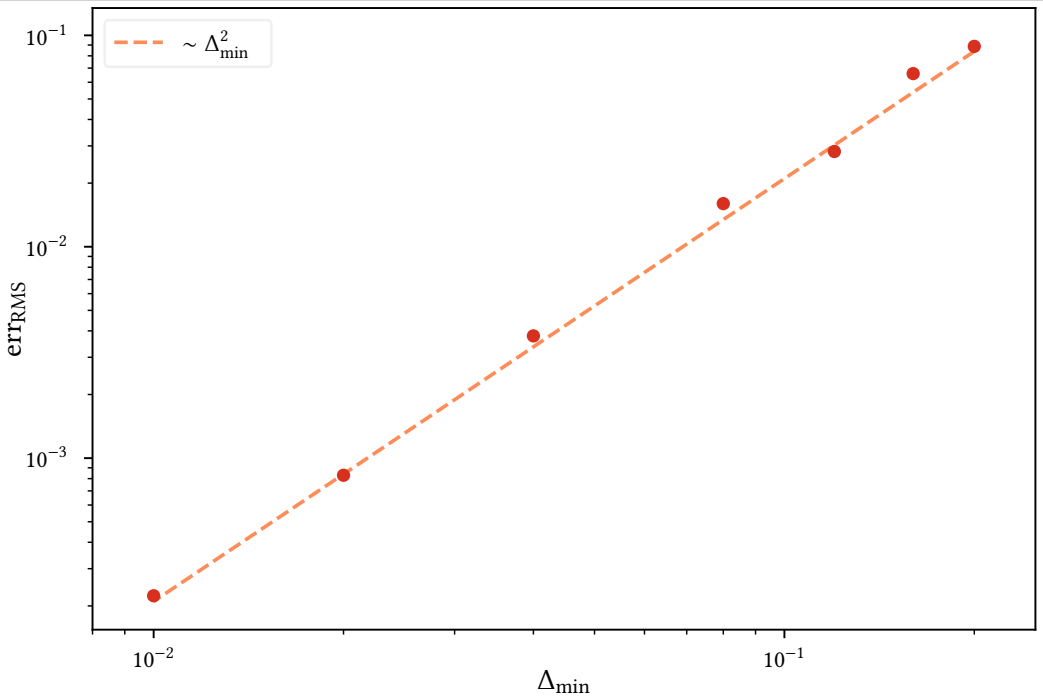


Figure 4.2: RMS error of geodesic level set approximations to analytically known three-dimensional surface, as a function of mesh point density. Using seven different mesh point densities (here denoted by their Δ_{\min}), we computed approximations of the sinusoidal surface defined by equations (4.1) and (4.3) — four of which are shown in figure 4.1 — whose RMS error (as defined in equation (4.4)) are shown as solid dots. Note how the RMS error appears to increase quadratically as a function of the mesh density.

Unsurprisingly, the curves in figure 4.4a all lie within the computed manifold, as all of its constituent mesh points were computed as endpoints of trajectories in a similarly defined direction field (see section 3.7). The same applies for the curves shown in figure 4.4b; however, there seems to be some regions of the manifold which are particularly challenging to hit — signified by a decreased trajectory density — it appears that very specific weights (a, b) are required to reach them. Regardless, none of the computed trajectories ever leave the computed surface, which confirms that the surface *is* in fact an invariant manifold of the ξ_1 - and ξ_2 -direction fields, in compliance with LCS existence criterion (2.28c).

4.2 VERIFYING OUR METHOD OF EXTRACTING LCSs FROM THE COMPUTED MANIFOLDS

4.2.1 An analytical test case

As a verification test case for our way of extracting repelling LCSs from the computed manifolds (which is described in detail in section 3.11), we defined the purely radial velocity field

$$\dot{\mathbf{x}}(t) = \frac{\mathbf{x}}{\|\mathbf{x}\|} \sin \pi(\|\mathbf{x}\| - r), \quad (4.5)$$

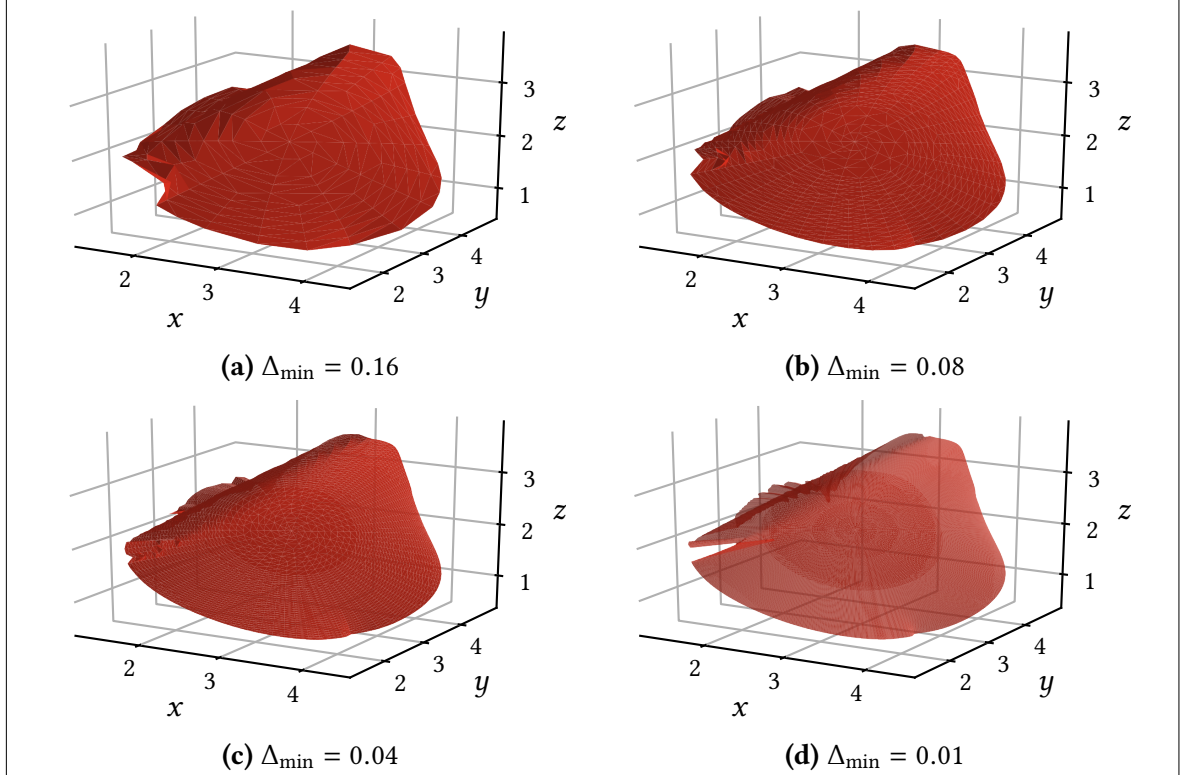
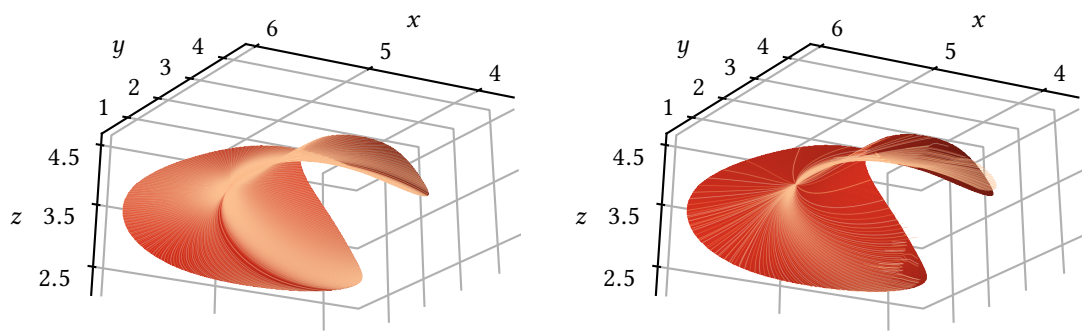


Figure 4.3: Geodesic level set approximations with varying mesh point densities, for a manifold in the steady ABC flow (which is described in section 3.1). The manifolds were all computed using the parameters given in table 4.1, with varying mesh point densities (here, given by the value of Δ_{\min}). Each of the approximations were grown from the same initial position \mathbf{x}_0 . Note how, although the microscale behaviour generally is more well-resolved as the mesh point density increases, there appears to be a threshold beneath which undesired numerical artifacts — most prevalently near the left edge of the manifold shown in (d) — manifest.

which is perfectly stationary on the sphere $\|\mathbf{x}\| = r$. We then computed strain eigenvalues and -vectors over the time interval $\mathcal{I} = [0, 10]$ for an equidistant grid of $200 \times 200 \times 200$ tracers in the domain $\mathcal{U} = [-2, 2]^3$, as outlined in sections 3.3.1 and 3.4, for $r = 1$. Moreover, we computed the arithmetic average of $\lambda_3(\mathbf{x}_0)$ across all solid angles in order to approximate it as a function of radius alone. The dependence of λ_3 as a function of radius is shown in figure 4.5, which reveals a sharp repulsion peak at $\|\mathbf{x}\| = r = 1$. This agrees well with the underlying velocity field (equation (4.5)); in particular, in passing through $\|\mathbf{x}\| = r$, the flow direction changes from radially inwards to radially outwards (or vice versa). Accordingly, we expect to find a single repelling LCS, forming a unit sphere.

Using a filtering frequency $v = 20$ (see section 3.5.1 and table 3.2) and otherwise the same parameters as given in table 4.2, we developed manifolds from the set of 225 grid points in the reduced \mathcal{U}_0 domain by the method described in sections 3.5 and 3.7–3.10. Then, by means of the method outlined in section 3.11, we extracted repelling LCSs from the computed manifolds, using a tolerance parameter $\gamma_\square = 1.2$, keeping only the LCSs with (pseudo-)surface area greater than or equal to $W_{\min} = 1$. The result was a total of 18 identical



(a) Trajectories computed in the direction field given by equation (3.24)

(b) Trajectories of the direction field given by equation (2.31), for different weights (a, b)

Figure 4.4: Trajectories orthogonal to the ξ_3 -direction field, superimposed onto a computed manifold surface in the steady ABC flow. The manifold was computed using the parameters given in table 4.2. The trajectories were computed as solution curves of equations (2.31) and (3.24), respectively, starting at (a small circle laying within the manifold, centered at) the manifold epicentre x_0 . Note how none of the trajectories ever leave the manifold. The trajectories shown in (a) cover the entire manifold, which is as expected, as the manifold mesh points were computed as end points of trajectories in a similar direction field (cf. section 3.7). The trajectories shown in (b) never leave the manifold, but face difficulties reaching certain regions of it, as can be seen from locally reduced density of trajectories. Such regions are likely only accessible for trajectories starting out at x_0 with very particular weights (a, b) .

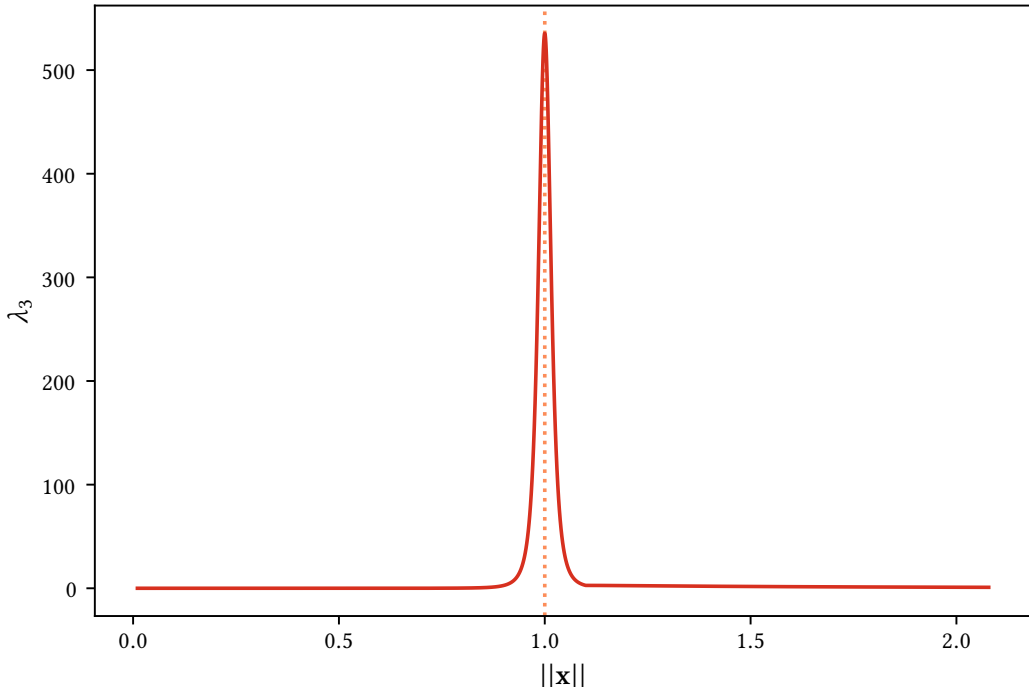


Figure 4.5: Arithmetic average of λ_3 across all solid angles, for the purely radial velocity field given by equation (4.5), using $r = 1$. Note in particular the sharp repulsion peak at $\|x\| = 1$, which is a strong indicator for the presence of a repelling LCS.

(to numerical precision) spherical LCSs of radius 1. These are shown in figure 4.6. Seeing as the expected LCS was successfully reproduced without false positives, we concluded that our LCS extraction routine functions as intended.

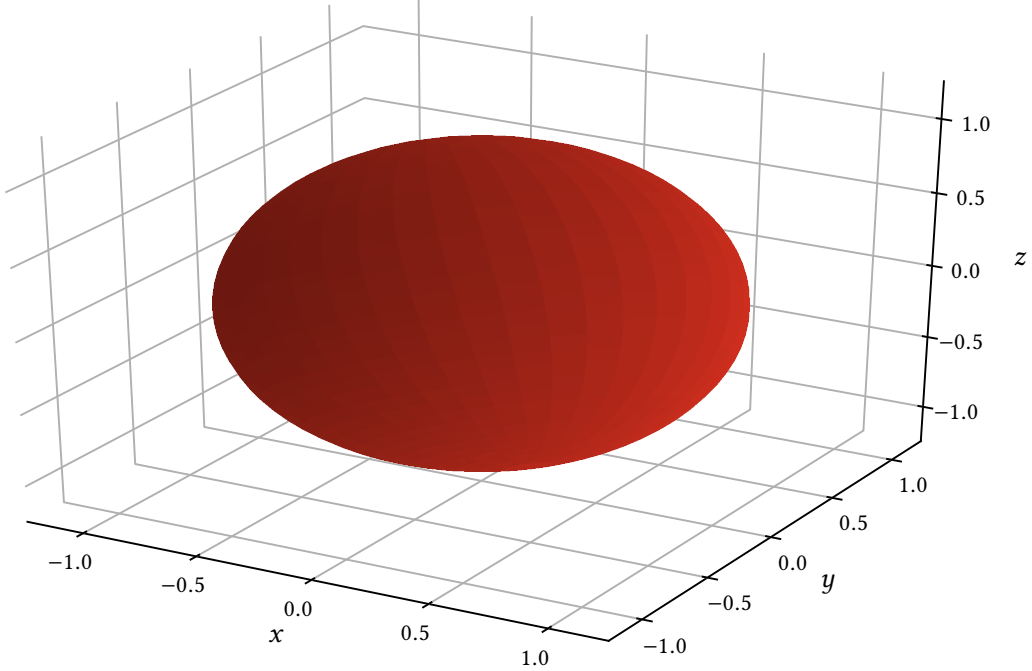


Figure 4.6: The single repelling LCS present in the purely radial velocity field given by equation (4.5) with $r = 1$. In computing the underlying manifolds, we used the filtering parameter $\nu = 20$ (cf. section 3.5.1 and table 3.2) and otherwise the same parameter values as given in table 4.2. To extract the LCSs, we used the tolerance parameter $\gamma_{\square} = 1.2$, keeping only the LCSs whose (pseudo-)surface area greater than or equal to $\mathcal{W}_{\min} = 1$ (see section 3.11). This resulted in 18 identical (to numerical precision) copies of a single, spherical, repelling LCS of unit radius – which is exactly as expected, given the sharp repulsion maximum at $\|\mathbf{x}\| = 1$, as shown in figure 4.5.

4.2.2 Verifying that the computed LCSs are in fact repelling

Per definitions 5 and 6, we expect lumps of particles which start out at opposite sides of a repelling LCS to quickly diverge under the advection of the underlying flow system. Moreover, courtesy of being material surfaces, no particles may ever cross a repelling LCS. In order to verify the impenetrable and repelling nature of the computed LCSs, we used a setup of two blobs of initial conditions, situated at opposite sides of an identified LCS surface in the steady ABC flow (more on which to follow in section 4.3). We then advected the particle blobs and the points in the parametrization of the LCS for five units of time, in the velocity field given by equations (3.1) and (3.2), using the Dormand-Prince 8(7) ODE solver in similar fashion to how we ‘adverted’ the flow map Jacobian field in the first place (see section 3.3). The initial and final states are shown in figure 4.7.

Figure 4.7 shows that, while the triangulated structure of the LCS breaks down, the two blobs of particles have been far removed from each other in the transition from figure 4.7a to

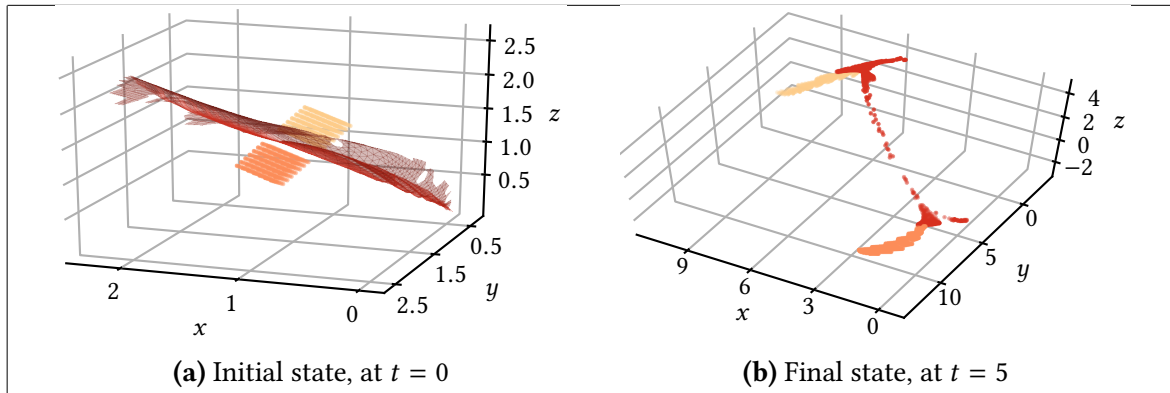


Figure 4.7: Advection of tracers in order to verify the repelling nature of the computed LCSs. At $t = 0$, two blobs of initial conditions are placed at opposite sides of a repelling LCS identified in the steady ABC flow — more on which to follow in section 4.3 — as shown in (a). The two blobs, and the mesh points in the parametrization of the LCS, are then advected by the velocity field given by equations (3.1) and (3.2) using the Dormand-Prince 8(7) ODE solver until $t = 5$, for which the corresponding state is shown in (b). Note that, although the LCS triangulation breaks down under the advection, the two blobs of particles remain fairly compact, and remain on the opposite sides of the LCS, never crossing the LCS surface. This indicates that the local centre of strongest repulsion remains located *inbetween* the two blobs of particles throughout — which is the exact behaviour we expect for a repelling LCS.

figure 4.7b. Furthermore, particles belonging to a single blob remain reasonably compact, indicating that the local repulsion centre was situated between the two blobs throughout — i.e., along the LCS. One possible explanation for the relatively large amount of stretching of the mesh points in the parametrization of the LCS under the aforementioned advection, could be that (several of) the mesh points being slightly perturbed away from the *actual* LCS surface, due to round-off errors (which are practically unavoidable, as LCSs are of infinitesimal width per existence criterion (2.28b)). Finally, the fact that none of the particles belonging to either of the two blobs ever appear to move across the LCS mesh points, supports the notion that the computed LCSs do in fact act as repelling material surfaces.

4.3 COMPUTED LCSs IN THE ABC FLOW

Having computed Cauchy-Green strain eigenvalues and -vectors for both variants of the ABC flow (as presented in section 3.1), we used the \mathcal{U}_0 domain — i.e., the grid points satisfying the LCS existence criteria (2.28a), (2.28b) and (2.28b) (the implementation of which are described in section 3.5.1) — as a first approximation to where we may reasonably expect to find repelling LCSs. Four different views of the \mathcal{U}_0 domains for the steady and unsteady ABC flows are shown in figures 4.8 and 4.9, respectively.

Note that, although the \mathcal{U}_0 domains for the two flow variants do not contain the same number of points (cf. table 3.2), the macroscopic trends remain the same. The difference lies in minute details, such as the topmost cavities in figures 4.8a and 4.9a being of slightly

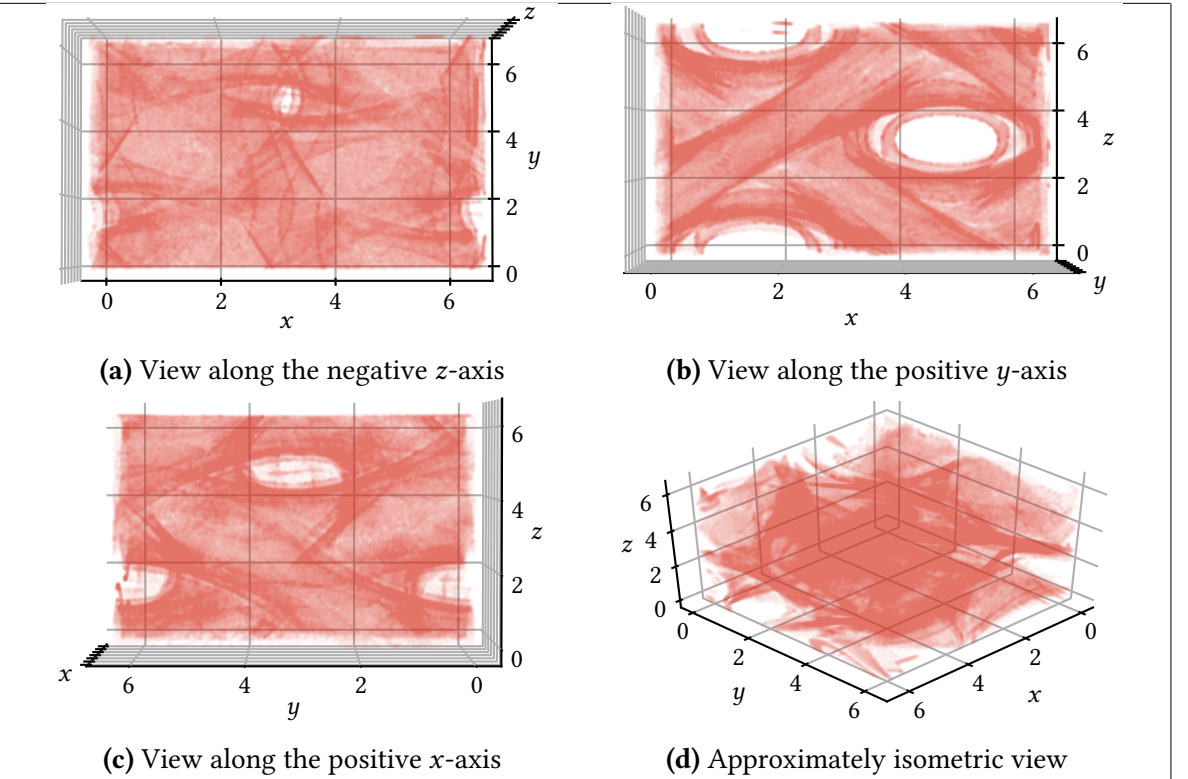


Figure 4.8: Four views of the \mathcal{U}_0 domain obtained for transport in the steady ABC flow, for the time interval $\mathcal{I} = [0, 5]$, identified as the grid points which satisfy the LCS criteria (2.28a), (2.28b) and (2.28d) (details on the implementation are available in section 3.5.1). In total, the domain consists of 340 951 different points (cf. table 3.2).

different sizes, or the point densities along the north east ‘bands’ in figures 4.8b and 4.9b being somewhat dissimilar. This is as expected, seeing as the two underlying transport systems are lightly perturbed versions of one another.

Using an approximately evenly sampled subset of the \mathcal{U}_0 domain as initial conditions, 618 and 676 for the steady and unsteady variants of the ABC flow, respectively, we then computed manifolds and extracted LCSs using the parameters in tables 3.2 and 4.2 and the method outlined in sections 3.5 and 3.7–3.11. This resulted in a total of 22 LCS surfaces for the steady flow, and 31 surfaces for the unsteady flow.

The LCSs present in the steady flow turn out to form two distinct, smooth and coherent structures, which are shown in figure 4.10. The structures lie close together, yet appear not to be connected — accordingly, the two structures are highlighted by different colors for the purpose of facilitating visual comparisons. Note in particular the correspondence between the \mathcal{U}_0 domain, shown in figure 4.8, and the computed LCSs, shown in figure 4.10 — where the perspective of each subfigure is the same as that of the corresponding subfigure in figure 4.8. Two prominent similarities are the tunnel-like structure apparent in the middle right of figures 4.8b and 4.10b, and the indent which manifests near the bottom right corner of figures 4.8c and 4.10c.

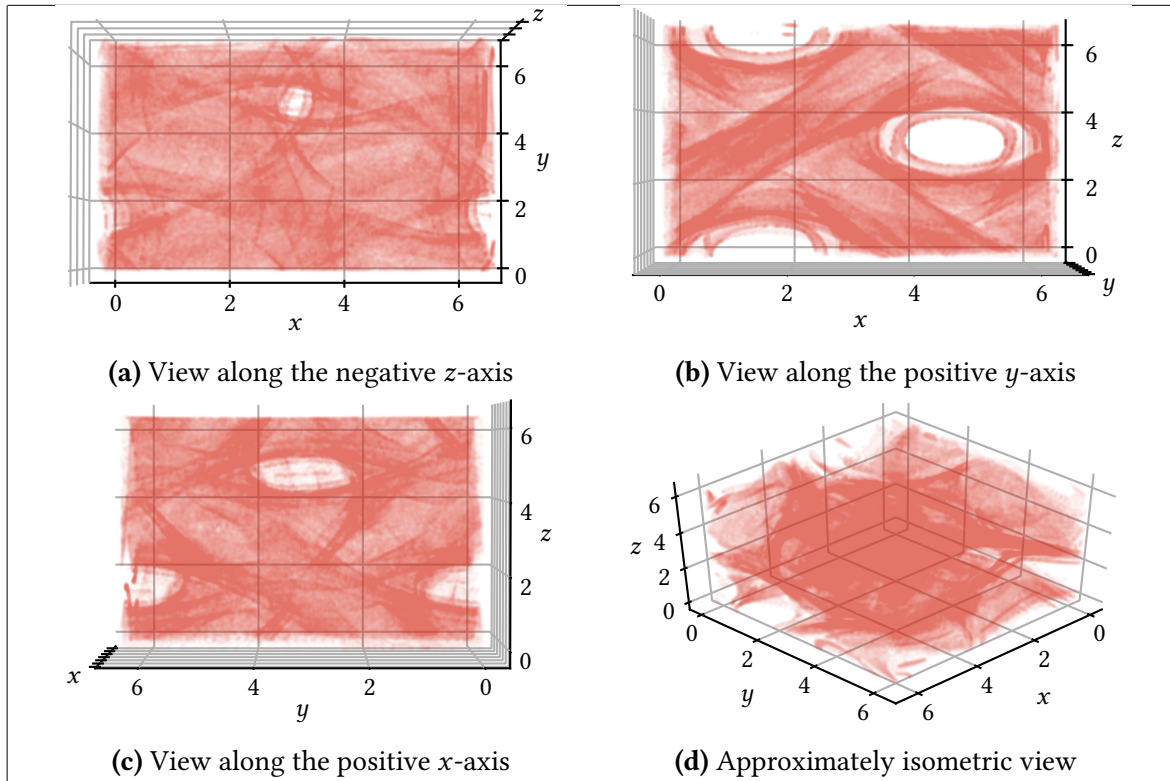


Figure 4.9: Four views of the \mathcal{U}_0 domain obtained for transport in the unsteady ABC flow, for the time interval $\mathcal{I} = [0, 5]$, identified as the grid points which satisfy the LCS criteria (2.28a), (2.28b) and (2.28d) (details on the implementation are available in section 3.5.1). In total, the domain consists of 361 461 different points (cf. table 3.2).

The computed LCSs in the unsteady flow constitute three distinct, smooth and coherent structures, which are shown in figure 4.11. Although the structures lie adjacent to each other, they do not seem to be connected. Thus, the different structures are indicated using disparate colors, yet again to facilitate visual comparisons. Just like for the LCSs in the steady flow, the computed LCSs strongly resemble subsets of the \mathcal{U}_0 , shown in figure 4.9 — where the viewing angle of each \mathcal{U}_0 domain subfigure is the same as that of the corresponding subfigure in figure 4.11. The two largest structures apparent in figure 4.11 harmonize with the two dominant structures found for the steady flow (see figure 4.10). The smallest structure appears reasonable when considered together with the \mathcal{U}_0 domain — shown in figure 4.9 — in particular, it further enhances the tubular structures manifesting in the middle right of figures 4.9b and 4.11b, and the middle top of figures 4.9c and 4.11c.

4.4 COMPUTED LCSs IN THE FØRDE FJORD

Just like for the ABC flow, we used the \mathcal{U}_0 domain — i.e., the grid points satisfying the LCS existence criteria (2.28a), (2.28b) and (2.28d) (the implementation of which are described in section 3.5.1) — obtained for the transport system governed by the oceanic currents in the Førde fjord as a first approximation to where repelling LCSs can reasonably be expected to be found. Four different views of the \mathcal{U}_0 domain are shown in figure 4.12. Compared to

Table 4.2: Parameters used to compute manifolds, and subsequently repelling LCSs, in both variants of the ABC flow (see section 3.1).

Parameter	Value	Description
δ_{init}	10^{-3}	Separation of innermost geodesic level set from the manifold epicentre, cf. figure 3.4
$\Delta_{\min}, \Delta_{\max}$	0.04, 0.16	Boundaries for interpoint separations (details found in section 3.8.1)
Δ_1	$2\Delta_{\min}$	Interset distance used to compute the second geodesic level set (see sections 3.7 and 3.8.3)
γ_{Δ}	$5 \cdot 10^{-3}$	Tolerance for the separation of a mesh point from its ancestor (per equation (3.26))
γ_{arc}	5	Sets an upper limit to trajectory lengths as $\gamma_{\text{arc}}\Delta_i$ (briefly mentioned in section 3.7.1)
γ_{\cup}	$7 \cdot 10^{-1}$	Sets an upper limit to the extent of loop-like segments of any level set (see section 3.8.2)
α_{\uparrow}	$8.7 \cdot 10^{-2} \text{ rad } (5^\circ)$	Used in a curvature-based approach to adjust interset distances (outlined in section 3.8.3)
α_{\downarrow}	$4.4 \cdot 10^{-1} \text{ rad } (25^\circ)$	
$(\Delta\alpha)_{\uparrow}, (\Delta\alpha)_{\downarrow}$	$2\Delta_{\max}\alpha_{\uparrow}, 2\Delta_{\min}\alpha_{\downarrow}$	
γ_{\square}	1.75	Relaxation parameter for extracting LCSs from the computed manifolds (see section 3.11)
W_{\min}	6.0	Filters away the smallest LCSs measured in (pseudo-)surface area (see section 3.11)

the corresponding domains for the two variants of the ABC flow (as shown in figures 4.8 and 4.9), the flow in the Førde fjord appears a lot more chaotic, with fewer discernible macroscopic trends. Figures 4.12b and 4.12c do, however, indicate that the points in the oceanic \mathcal{U}_0 domain are loosely organized in horizontal layers.

Using an approximately evenly sampled subset of the \mathcal{U}_0 domain – yielding a total of 1 631 grid points – as initial conditions, we then computed manifolds and extracted LCSs using the parameters in tables 3.2 and 4.3 and the method outlined in sections 3.5 and 3.7–3.11. This resulted in a total of 110 LCS surfaces. As figure 4.13 indicates, these largely appear to be organized in a sequence of horizontal layers. Moreover, all of the LCSs are sufficiently large to warrant treating them as individual entities. Thus, in contrast to the LCSs obtained in (either version of) the ABC flow (see section 4.3), we elected to assign each LCS a numerical value

$$Q_i = \frac{\log(\bar{\lambda}_3)_i}{\max_i \{ \log(\bar{\lambda}_3)_i \}}, \quad (4.6)$$

where $(\bar{\lambda}_3)_i$, the repulsion average of LCS surface i , is defined in equation (3.32). We then used the (unit normalized) set of numbers $\{Q_i\}$ to select a color for the corresponding LCSs, drawn from a perceptually uniform colormap.

When comparing the computed LCSs (figure 4.13) to the corresponding \mathcal{U}_0 domain (fig-

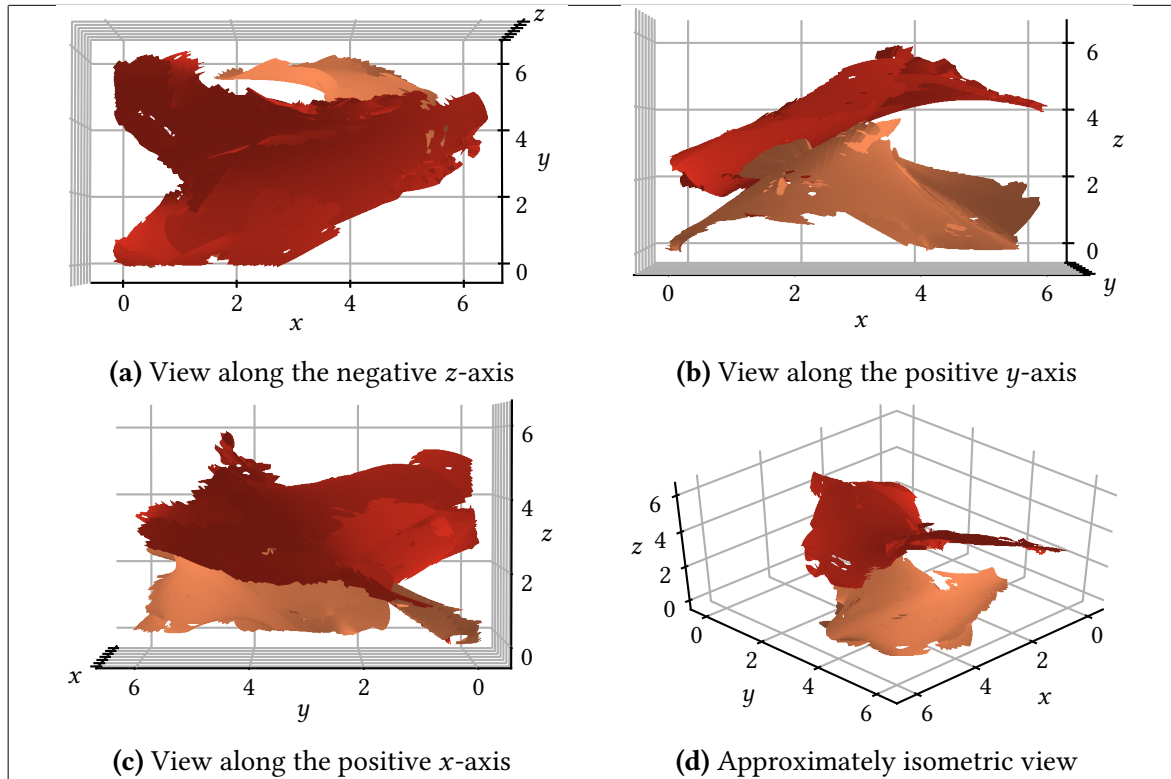


Figure 4.10: Four views of the repelling LCSs obtained for transport in the steady ABC flow, for the time interval $\mathcal{I} = [0, 5]$ (see section 3.1.1). A total of 22 surfaces constitute two distinct, smooth and coherent structures, which are shown in different colors. We provide four different viewing angles (the same as the ones used in figure 4.8, which shows the computed \mathcal{U}_0 domain), chosen in order convey the three-dimensional structures in as great detail as possible.

ure 4.12), the organization of the LCSs in horizontal layers seems reasonable. This is particularly apparent from inspecting figures 4.12b and 4.13b, and figures 4.12c and 4.13c. This indicates that the oceanic flow undergoes the most stretching in the vertical direction. Lastly, the repulsion appears to be largely uniform within any given depth layer.

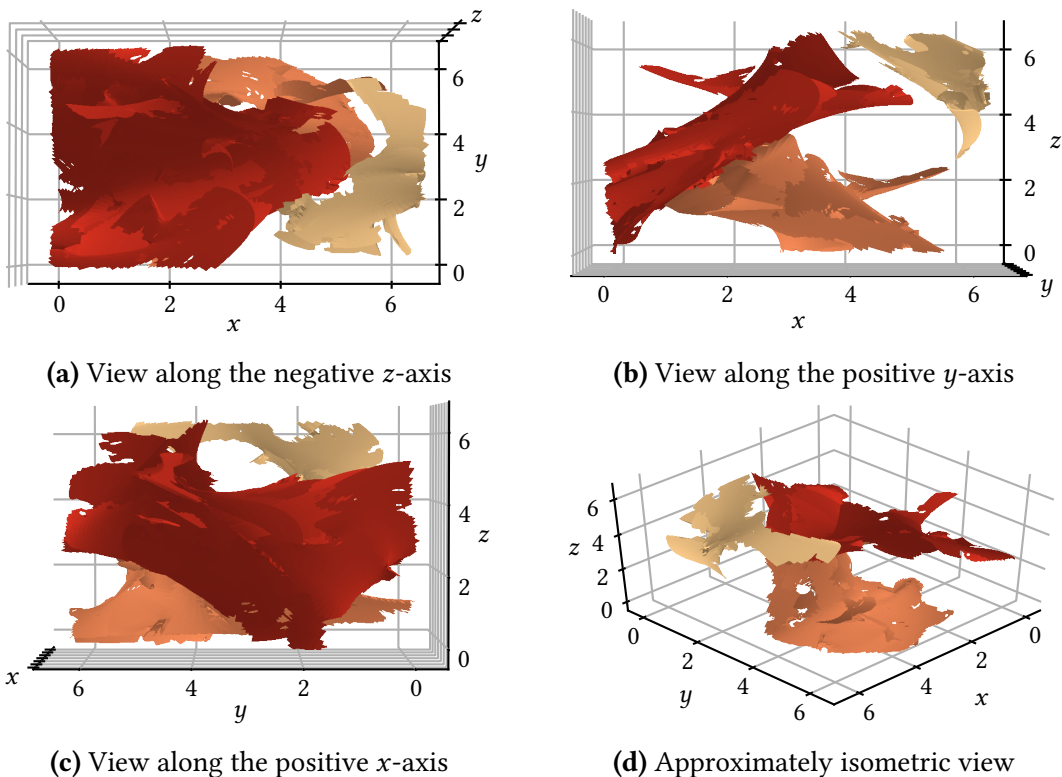


Figure 4.11: Four views of the repelling LCSs obtained for transport in the unsteady ABC flow, for the time interval $\mathcal{I} = [0, 5]$ (see section 3.1.2). A total of 31 surfaces constitute three distinct, smooth and coherent structures, which are shown in different colors. We provide four different viewing angles (the same as the ones used in figure 4.9, which shows the computed \mathcal{U}_0 domain), chosen in order convey the three-dimensional structures in as great detail as possible.

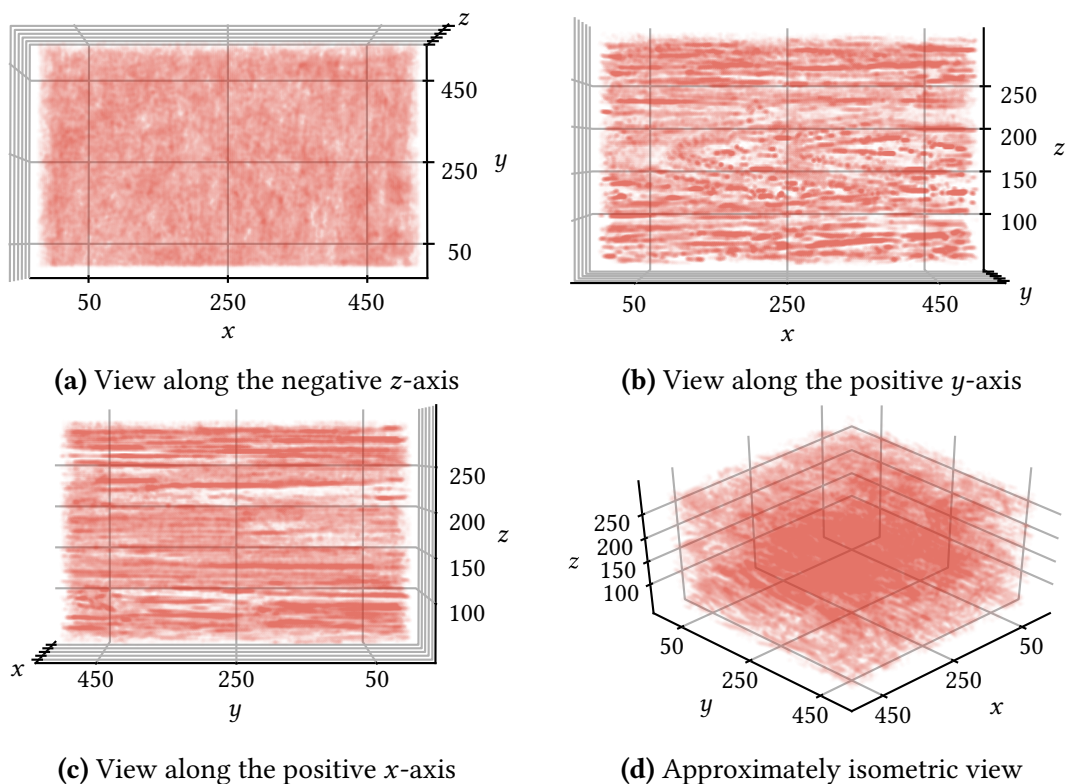


Figure 4.12: Four views of the \mathcal{U}_0 domain obtained for transport in the Førde fjord, over a time interval of 12 hours (see section 3.2), identified as the grid points which satisfy the LCS criteria (2.28a), (2.28b) and (2.28d) (details on the implementation are available in section 3.5.1). Note that the axes are given in metres, where $z = 0$ corresponds to the surface level, increasing downwards. In total, the domain consists of 1 631 points (cf. table 3.2).

Table 4.3: Parameters used to compute manifolds, and subsequently repelling LCSs, in the Førde fjord (see section 3.2). Note that, as the domain of interest is scaled in units of metre, so too are δ_{init} , Δ_{\min} , Δ_{\max} and Δ_1 ; whereas \mathcal{W}_{\min} is given in square metre.

Parameter	Value	Description
δ_{init}	10^{-1}	Separation of innermost geodesic level set from the manifold epicentre, cf. figure 3.4
$\Delta_{\min}, \Delta_{\max}$	2, 8	Boundaries for interpoint separations (details found in section 3.8.1)
Δ_1	$2\Delta_{\min}$	Interset distance used to compute the second geodesic level set (see sections 3.7 and 3.8.3)
γ_{Δ}	$5 \cdot 10^{-3}$	Tolerance for the separation of a mesh point from its ancestor (per equation (3.26))
γ_{arc}	5	Sets an upper limit to trajectory lengths as $\gamma_{\text{arc}}\Delta_i$ (briefly mentioned in section 3.7.1)
$\gamma_{\circlearrowleft}$	$7 \cdot 10^{-1}$	Sets an upper limit to the extent of loop-like segments of any level set (see section 3.8.2)
α_{\uparrow}	$8.7 \cdot 10^{-2} \text{ rad } (5^\circ)$	Used in a curvature-based approach to adjust interset distances (outlined in section 3.8.3)
α_{\downarrow}	$4.4 \cdot 10^{-1} \text{ rad } (25^\circ)$	
$(\Delta\alpha)_{\uparrow}, (\Delta\alpha)_{\downarrow}$	$2\Delta_{\max}\alpha_{\uparrow}, 2\Delta_{\min}\alpha_{\downarrow}$	
γ_{\square}	1.2	Relaxation parameter for extracting LCSs from the computed manifolds (see section 3.11)
\mathcal{W}_{\min}	20 000	Filters away the smallest LCSs measured in (pseudo-)surface area (see section 3.11)

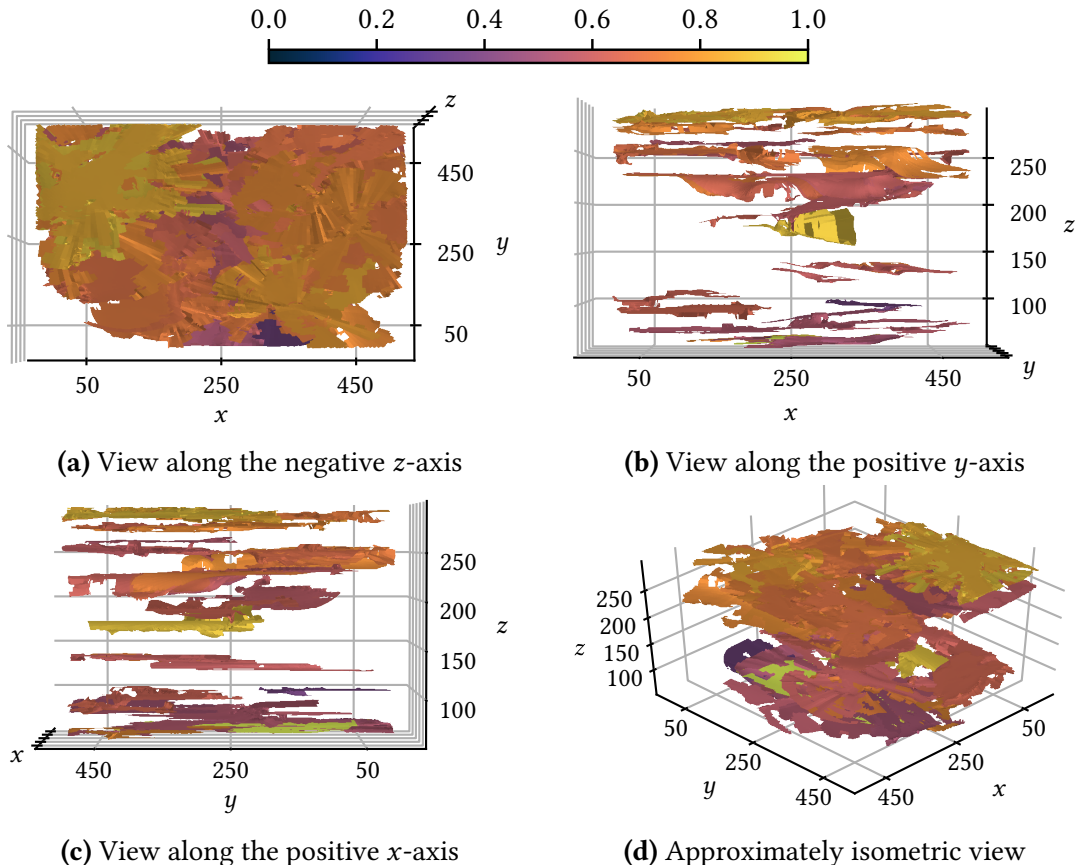


Figure 4.13: Four views of the repelling LCSs obtained for transport in the Førde fjord, over a time interval of 12 hours (see section 3.2). A total of 110 distinct surfaces are shown, which are colored according to their relative repulsion averages (per equation (4.6)) using the perceptually uniform colormap shown at the top. We provide four different viewing angles (the same as the ones used in figure 4.12, which shows the computed \mathcal{U}_0 domain), chosen in order to convey the three-dimensional structures in as great detail as possible.

5 Discussion

5.1 REGARDING THE VARIATIONAL APPROACH TO COMPUTING THE CAUCHY-GREEN STRAIN CHARACTERISTICS

As outlined in sections 3.3 and 3.4, we used an SVD decomposition of the flow map Jacobian to find the Cauchy-Green strain eigenvalues and -vectors, rather than computing these directly from the Cauchy-Green strain tensor field. This approach, suggested by Miron et al. (2012) and endorsed by Oettinger and Haller (2016), boasts superior accuracy compared to the more conventional approach of approximating the directional derivatives of the flow map (i.e., the components of the flow map Jacobian) by applying a finite difference method and then explicitly computing the Cauchy-Green strain tensor field – as was done by Farazmand and Haller (2012a). In addition to the increased mathematical complexity of directly transporting the flow map Jacobian field, the approach relies on bounded first spatial derivatives of the underlying velocity field, as is evident from inspecting equation (2.22). This should, however, not be an issue when considering smooth analytical test cases, or when using a high (quadratic or higher, cf. section 2.1.2) order interpolation method for gridded data. Alternatively, the derivatives can be approximated by e.g. a finite difference method. Should any of these approaches prove impractical, the method of Farazmand and Haller (2012a) could be sufficient.

- Bruk av Dormand-Prince-integrator ga oss en frihetsgrad mindre (integrasjonsstenglende)
- ABC-LCSenes robusthet under tidsavhengig perturbasjon tyder på at metoden er velegnet også for bruk på modelldata
- Henvis til Peacock et al.'s haveksperiment (tracers sluppet fra båt)
- Avveiningsspørsmål hvorvidt en skal kjøre full 3D-analyse, eller nøye seg med 2D
 - For systemer som til god tilærming kan betraktes som todimensjonale, som spredning av olje-/plastsøl langs havoverflatestrømninger, vil nok todimensjonal analyse kunne være tilstrekkelig – fordi utstrekningen i planet (generelt) er signifikant større enn i dybderetningen
 - For systemer som større elver eller fjorder, hvor utstrekningen er i samme størrelsesorden som dybden – eller, når en betrakter spredningsprosesser som ikke begrenser seg til overflatestrømninger (som feks rester fra gruvedeponi) – kan 3D-analyse være hensiktsmessig
 - *Situasjonsavhengig*

6 Conclusions

For future work: Siter abstractet til (Haller and Karrasch 2018), finnes på <https://agu.confex.com/agu/os18/meetingapp.cgi/Paper/316654>

References

- Blazevski, D. and Haller, G. (2014). "Hyperbolic and elliptic transport barriers in three-dimensional unsteady flows". In: *Physica D: Nonlinear Phenomena* 273–274, pp. 46–62. ISSN: 0167-2789. DOI: [10.1016/j.physd.2014.01.007](https://doi.org/10.1016/j.physd.2014.01.007).
- de Boor, C. (1978). *A Practical Guide to Splines*. 1st ed. Springer-Verlag New York. ISBN: 0-387-95366-3.
- Farazmand, M. and Haller, G. (2012a). "Computing Lagrangian coherent structures from their variational theory". In: *Chaos: An Interdisciplinary Journal of Nonlinear Science* 22.1, p. 013128. ISSN: 1054-1500. DOI: [10.1063/1.3690153](https://doi.org/10.1063/1.3690153).
- Farazmand, M. and Haller, G. (2012b). "Erratum and addendum to 'A variational theory of hyperbolic Lagrangian coherent structures' [Physica D 240 (2011) 547–598]". In: *Physica D: Nonlinear Phenomena* 241.4, pp. 439–441. ISSN: 0167-2789. DOI: [10.1016/j.physd.2011.09.013](https://doi.org/10.1016/j.physd.2011.09.013).
- Frisch, U. (1995). *Turbulence, the legacy of A.N. Kolmogorov*. 1st ed. Cambridge University Press. ISBN: 0-521-45103-5.
- Garvik, O. (Dec. 12, 2017). "Gruvekonflikten i Førdefjorden". In: *Store norske leksikon*. Available at https://snl.no/Gruvekonflikten_i_Førdefjorden (accessed May 11, 2018).
- Hairer, E., Nørsett, S. P., and Wanner, G. (1993). *Solving Ordinary Differential Equations I: Nonstiff Problems*. 2nd ed. Springer-Verlag Berlin Heidelberg. ISBN: 978-3-540-56670-0. Corrected 3rd printing, 2008.
- Hairer, E. and Wanner, G. (1996). *Solving Ordinary Differential Equations II: Stiff and Differential-Algebraic Problems*. 2nd ed. Springer-Verlag Berlin Heidelberg. ISBN: 978-3-642-05221-7. Corrected 2nd printing, 2002.
- Haller, G. (2011). "A variational theory of hyperbolic Lagrangian Coherent Structures". In: *Physica D: Nonlinear Phenomena* 240.7, pp. 547–598. ISSN: 0167-2789. DOI: [10.1016/j.physd.2010.11.010](https://doi.org/10.1016/j.physd.2010.11.010).
- Haller, G. and Karrasch, D. (2018). *Material Barriers to Diffusive Mixing: Theory*. Paper presented at the Ocean Sciences Meeting, Portland, OR, February 12–16.
- Haugan, I. (May 20, 2015). "– Sjødeponi kan være den beste løsningen". In: *forskning.no*. Available at <https://forskning.no/forurensning-bergfag-geofag-kjemi/2015/05/sjodeponi-kan-vaere-den-bestе-løsningen> (accessed May 11, 2018).
- Karrasch, D. (2012). "Comment on 'A variational theory of hyperbolic Lagrangian coherent structures, Physica D 240 (2011) 574–598'". In: *Physica D: Nonlinear Phenomena* 241.17, pp. 1470–1473. ISSN: 0167-2789. DOI: [10.1016/j.physd.2012.05.008](https://doi.org/10.1016/j.physd.2012.05.008).
- Krauskopf, B. et al. (2005). "A Survey of Methods for Computing (un)Stable Manifolds of Vector Fields". In: *International Journal of Bifurcation and Chaos* 15.3, pp. 763–791. ISSN: 1793-6551. DOI: [10.1142/S0218127405012533](https://doi.org/10.1142/S0218127405012533).
- Løken, A. M. T. (2017). "Sensitivity to Numerical Integration Scheme in Calculation of Lagrangian Coherent Structures". Unpublished specialization project. Available at http://folk.ntnu.no/amløken/sensitivity_to_numerical_integration_scheme_loken.pdf.
- Miron, P. et al. (2012). "Anisotropic mesh adaption on Lagrangian Coherent Structures". In: *Journal of Computational Physics* 231.19, pp. 6419–6437. ISSN: 0021-9991. DOI: [10.1016/j.jcp.2012.06.015](https://doi.org/10.1016/j.jcp.2012.06.015).

References

- Möller, T. and Trumbore, B. (1997). "Fast, Minimum Storage Ray-Triangle Intersection". In: *Journal of Graphics Tools* 2.1, pp. 21–28. DOI: [10.1080/10867651.1997.10487468](https://doi.org/10.1080/10867651.1997.10487468).
- Oettinger, D. and Haller, G. (2016). "An autonomous dynamical system captures all LCSs in three-dimensional unsteady flows". In: *Chaos: An Interdisciplinary Journal of Nonlinear Science* 26.10. ISSN: 1054-1500. DOI: [10.1063/1.4965026](https://doi.org/10.1063/1.4965026).
- Onu, K., Huhn, F., and Haller, G. (2015). "LCS Tool: A computational platform for Lagrangian coherent structures". In: *Journal of Computational Science* 7, pp. 26–36. ISSN: 1877-7503. DOI: [10.1016/j.jocs.2014.12.002](https://doi.org/10.1016/j.jocs.2014.12.002).
- Prince, P. and Dormand, J. (1981). "High order embedded Runge-Kutta formulae". In: *Journal of Computational and Applied Mathematics* 7.1, pp. 67–75. ISSN: 0377-0427. DOI: [10.1016/0771-050X\(81\)90010-3](https://doi.org/10.1016/0771-050X(81)90010-3).
- Slagstad, D. and McClamans, T. A. (2005). "Modeling the ecosystem dynamics of the Barents sea including the marginal ice zone: I. Physical and chemical oceanography". In: *Journal of Marine Systems* 58.1, pp. 1–18. ISSN: 0924-7963. DOI: [10.1016/j.jmarsys.2005.05.005](https://doi.org/10.1016/j.jmarsys.2005.05.005).
- Stoer, J. and Bulirsch, R. (2002). *Introduction to Numerical Analysis*. Springer-Verlag New York. ISBN: 978-1-4419-3006-4.
- Williams, J. (2018). *Bspline-Fortran: Multidimensional B-Spline Interpolation of Data on a Regular Grid*. Zenodo. DOI: [10.5281/zenodo.1215290](https://doi.org/10.5281/zenodo.1215290). Open Access Software.
- Zhao, X.-H. et al. (1993). "Chaotic and Resonant Streamlines in the ABC flow". In: *SIAM Journal on Applied Mathematics* 53.1, pp. 71–77. ISSN: 0036-1399. DOI: [10.1137/0153005](https://doi.org/10.1137/0153005).

A Appendix A